Journal of Ophthalmology

Optical Coherence Tomography in Ophthalmology

Guest Editors: Eduardo Buchele Rodrigues, Felipe Medeiros, Stefan Mennel, and Fernando M. Penha

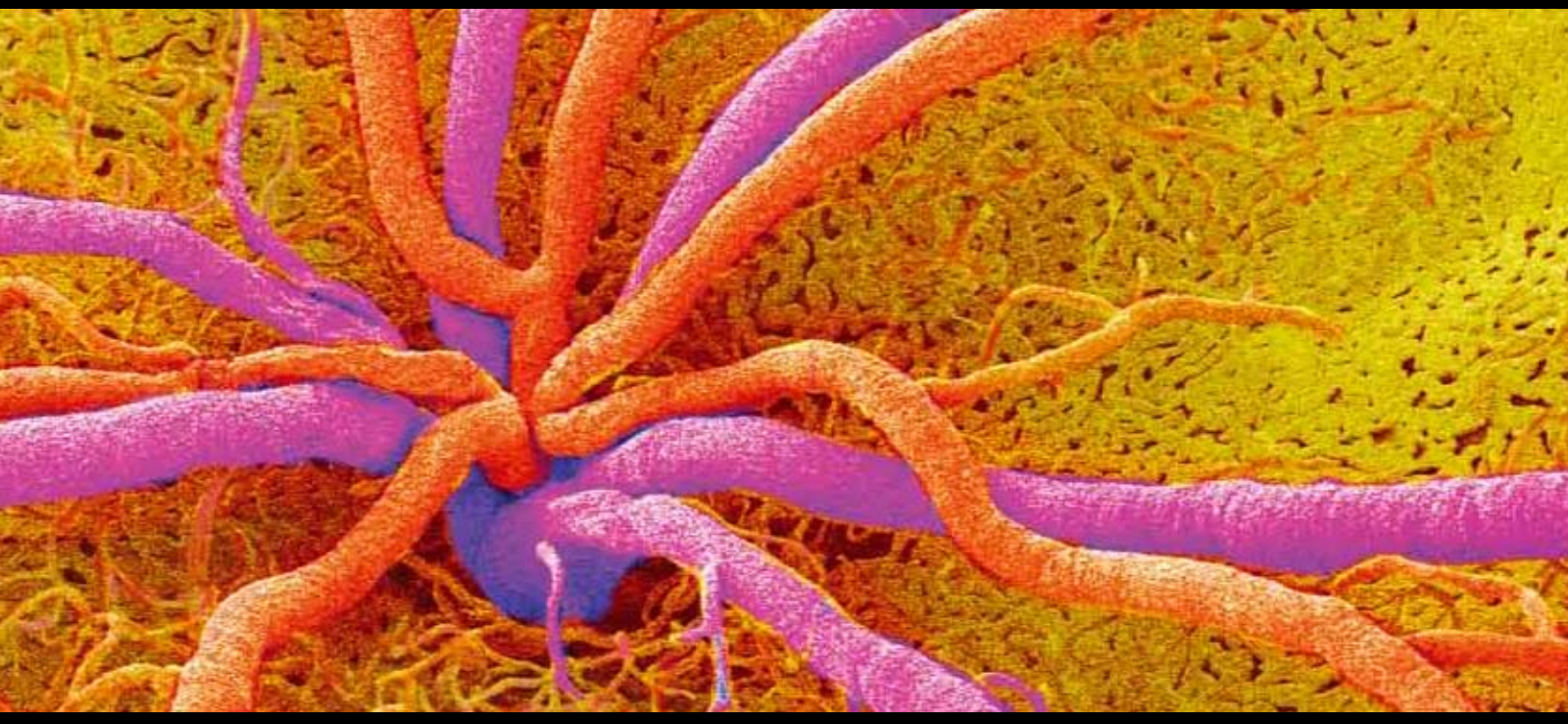

Optical Coherence Tomography in Ophthalmology

Journal of Ophthalmology

Optical Coherence Tomography in Ophthalmology

Guest Editors: Eduardo Buchele Rodrigues, Felipe Medeiros, Stefan Mennel, and Fernando M. Penha

Editorial Board

Contents

Hindawi Publishing Corporation
Journal of Ophthalmology
Volume 2012, Article ID 134569, 1 page
doi:10.1155/2012/134569

Editorial

Optical Coherence Tomography in Ophthalmology

Eduardo Buchele Rodrigues,[1] Felipe Medeiros,[2] Stefan Mennel,[3] and Fernando M. Penha[4]

[1] *Department of Ophthalmology, Federal University of São Paulo, R. Botucatu, 821 Vila Mariana, 04023-062 São Paulo, SP, Brazil*
[2] *Department of Ophthalmology, University of California, San Diego, CA 92093, USA*
[3] *Department of Ophthalmology, Philipps University Marburg, 35032 Marburg, Germany*
[4] *Department of Ophthalmology, Federal University of São Paulo, São Paulo, SP, Brazil*

Correspondence should be addressed to Eduardo Buchele Rodrigues, rodriguesretina@gmail.com

Received 25 December 2011; Accepted 25 December 2011

Optical coherence tomography (OCT) is an optical signal acquisition and processing method that captures micrometer-resolution three-dimensional images from within biological tissues. In recent years, OCT has become an important imaging technology used in diagnosing and following macular pathologies. It has complemented fluorescein angiography in many cases, especially in the diagnosis and management of various retinal disorders, including macular edema and age-related macular degeneration. In addition, further development enabled application of optical coherence tomography in evaluation of the integrity of the nerve fiber layer, optic nerve cupping, anterior chamber angle, or corneal topography.

In this special issue, a number of researchers and physicians prepared twelve papers to discuss developments on the application of OCT for ocular diseases diagnosis. It comprises three review articles, six original articles, and three case reports. One of the review articles is an overview on the usefulness of OCT for the anterior segment entities by our work group. The other two review papers deal with the use of OCT in ophthalmic tumors and on the simultaneous confocal scanning laser ophthalmoscopy combined with high-resolution spectral domain. Three case reports show unique features of OCT in patients with fundus abnormalities as diffuse unilateral subacute neuroretinitis, central serous chorioretinopathy, and punctate inner choroidopathy. Original papers on various subjects such as glaucoma diagnostics, retinal detachment, or retinitis pigmentosa offer novel insights into ophthalmology research.

We expect this special issue to be a contribution to the progress in imaging in ophthalmology. The diversity of papers illustrates the wide utility of OCT in ophthalmology.

Acknowledgments

The editors acknowledge the efforts of the writers and the publisher staff.

Eduardo Buchele Rodrigues
Felipe Medeiros
Stefan Mennel
Fernando M. Penha

Hindawi Publishing Corporation
Journal of Ophthalmology
Volume 2012, Article ID 806989, 5 pages
doi:10.1155/2012/806989

Review Article

Anterior Segment Tomography with the Cirrus Optical Coherence Tomography

Eduardo B. Rodrigues,[1,2] Margara Johanson,[1,2] and Fernando M. Penha[1,2]

[1] *Department of Ophthalmology, Vision Institute, UNIFESP, Sao Paulo, Brazil*
[2] *Instituto de Olhos de Florianópolis, Rua Presidente Coutinho 579, Conjunto 501, 88000 Florianópolis, SC, Brazil*

Correspondence should be addressed to Eduardo B. Rodrigues, rodriguesretina@gmail.com

Received 11 April 2011; Accepted 11 October 2011

Academic Editor: Stefan Mennel

Optical coherence tomography (OCT) is an optical acquisition method to examine biological tissues. In recent years, OCT has become an important imaging technology used in diagnosing and following macular pathologies. Further development enabled application of optical coherence tomography in evaluation of the integrity of the nerve fiber layer, optic nerve cupping, anterior chamber angle, or corneal topography. In this manuscript we overview the use of OCT in the clinical practice to enable corneal, iris, ciliary body, and angle evaluation and diagnostics.

1. Introduction

Optical coherence tomography (OCT) systems use low-coherence, near-infrared light to provide detailed images of anterior segment structures at resolutions exceeding other systems like ultrasound biomicroscopy or conventional ultrasound [1, 2]. The first use of OCT for anterior segment imaging has been reported by Izatt and coworkers, who developed a slit-lamp-mounted, 830 nm time-domain device [3]. The initial equipment allowed direct in vivo measurements of corneal thickness and surface profile, anterior chamber depth and angle, and iris thickness and surface profile. Since then, significant technology progress has been made which ultimately enabled establishment of the current time-domain Visante OCT as well as the spectral-domain OCT device. The Cirrus spectral-domain equipment (Carl Zeiss Meditec, Dublin, CA, USA) is an around 5 micra high-definition (HD) 840 nm spectral-domain OCT instrument primarily designed for retinal imaging.

The purpose of this paper is to present the various applications of the HD-OCT Cirrus device in the clinical practice to enable corneal, iris, ciliary body, and angle evaluation, for instance, examination of even fine structures like Descemet's membrane, the trabecular meshwork, and Schwalbe's line.

2. Acquiring Anterior Segment Scans with the Cirrus

The Anterior Segment Cube 512 × 128 mode generates a volume of data through a 4-millimeter square grid by acquiring a series of 128 horizontal scan lines each composed of 512 A-scans. The mode acquires a pair of high-definition scans through the center of the cube in the vertical and horizontal directions that are composed of 1024 A-scans each. The Anterior Segment Cube 512 × 128 can be used for measuring the central corneal thickness and create a 3-D image of the data.

The Anterior Segment 5-Line Raster scans through 5 parallel lines of equal length that can be used to view high-resolution images of the anterior chamber angle and cornea. The line length is fixed at 3 mm, while the rotation and spacing are adjustable. Each line is composed of 4096 A-scans, and by default, the lines are horizontal and separated by 250 μm, so that the 5 lines together cover 1 mm width.

3. Corneal Evaluation

3.1. Indications and Limitations. The HD-OCT device has been recently used as a noninvasive corneal imaging modality

that was capable of in vivo differentiation of both corneal layers and demonstration of pathologic abnormalities in the cornea (Figure 1). Corneal indications for the Cirrus OCT can be divided into pachymetry analysis, keratectomy, refractive surgery, structural, and contact lens abnormalities. For pachymetry, the Anterior Segment Cube 512×128 enables identification of the central corneal section, which facilitates positioning for central corneal thickness measurements. Images are framed in blue and pink in order to demonstrate the vertical and horizontal line (Figure 2). No specific pachymetry map on the Cirrus is yet provided. Further studies should be performed to compare the validity of the Cirrus pachymetry with other devices, for example, Pentacam.

For refractive surgery corneal Cirrus OCT enables identification of the postoperative flap and unexpected changes as epithelial ingrowth. The thickness of eventual epithelial hyperplasia can be viewed by the Cirrus OCT. Postoperatively, OCT enables visualization of corneal flaps, as well as the integrity of the corneal layers.

For keratectomy the HD-OCT also allows various changes such as attachment of the implanted posterior Descemet in DMEK procedure or even wrinkle or fold within the DSEK. The OCT images also enable better clinical decision to conduct more accurate planning of treatments for corneal opacities.

Structural anatomies of the cornea like keratin precipitates secondary to uveitis can be monitored with the Cirrus OCT. Cases of intrastromal corneal foreign body can be viewed by the Cirrus. OCT accurately maps corneal thickness in clear and opacified corneas, allowing the examiner to precisely map the depth of corneal opacities, the degree of epithelial hyperplasia, and the thickness of the cornea, as well as corneal edema and thickening, scleral melts, corneal degenerations, and scars as well as corneal dystrophies [4] (Figure 3). Cirrus OCT provides clear delineation of corneal anatomic features and pathologic corneal deposits in most cases. The characteristics and depth of these deposits are illustrated and can be localized to specific layers of the cornea. When available, there has been significant correlation between OCT images and histopathologic features, providing a noninvasive confirmation of the clinical diagnosis.

Contact lens distance to the corneal epithelial can be measured with the Cirrus OCT. It enables to distinguish cases of thinner tear film thickness, which may be a sign of tight contact lens adaptation. Some of the limitations of the Cirrus in corneal analysis include not enough resolution for endothelial cell distinction, less precise pachymetry in comparison to the Pentacam, and little amount of publications on the topic in the medical literature.

3.2. Selected Clinical Cases

Case 1. An 86-year-old female underwent phacoemulsification surgery for therapy of cataracta rubra, advanced nuclear sclerosis. The surgery lasted 28 minutes while ultrasound time 3.02 minutes. Figure 4 shows microbullous keratopathy after phacoemulsification with dense corneal edema and interruption of endothelium-Descemet's membrane layer.

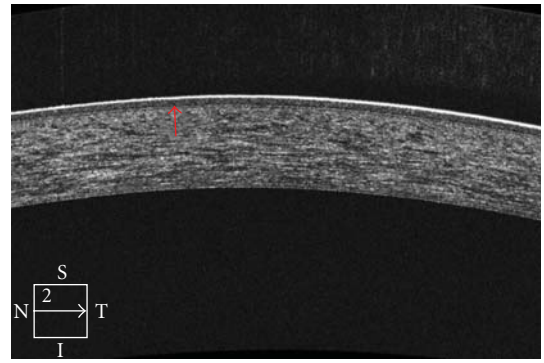

Figure 1: High-definition OCT of the cornea enables localization of the interface between the corneal stroma and epithelial/Bowman's layer.

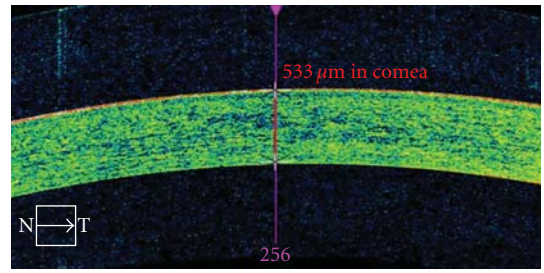

Figure 2: Anterior Segment Cube 512×128 imaging of the cornea enables pachymetry measurements.

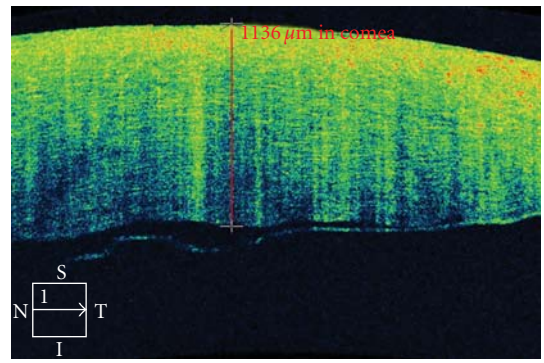

Figure 3: Cirrus OCT of a 79-year-old patient who underwent cataract surgery. She developed postoperative corneal edema detected and monitored by the Cirrus OCT, characterized by diffuse hyperreflectivity interspacing lacunae of hyporeflectivity on corneal OCT scan. In addition, interruption of the endothelial layer can be documented.

Case 2. A 77-year-old patient presents with nuclear lens cataract. Preoperative evaluation included specular corneal microscopy, fundus evaluation, and pachymetry. Figure 2 demonstrates the utility of the CIRRUS for measurement of the total central corneal thickness of 533 micra. Recent research demonstrated accordance of these outcomes with the pachymetry data [5].

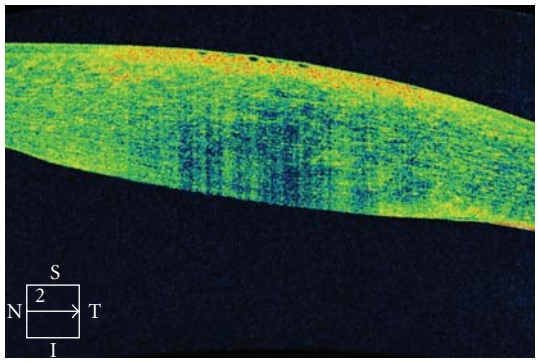

Figure 4: Corneal imaging with the Cirrus OCT of an 86-year-old female patient who underwent lens phacoemulsification for therapy of dense nigra cataract. She developed focal microbullous keratopathy. OCT shows both the remarkable corneal edema, as well as interruption of endothelium layer. The patient was treated with topical steroids and experience improvement 4 weeks later.

Table 1: Some properties and differences among Visante, Pentacam, and Cirrus OCT are described in detail. Courtesy of Zeiss.

(I) Visante anterior segment OCT
(a) Anterior segment
(i) 6 mm depth by 16 mm width 256 A-Scan per B-Scan
(ii) 3 mm depth by 10 mm width 512 A-Scan per B-Scan
(b) Wavelength 1310 nm (infrared, nonvisible light)
(II) Cirrus HD-OCT
(a) Anterior segment
(i) Cube: 4×4 mm, 512 A-Scan
(ii) 5-Line Raster: 3 mm, 4096 A-Scans
(b) Posterior segment
(i) Cube: 6×6 mm, 512 A-Scan
(ii) 5-Line Raster: 9 mm, 4096 A-Scans
(c) Wavelength 840 nm
(III) Pentacam
(a) Rotating Scheimpflug Imaging System
(b) Wavelength 475 nm, blue LED (Info: Ziemer Galilei wavelength 470 nm)

4. Anterior Chamber Angle Evaluation

4.1. Indications, Limitations, and Comparison with the Visante OCT. The Visante anterior segment OCT system (Carl Zeiss Meditec, Dublin, CA, USA) is a time-domain 1310 nm operating device that supports several modes, including high-resolution cornea, corneal pachymetry, and anterior segment at resolution of 18 μm axially by 60 μm laterally. The Visante anterior segment OCT (AS-OCT) has been proposed as a diagnostic tool to evaluate gonioscopic angle closure in patients; however, it may overestimate the frequency of closed angles compared to gonioscopy [6]. This discrepancy in findings may occur because on AS-OCT images, it is not possible to determine the location of the trabecular meshwork, and the presence of any contact between the iris and the angle wall anterior to the scleral spur is graded as angle closure. However, if this apposition did not reach the level of the posterior trabecular meshwork, the quadrant would be considered open on gonioscopy. The inability to detect the scleral spur may limit the accuracy and usefulness of angle imaging, methods as AS-OCT. Table 1 describes some instrument properties and differences among Visante, Pentacam, and Cirrus OCT.

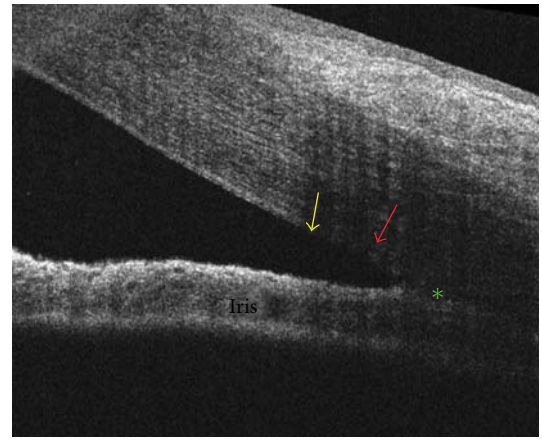

Figure 5: The Cirrus HD-OCT may enable identification of Schwalbe's line (yellow arrow), scleral spur (green asterisk), and trabecular meshwork (red arrow).

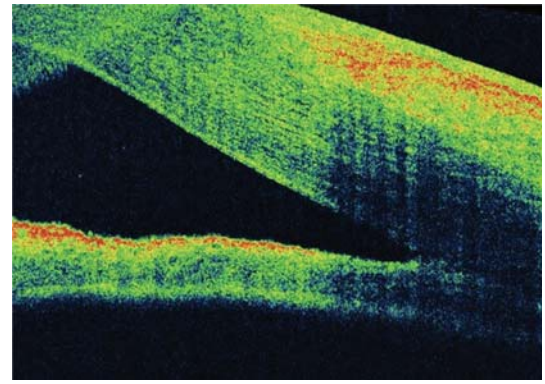

Figure 6: A 45-year-old female underwent vitrectomy plus silicone oil for retinal detachment repair. She presented with postoperative corneal edema that impaired angle examination. Cirrus OCT disclosed open anterior chamber angle.

HD-OCT applies a scanning rate 50 to 60 times faster than time-domain OCT devices and with an axial resolution of 3 to 5 μm. Cirrus HD-OCT makes images of the anterior chamber angle with higher resolution than does AS-OCT devices. With the Cirrus OCT, details of the anterior chamber angle such as the scleral spur can be viewed. The Cirrus OCT may enable identification of Schwalbe's line, scleral spur, and trabecular meshwork (Figure 5). It also assists in the diagnosis of narrow angle or anterior iris synechia (Figure 6). When analyzing the usefulness of HD-OCT in angle examination, the rate of angle closure diagnosis was lower using HD-OCT, with some eyes graded as open on

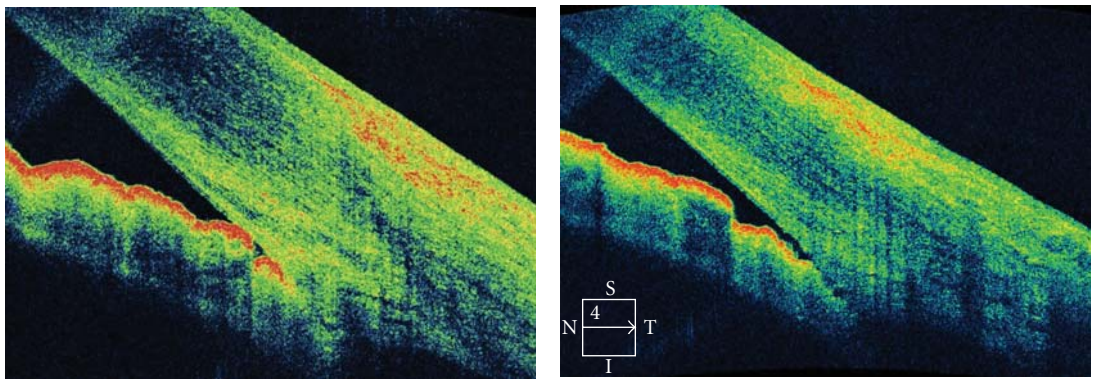

(a) (b)

Figure 7: A 49-year-old female presents with a 1-week history of pain and visual loss OS. Ophthalmic examination was unremarkable, except for angle alterations and intraocular pressure of 57 mmHg OS. There were OS areas alternating very narrow and close anterior chamber angle; OD the angle was narrow. (a) OCT examination confirmed the anterior chamber angle morphology (b) The patient underwent topical and systemic antihypertensive ocular therapy. Two days later, the intraocular pressure was 16 mmHg OS, the angle was open, confirmed by OCT exam.

HD-OCT but closed on gonioscopy. Wong et al. assessed the ability of HD-OCT with a 60-diopter aspheric lens mounted over the imaging aperture to image the anterior chamber angle [7]. Cross-sectional HD-OCT enabled visualization of the scleral spur in 71 of 90 quadrants (78.9%) and the termination of the Descemet membrane (Schwalbe's line) in 84 of 90 quadrants (93.3%). The authors concluded that the adapted HD-OCT allowed magnified views of the anterior chamber angle and provided visualization of Schwalbe's line and trabecular meshwork in most eyes. The newest version of the Cirrus software 4.0 presents improvements that appropriate anterior segment examination without the need of any lens. One recent study claimed spectral domain OCTs as the better means to identify Schwalbe's line in comparison with other devices [8]. Future studies should promote improvements in the application of HD-OCT in angle imaging for instance analysis with the 3-dimensional image of the angle.

4.2. Selected Clinical Case

Case 1. A 45-year-old female underwent vitrectomy plus silicone oil for retinal detachment repair. She presented with postoperative corneal edema and increase in intraocular pressure. The corneal edema impaired angle examination. OCT disclosed open anterior chamber angle (Figure 6).

Case 2. A 49-year-old female presents with a 1-week history of pain and visual loss OS. Her corrected visual acuity was 20/80 OS and 20/20 OD. Ophthalmic examination was unremarkable, except for angle alterations and intraocular pressure of 57 mmHg OS. There were OS areas alternating very narrow and close anterior chamber angle; OD the angle was narrow. OCT examination confirmed the anterior chamber angle morphology (Figure 7(a)). The patient underwent topical and systemic antihypertensive ocular therapy. Two days later, the intraocular pressure was 16 mmHg OS, the angle was open, confirmed by OCT exam (Figure 7(b)).

5. Final Remarks

Cirrus OCT provides relevant clinical data in regard to anterior chamber and corneal diagnosis. It enables detailed high-resolution corneal morphology analysis. It also allows anterior-chamber angle examination. OCT is a novel device to perform in vivo optical biopsies and a promising research and clinical tool for the evaluation of corneal pathologic features in a noninvasive manner. The future use of this novel technology should develop and increasingly is becoming important equipment in the clinical and surgical management of corneal, anterior chamber angle, and iridociliary diseases.

References

[1] M. Doors, T. T. J. M. Berendschot, J. de Brabander, C. A. B. Webers, and R. M. M. A. Nuijts, "Value of optical coherence tomography for anterior segment surgery," *Journal of Cataract and Refractive Surgery*, vol. 36, no. 7, pp. 1213–1229, 2010.

[2] T. Simpson and D. Fonn, "Optical coherence tomography of the anterior segment," *Ocular Surface*, vol. 6, no. 3, pp. 117–127, 2008.

[3] J. A. Izatt, M. R. Hee, E. A. Swanson et al., "Micrometer-scale resolution imaging of the anterior eye in vivo with optical coherence tomography," *Archives of Ophthalmology*, vol. 112, no. 12, pp. 1584–1589, 1994.

[4] J. L. B. Ramos, Y. Li, and D. Huang, "Clinical and research applications of anterior segment optical coherence tomography—a review," *Clinical and Experimental Ophthalmology*, vol. 37, no. 1, pp. 81–89, 2009.

[5] H. Y. Kim, D. L. Budenz, P. S. Lee, W. J. Feuer, and K. Barton, "Comparison of central corneal thickness using anterior segment optical coherence tomography vs. ultrasound pachymetry," *American Journal of Ophthalmology*, vol. 145, no. 2, pp. 228–232, 2008.

[6] L. M. Sakata, R. Lavanya, D. S. Friedman et al., "Comparison of gonioscopy and anterior-segment ocular coherence tomography in detecting angle closure in different quadrants of the anterior chamber angle," *Ophthalmology*, vol. 115, no. 5, pp. 769–774, 2008.

[7] H. T. Wong, M. C. Lim, L. M. Sakata et al., "High-definition optical coherence tomography imaging of the iridocorneal angle of the eye," *Archives of Ophthalmology*, vol. 127, no. 3, pp. 256–260, 2009.

[8] T. Jing, P. Marziliano, and H. T. Wong, "Automatic detection of Schwalbe's line in the anterior chamber angle of the eye using HD-OCT images," in *Proceedings of the 32nd Annual International Conference of the IEEE Engineering in Medicine and Biology Society (EMBC '10)*, pp. 3013–3016, September 2010.

Hindawi Publishing Corporation
Journal of Ophthalmology
Volume 2012, Article ID 959721, 5 pages
doi:10.1155/2012/959721

Clinical Study

Comparison of Macular Thickness in Diabetic Macular Edema Using Spectral-Domain Optical Coherence Tomography and Time-Domain Optical Coherence Tomography

Masashi Kakinoki, Taichirou Miyake, Osamu Sawada, Tomoko Sawada, Hajime Kawamura, and Masahito Ohji

Department of Ophthalmology, Shiga University of Medical Science, Seta-Tsukinowa-cho, 520-2192 Otsu, Japan

Correspondence should be addressed to Masashi Kakinoki, kakinoki.masashi@gmail.com

Received 4 April 2011; Revised 22 September 2011; Accepted 14 October 2011

Academic Editor: Eduardo Buchele Rodrigues

Purpose. To compare the macular thicknesses in diabetic macular edema (DME) measured with spectral-domain optical coherence tomography (SD-OCT) and time-domain (TD) OCT. *Patients and Methods.* The average macular thicknesses of 50 eyes of 29 patients with DME were measured using SD-OCT and TD-OCT. *Results.* The mean macular thicknesses measured with TD-OCT and SD-OCT were 401.5 ± 117.8 μm (mean ± SD) and 446.2 ± 123.5 μm, respectively. The macular thicknesses measured with the two devices were well correlated (Pearson's product moment correlation, $r = 0.977$, $P < 0.001$). A significant correlation was found between the best-corrected visual acuity and the retinal thickness measured by TD-OCT and SD-OCT (Pearson's product moment correlation, TD-OCT, $r = 0.34$; $P < 0.05$; SD-OCT, $r = 0.32$; $P < 0.05$). *Discussion.* The mean macular thickness measured with SD-OCT was about 45 μm thicker than that measured with TD-OCT. Attention should be paid when comparing data obtained using different OCT machines.

1. Introduction

Optical coherence tomography (OCT), which provides B-mode retinal images, has become essential for diagnosing retinal disease and glaucoma [1–9] since the technology was first reported by Huang et al. in 1991 [10]. OCT also provides quantitative retinal thickness data, which are useful to monitor retinal changes in clinical and research settings [3].

Time-domain OCT (TD-OCT) includes an interferometer that measures the echo delay time of light that is reflected and backscattered from various retinal microstructures. The echo time delays of light beam reflected from the retinal microstructure are compared with the echo time delays of the same light beam reflected from a reference mirror at known distances. The TD method samples only one point at a time. Therefore, it takes a relatively long time to obtain A-scan and B-mode retinal images, and it is almost impossible to obtain a three-dimensional retinal image.

In spectral-domain OCT (SD-OCT), light beams returning from the sample and reference paths are combined at the detector, a spectrometer that resolves the interference signals throughout the depth of each A-scan without varying the length of the reference path. This is possible because the spectrometer resolves the relative amplitudes and phases of the spectral components backscattered from all depths of each A-scan simultaneously using the Fourier transformation. This allows SD-OCT to acquire retinal images about 50 times faster compared with TD-OCT [11]. The substantial increase in scan speed allows acquisition of three-dimensional data sets.

A few studies have compared the macular thicknesses of patients with diabetic macular edema (DME) obtained with TD-OCT and SD-OCT [12, 13]. We compared the retinal thickness measurements obtained with the two OCT devices in subjects with DME to understand the differences in measurements between the two OCTs. We already reported the difference in mean retinal thickness between TD-OCT and SD-OCT in normal eyes [14]. To the best of our knowledge, the current study is the first to compare the macular thickness measurements from the two OCT devices between normal subjects and patients with DME.

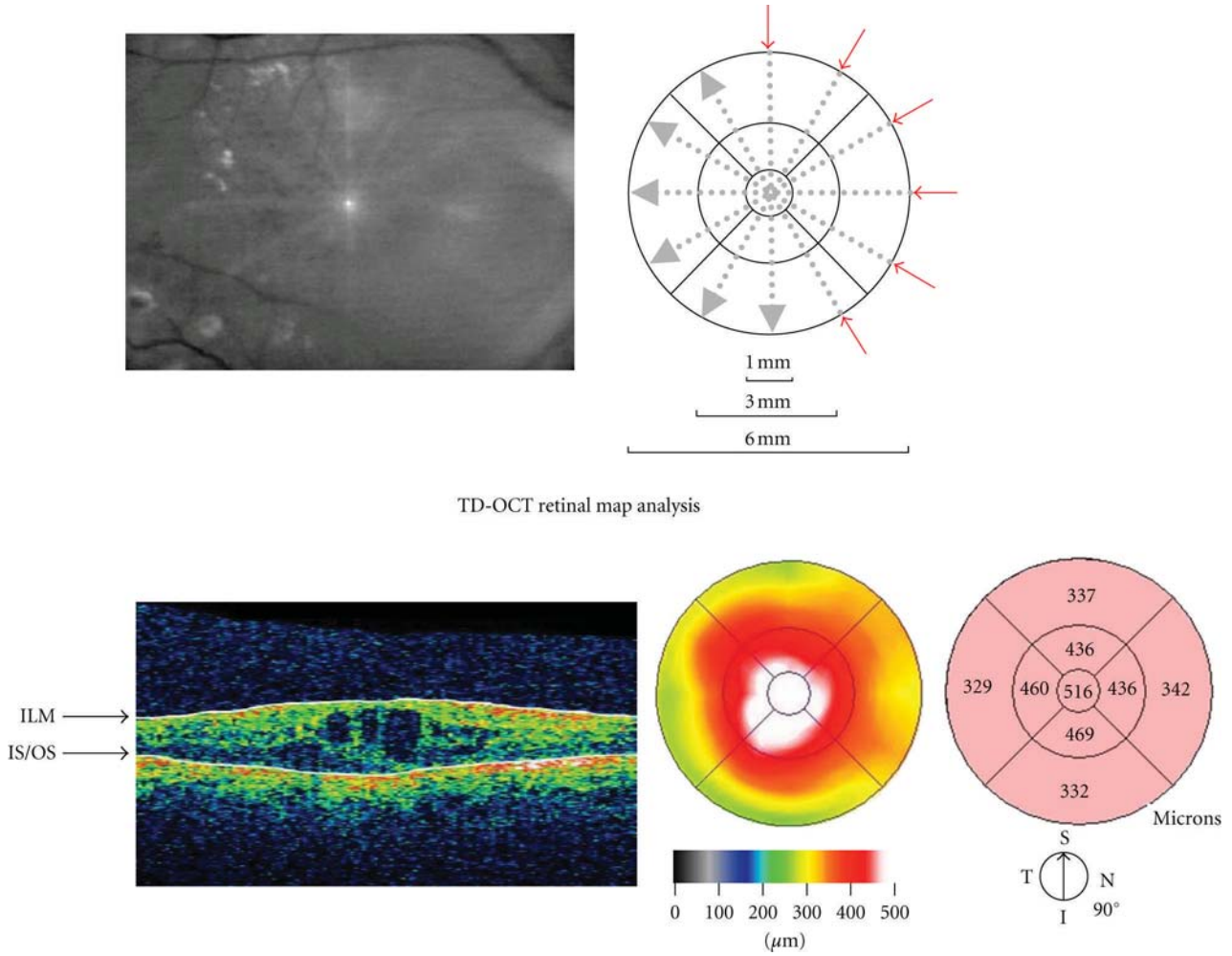

Figure 1: (Top) Fast macular thickness scan pattern with TD-OCT. (Bottom) The mean retinal thickness at the central 1 mm circle is 516 μm in a 74-year-old man.

2. Patients and Methods

The macular thickness was measured in 50 eyes of 29 patients with DME using TD-OCT (Stratus OCT, Carl Zeiss Meditec, Dublin, CA, USA) and SD-OCT (Cirrus HD-OCT, Carl Zeiss Meditec, Dublin, CA, USA) to determine a correlation between the devices. The mean patient age was 68.0 ± 9.0 years (range, 45–85 years). Of the 29 subjects with DME, 18 were men and 11 were women.

With TD-OCT, the macular thickness data were obtained using the fast macular thickness scan pattern (Figure 1). This scan pattern acquires six linear B-scans in a continuous, automated sequence. The scans are centered at the fovea in a radial pattern and separated by 30-degree increments. Each B-scan consists of 128 A-scans. The axial resolution of TD-OCT is less than 10 μm according to the manufacturer's data.

The Macular Cube 200 × 200 scan pattern in SD-OCT generates a data cube through a 6 mm square grid by acquiring a series of 200 horizontal scan lines, each comprised of 200 A-scans (Figure 2) with an axial resolution of 5 μm.

The average retinal thickness at the central 1 mm area was analyzed with both OCT machines. About 128 points were measured within a 1 mm circle with TD-OCT and about 872 points with SD-OCT.

Three operators measured the macular thickness of each subject using the two OCT instruments on the same day. Apparent segmentation failures in TD-OCT and SD-OCT were excluded from this study.

The best-corrected visual acuities (BCVAs) were obtained in decimal VA and converted to logarithm of the minimum angle of resolution (log MAR) for statistical analysis.

3. Results

The mean macular thicknesses in patients with DME measured with TD-OCT was 401.5 ± 117.8 μm (mean ± SD; range, 203–712 μm) and with SD-OCT 446.2 ± 123.5 μm; range, 245–775 μm). The mean macular thickness with SD-OCT was 44.7 μm thicker than that with TD-OCT, which was a significant difference ($P < 0.001$, paired t-test). The

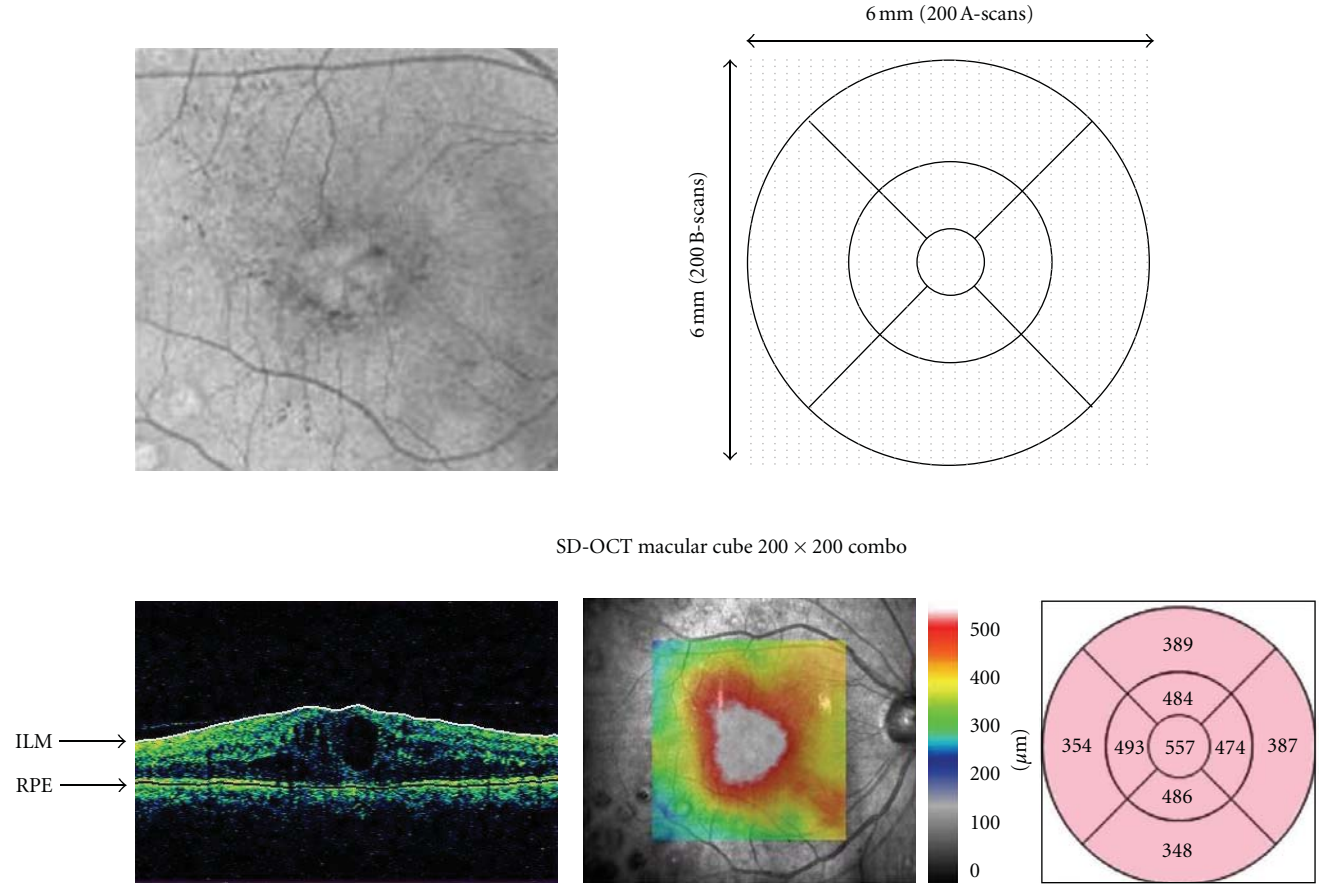

Figure 2: (Top) Macular cube 200 × 200 mode with SD-OCT. (Bottom) The mean retinal thickness at the central 1 mm circle is 557 μm in the same 74-year-old man.

macular thickness measured with TD-OCT correlated well with that measured with SD-OCT (Pearson's product moment correlation, $r = 0.977$, $P < 0.001$) (Figure 3).

A representative case was that of a 75-year-old man with DME. TD-OCT traced the ILM and IS/OS line automatically, and the central retinal thickness was 543 μm (Figure 4(a)). SD-OCT traced the ILM and RPE automatically, and the central retinal thickness was 567 μm (Figure 4(b)), which was 24 μm thicker than the TD-OCT measurement. Compared with the five-line mode of the SD-OCT (Figure 4(c)), the true IS/OS line of the TD-OCT may be the pale line that is defined by the arrowheads (Figure 4(a)). If TD-OCT automatically traced the true IS/OS line, the central retinal thickness would be thinner than 543 μm. We assumed that the retinal thickness using TD-OCT was thicker than the actual retinal thickness, and as a result, the difference in the retinal thicknesses between the two machines was small. This is one reason that the macular thickness in normal subjects is about 15 μm thicker than in patients with DME.

The relationship between the BCVA and the retinal thickness also was evaluated, and a significant correlation was found between the two devices (Pearson's product moment correlation, TD-OCT, $r = 0.34$; $P < 0.05$; SD-OCT, $r = 0.32$; $P < 0.05$) (Figure 5).

4. Discussion

In the current study, the average retinal thickness measured with TD-OCT was 401.5 ± 117.8 μm and with SD-OCT 446.2 ± 123.5 μm, a difference of about 45 μm. The difference in the average retinal thicknesses between the devices appears to have resulted from the different definitions of the retinal thicknesses. TD-OCT defines retinal thickness as the distance from the surface of the inner limiting membrane (ILM) to the boundary between the inner and outer segments of the photoreceptors (IS/OS). SD-OCT defines the retinal thickness as the distance from the surface of the ILM to the surface of the retinal pigment epithelium (RPE). The different algorisms explain the different results. Lammer et al. compared the retinal thickness of DME between TD-OCT and SD-OCT and reported mean difference was 58.5 μm [12]. Forooghian et al. also reported that the mean difference of the two machines was 53.0 μm [15]. These results were almost same as our result, and they suggested that different algorisms make the different results. Attention should be paid to the retinal thickness when data from different machines are compared, although the retinal thickness in patients with DME measured by SD-OCT correlated strongly with that measured by TD-OCT.

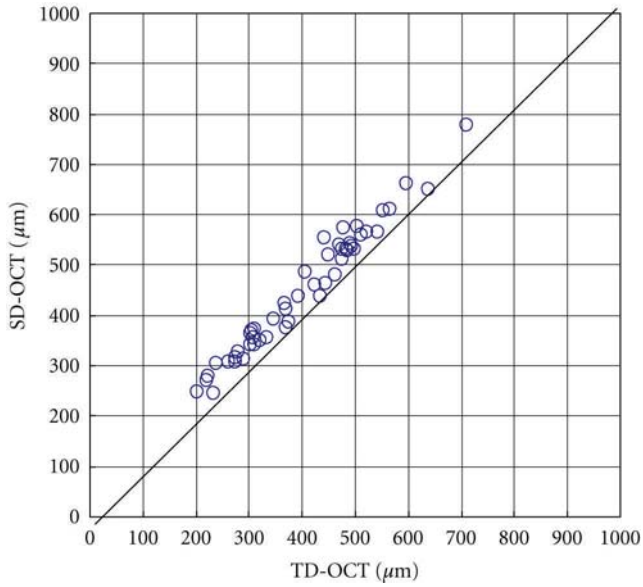

Figure 3: The difference between TD-OCT and SD-OCT average retinal thicknesses in patients with DME in a central 1 mm area is about 45 μm. These two data sets are well correlated (correlation coefficient, 0.977, $P < 0.001$, Pearson's product moment correlation).

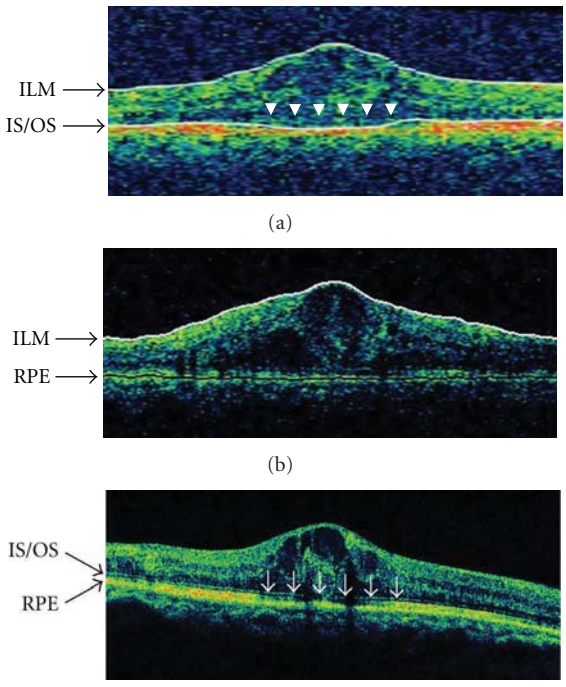

Figure 4: The ILM and IS/OS are traced by a white line using TD-OCT, although the true IS/OS line is thought to be that indicated by the arrowheads in the retinal thickness mode (a). The ILM and RPE are traced by a white and black line by the macular thickness mode of SD-OCT (b). The IS/OS line is indicated by a vague line in the five-line mode (arrowheads) (c).

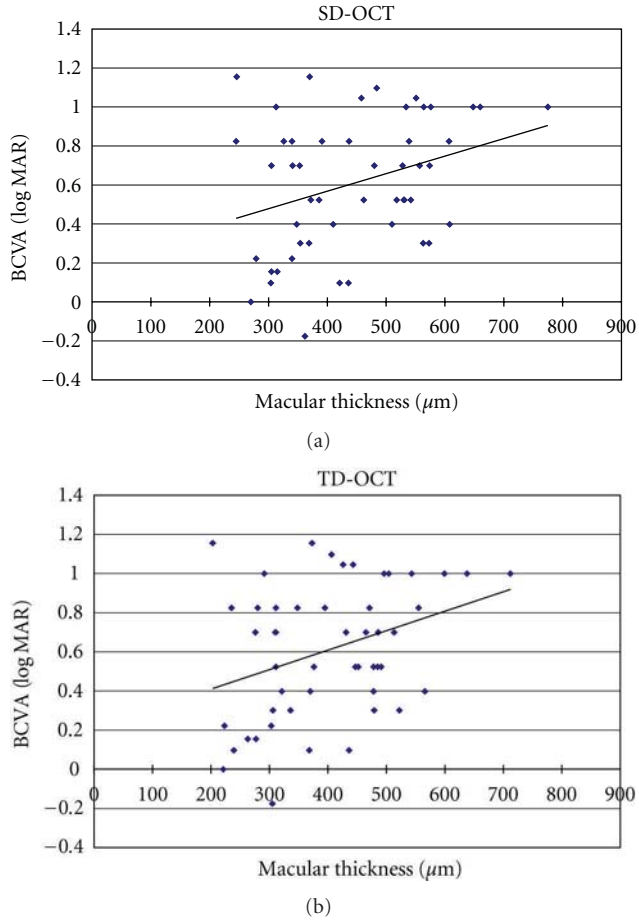

Figure 5: There is a significant correlation between TD-OCT (b) and SD-OCT (a) relationship for the BCVA and the retinal thickness (Pearson's product moment correlation, TD-OCT, $r = 0.34$, $P < 0.05$; SD-OCT, $r = 0.32$, $P < 0.05$).

We reported previously that when using SD-OCT in normal subjects, the macula was 60 μm thicker than when measured with TD-OCT [14]. In the current study, when using SD-OCT in subjects with DME, the macula was 45 μm thicker than when measured with TD-OCT. The difference in the macular thickness between TD-OCT and SD-OCT in normal subjects was about 15 μm thicker than that in patients with DME. With TD-OCT, the fast macular thickness scan pattern acquires six linear B-scans in a continuous automated sequence. The scans are centered at the fovea in a radial pattern and separated by 30-degree increments. With SD-OCT, the Macular Cube 200×200 scan pattern generates a data cube through a 6 mm square grid by acquiring a series of 200 horizontal scan lines, each comprised of 200 A-scans. The average retinal thickness at the central 1 mm circle was about 128 points with TD-OCT and about 872 points with SD-OCT. Compared with TD-OCT, the higher reliability of SD-OCT is based on the uniformity and the larger number of scan points. The scan pattern and the scan accuracy may explain the difference in the macular thickness between normal subjects and DME.

Using TD-OCT, the IS/OS line disappeared in some areas or was not clearly detected in some cases. The measurement line was not traced on IS/OS and traced on the RPE line. This may result in a thicker measurement than the actual thickness on TD-OCT.

As in previous studies, we also found a correlation between the macular thickness and BCVA in subjects with DME [16, 17]. The Diabetic Retinopathy Clinical Research Network reported that the relationship between the VA and central retinal thickness measured by OCT was linear [16]. However, Koleva-Georgieva and Sivkova reported no correlation between the BCVA and retinal thickness [18], which may have resulted from the small number of subjects and that six of nine eyes had macular ischemia. The low VA could be due to the serous macular detachment with large cystoid spaces and the presence of macular ischemia.

In conclusion, the mean retinal thickness in patients with DME measured with SD-OCT was about 45 μm thicker than that with TD-OCT. Care should be taken when comparing retinal thicknesses between the two OCT machines.

Conflict of Interests

The authors have no proprietary interest in any aspect of this paper.

Acknowledgments

This paper is supported in part by a grant from the Ministry of Education, Culture, Sports, Science and Technology of Japan (#18591915) and a grant from the Ministry of Health, Labor and Welfare.

References

[1] G. J. Jaffe and J. Caprioli, "Optical coherence tomography to detect and manage retinal disease and glaucoma," *American Journal of Ophthalmology*, vol. 137, no. 1, pp. 156–169, 2004.

[2] B. Haouchine, P. Massin, R. Tadayoni, A. Erginay, and A. Gaudric, "Diagnosis of macular pseudoholes and lamellar macular holes by optical coherence tomography," *American Journal of Ophthalmology*, vol. 138, no. 5, pp. 732–739, 2004.

[3] T. Otani, S. Kishi, and Y. Maruyama, "Patterns of diabetic macular edema with optical coherence tomography," *American Journal of Ophthalmology*, vol. 127, no. 6, pp. 688–693, 1999.

[4] T. Iida, N. Hagimura, T. Sato, and S. Kishi, "Evaluation of central serous chorioretinopathy with optical coherence tomography," *American Journal of Ophthalmology*, vol. 129, no. 1, pp. 16–20, 2000.

[5] T. Alasil, P. A. Keane, J. F. Updike et al., "Relationship between optical coherence tomography retinal Parameters and visual acuity in diabetic macular edema," *Ophthalmology*, vol. 117, no. 12, pp. 2379–2386, 2010.

[6] T. Sato, T. Iida, N. Hagimura, and S. Kishi, "Correlation of optical coherence tomography with angiography in retinal pigment epithelial detachment associated with age-related macular degeneration," *Retina*, vol. 24, no. 6, pp. 910–914, 2004.

[7] R. Chaudhary, R. Arora, D. K. Mehta, and M. Singh, "Optical coherence tomography study of optic disc melanocytoma," *Ophthalmic Surgery Lasers and Imaging*, vol. 37, no. 1, pp. 58–61, 2006.

[8] V. Gupta, A. Gupta, M. R. Dogra, and A. Agarwal, "Optical coherence tomography in group 2A idiopathic juxtafoveolar telangiectasis," *Ophthalmic Surgery Lasers and Imaging*, vol. 36, no. 6, pp. 482–486, 2005.

[9] P. J. Rosenfeld, A. A. Moshfeghi, and C. A. Puliafito, "Optical coherence tomography findings after an intravitreal injection of bevacizumab (Avastin) for neovascular age-related macular degeneration," *Ophthalmic Surgery Lasers and Imaging*, vol. 36, no. 4, pp. 331–335, 2005.

[10] D. Huang, E. A. Swanson, C. P. Lin et al., "Optical coherence tomography," *Science*, vol. 254, no. 5035, pp. 1178–1181, 1991.

[11] M. Wojtkowski, T. Bajraszewski, P. Targowski, and A. Kowalczyk, "Real-time in vivo imaging by high-speed spectral optical coherence tomography," *Optics Letters*, vol. 28, no. 19, pp. 1745–1747, 2003.

[12] J. Lammer, C. Scholda, C. Prünte, T. Benesch, U. Schmidt-Erfurth, and M. Bolz, "Retinal thickness and volume measurements in diabetic macular edema: a comparison of four optical coherence tomography systems," *Retina*, vol. 31, no. 1, pp. 48–55, 2011.

[13] S. Modjtahedi, C. Chiou, B. Modjtahedi, D. G. Telander, L. S. Morse, and S. S. Park, "Comparison of macular thickness measurement and segmentation error rate between stratus and fourier-domain optical coherence tomography," *Ophthalmic Surgery Lasers and Imaging*, vol. 41, no. 3, pp. 301–310, 2010.

[14] M. Kakinoki, O. Sawada, T. Sawada, H. Kawamura, and M. Ohji, "Comparison of macular thickness between cirrus HD-OCT and stratus OCT," *Ophthalmic Surgery Lasers and Imaging*, vol. 40, no. 2, pp. 135–140, 2009.

[15] F. Forooghian, C. Cukras, C. B. Meyerle, E. Y. Chew, and W. T. Wong, "Evaluation of time domain and spectral domain optical coherence tomography in the measurement of diabetic macular edema," *Investigative Ophthalmology and Visual Science*, vol. 49, no. 10, pp. 4290–4296, 2008.

[16] Diabetic Retinopathy Clinical Research Network, "Relationship between optical coherence tomography-measured central retinal thickness and visual acuity in diabetic macular edema," *Ophthalmology*, vol. 114, no. 3, pp. 525–536, 2007.

[17] S. W. Kang, C. Y. Park, and D. I. Ham, "The correlation between fluorescein angiographic and optical coherence tomographic features in clinically significant diabetic macular edema," *American Journal of Ophthalmology*, vol. 137, no. 2, pp. 313–322, 2004.

[18] D. Koleva-Georgieva and N. Sivkova, "Assessment of serous macular detachment in eyes with diabetic macular edema by use of spectral-domain optical coherence tomography," *Graefe's Archive for Clinical and Experimental Ophthalmology*, vol. 247, no. 11, pp. 1461–1469, 2009.

Hindawi Publishing Corporation
Journal of Ophthalmology
Volume 2012, Article ID 347206, 4 pages
doi:10.1155/2012/347206

Case Report

Topographical Choroidal Thickness Change Following PDT for CSC: An OCT Case Report

William J. Wirostko,[1] Rick N. Nordgren,[1] and Adam M. Dubis[2]

[1] *Department of Ophthalmology, The Eye Institute, Medical College of Wisconsin, 925 North 87th Street, Milwaukee, WI 53226, USA*
[2] *Department of Cell Biology Neurobiology and Anatomy, Medical College of Wisconsin, 8700 West Wisconsin Avenue, Milwaukee, WI 53226, USA*

Correspondence should be addressed to William J. Wirostko, wirostko@mcw.edu

Received 11 February 2011; Revised 30 March 2011; Accepted 11 October 2011

Academic Editor: Stefan Mennel

Purpose. To describe topographical changes in choroidal thickness as measured by optical coherence tomography following photodynamic therapy (PDT) for central serous chorioretinopathy (CSC). *Methods*. Case report. *Results*. By 1 month following PDT, mean (SD) choroidal thickness decreased from 562 microns (24) to 424 microns (27) ($P < 0.01$) at 3 mm temporal to fovea, 483 microns (9) to 341 microns (21) ($P < 0.01$) at 1.5 mm temporal to fovea, 576 microns (52) to 370 microns (81) ($P < 0.01$) under the fovea, 442 microns (30) to 331 microns (54) ($P < 0.04$) at 1.5 mm nasal to fovea, and 274 microns (39) to 171 microns (17) ($P < 0.01$) at 3 mm nasal to fovea. The Location of greatest choroidal thickness (648 microns) prior to treatment was at point of leakage on fluorescein angiogram (FA). This region decreased to 504 microns following treatment. *Conclusion*. A decrease in choroidal thickness can be seen following PDT for CSC as far as 3 mm temporal and 3 mm nasal to fovea. The Location of greatest choroidal thickness may be at point of leakage on FA.

1. Introduction

Central serous chorioretinopathy (CSC) is characterized by a neurosensory retinal detachment in the posterior fundus associated with one or more leaks at the level of the retinal pigment epithelium (RPE) [1]. Etiology of leakage is unclear but thought to be related to hyperpermeability of the choroidal vasculature. Although many cases of CSC resolve spontaneously with improvement of vision, treatment may be considered for eyes with persistent or progressive vision loss from serous retinal detachment. Current treatment options include thermal laser photocoagulation or photodynamic therapy (PDT) with verteporfin (QLT Ophthalmics, Inc. Menlo Park, CA, USA) [1, 2].

Optical coherence tomography (OCT) is an imaging modality capable of depicting the retinochoroidal layers and the presence of a neurosensory retinal detachment in eyes with CSC [3]. In a recent OCT study, subfoveal choroidal thickness was shown to decrease following PDT for CSC [4]. However, the topographical location and extent of choroidal thickness changes following PDT for CSC were not described. In this paper, we describe a case report of topographic choroidal changes as measured by raster lines on spectral domain OCT following PDT for CSC. Findings are also described in relation to fluorescein angiography (FA) findings.

2. Material and Methods

A retrospective case study of a patient receiving PDT with Visudyne for CSC was performed. Medical records were reviewed for clinical findings, FA results, OCT findings, and PDT treatment parameters. Outcome parameters included visual acuity, clinical findings, and choroidal thickness as measured by OCT images. Choroidal thickness measurements were obtained by exporting all OCT images into Image J (http://rsb.info.nih.gov/ij/) where number of pixels in choroidal layer was counted and converted into microns using micron/pixel ratio. All measurements were performed

by one grader (RNN). The authors are not aware of any automated method to measure topographical choroidal thickness. Statistical analysis using the Mann-Whitney test was used to compare choroidal thickness before and after treatment at 3 mm temporal to the fovea, 1.5 mm temporal to the fovea, under the fovea, 1.5 mm nasal to the fovea, and 3 mm nasal to the fovea. Data set for each of these five locations was obtained from 5 horizontal raster scans (Figure 3).

3. Results

A 52-year-old woman presented for decreased vision in her right eye of 1-month duration. Visual acuity was 20/60 OD and 20/20 OS. Fundus exam of OD revealed a neurosensory detachment of the fovea with abnormalities of the retinal pigment epithelium (RPE) just superonasal to the fovea. Fluorescein angiography depicted leakage superonasal to the fovea at the level of the RPE with pooling into the neurosensory space (Figure 1). Spectral domain OCT using Cirrus HD-OCT (Carl Zeiss Meditec, Inc., Dublin, CA, JUSA) demonstrated a neurosensory detachment of the fovea (Figure 2). Five 6 mm long horizontal raster lines centered on the fovea and spaced 0.25 mm apart were obtained to topographically map the choroidal thickness. Mean (SD) choroidal thickness was 562 microns (24) at 3 mm temporal to fovea, 483 microns (9) at 1.5 mm temporal to fovea, 576 microns (52) under the fovea, 442 microns (30) at 1.5 mm nasal to fovea, and 274 microns (39) at 3 mm nasal to fovea. Thickest area of choroid (648 microns) was under area of leakage as seen on FA (Figure 3). Diagnosis of CSC was established, and treatment with PDT was recommended. After discussing the off-label nature of PDT for CSC, patient chose to proceed with treatment. Photodynamic therapy with verteporfin using 1.5 mm laser spot size, standard treatment parameters, and 83 seconds of duration was applied to juxtafoveal area of leakage as guided by FA [5]. Care was taken to avoid directly treating the fovea (Figure 1).

At 1 month following treatment, visual acuity improved to 20/20. Optical coherence tomography demonstrated resolution of subretinal fluid. Mean (SD) posttreatment choroidal thickness measurements were 424 microns (27) at 3 mm temporal to fovea, 341 microns (21) at 1.5 mm temporal to fovea, 370 microns (81) under the fovea, 331 microns (54) at 1.5 mm nasal to fovea, and 171 microns (17) at 3 mm nasal to fovea (Figure 3). This reduction was statistically significant ($P < 0.01$, $P < 0.01$, $P < 0.01$, $P < 0.04$, $P < 0.01$) at each location, respectively, using the Mann-Whitney test (Figure 4). Point of prior greatest choroidal thickness (648 microns) decreased to 504 microns, but was still the point of greatest choroidal thickness (Figure 3).

4. Discussion

This study describes topographical thickness changes in the choroidal layer using OCT for an eye with CSC undergoing PDT with verteporfin. Thickness changes are described with regard to FA findings and treatment location. The authors are not aware that this has been previously described. Prior reports on choroidal thickness in CSC have only described subfoveal thickness findings with no reference to location of FA leakage or PDT laser spot. Understanding the topographic changes of the choroid following PDT for CSC may be important, both for advancing our understanding of CSC and also improving our ability to restore vision.

Our findings of decreased choroidal thickness following PDT concur with prior reports [4]. In 2010, Maruko et al. found subfoveal choroidal thickness decreased from 389 ± 106 micron at baseline to 330 ± 103 microns at one month [4]. Our patient's mean (SD) subfoveal choroidal thickness decreased from 576 microns (52) to 370 microns (81) ($P < 0.01$ Mann-Whitney test). Interestingly, our report suggests that the reduction in choroidal thickness is diffuse and extends further than just under the fovea as previously reported. We measured a statistically significant reduction in choroidal thickness from up to 3 mm temporal of the fovea to 3 mm nasal of the fovea following a 1.5 mm juxtafoveal PDT laser spot applied to an area of juxtafoveal leakage as seen on FA (Figure 4). It remains unclear whether a similar diffuse effect or as significant of an effect would occur if the PDT

Figure 1: Fluorescein angiography of right eye demonstrating hyperfluorescence and leakage at level of RPE. White circle depicts the area of fundus treated with PDT (1.5 mm laser spot).

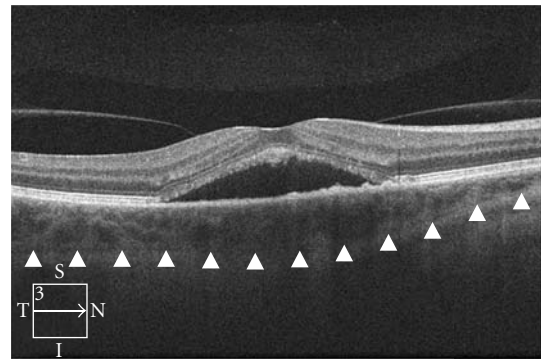

Figure 2: OCT image of retina and choroid prior to treatment demonstrating neurosensory retinal detachment. Arrowheads mark outer boundary of choroid used to measure choroidal thickness.

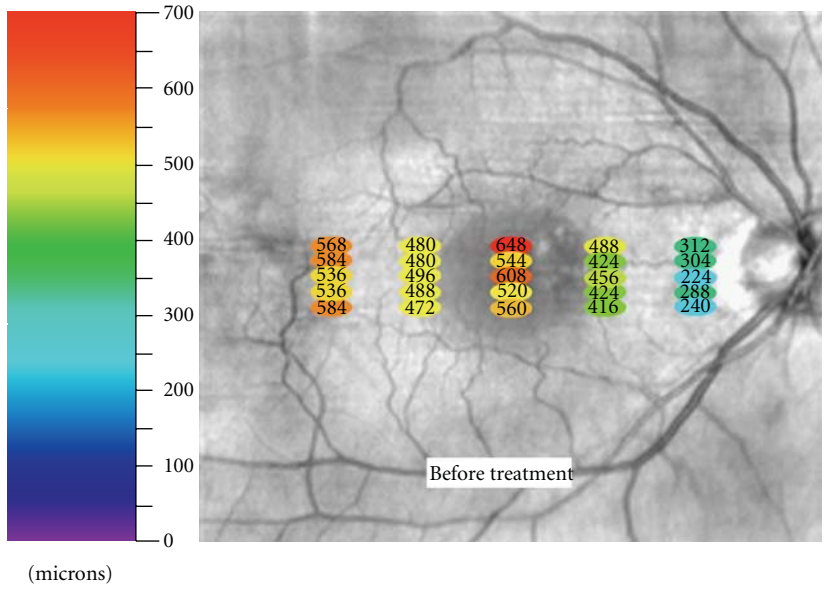

(a)

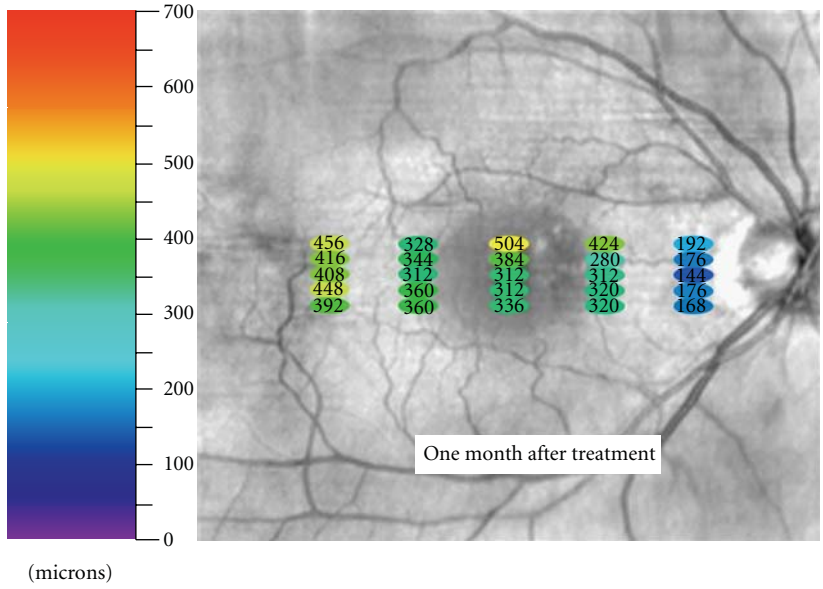

(b)

Figure 3: Fundus photograph of OD demonstrating thickness of choroid in microns at each specific measured point both before and after treatment.

laser spot was not applied over the leakage as seen on FA. Distinguishing these effects may be important for some cases, especially when FA leakage is subfoveal and the treating physician wishes to avoid exposing the fovea to PDT laser.

It is interesting to observe that the single thickest measurement of the choroid (648 microns) before treatment was in the area of leakage as seen on FA. Following treatment, this single location decreased to 504 microns but was still the point of greatest choroidal thickness (Figure 3). Unfortunately, the authors cannot comment on how abnormal either of these measurements is since complete normative data on choroidal thickness correcting for age, race, refractive area, and fundus location is not available [6].

Limitations of our study include the single sample size, the retrospective nature, short duration of follow-up, and limited sampling of choroid. Additionally, indocyanine green angiography which can provide information on choroidal hyperpermeability was not obtained on this patient. Nonetheless, the authors feel publishing this case is valuable since its unique combination of small focal juxtafoveal leakage on FA and small PDT laser spot allows us to make some interesting observations. Certainly, further studies are needed to corroborate our findings.

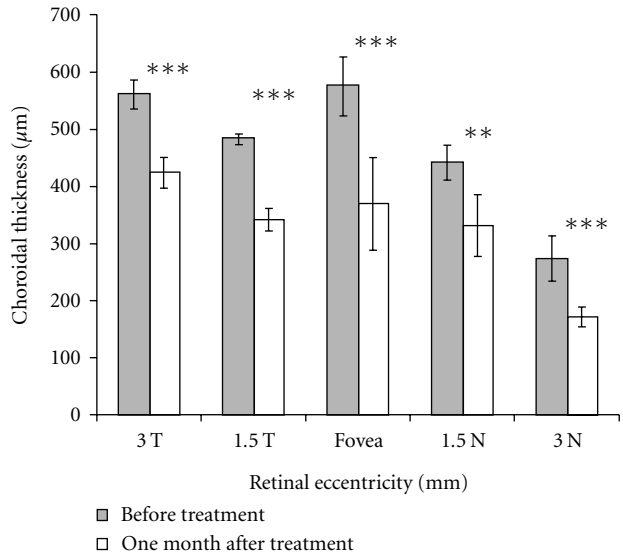

Figure 4: Chart comparing thickness of choroid at 3 mm temporal to fovea, 1.5 mm temporal to fovea, under the fovea, 1.5 mm nasal to fovea, and 3 mm nasal to fovea before and after treatment with PDT. Error bars represent one standard deviation. At all points, there was a significant reduction in choroidal thickness (the Mann-Whitney test): $^{***}P < 0.01$, $^{**}P < 0.04$.

5. Conclusion

This study documents the topographical changes in the choroidal layer as measured with OCT in an eye undergoing treatment with PDT and verteporfin for CSC. A reduction in choroidal thickness was observed as far away as 3 mm temporal and nasal to the area of leakage as seen on FA following treatment. Point of greatest choroidal thickness before and after treatment was in the area of leakage on FA.

Disclosure

The authors have no proprietary interest in any aspect of this study.

Acknowledgments

The authors wish to thank Joe Carroll, PhD (Medical College of Wisconsin, Milwaukee, WI, USA) for assistance with analyzing the OCT images and for his helpful comments on this manuscript. This paper is supported in part by an unrestricted grant from the Research to Prevent Blindness, Inc., New York, NY, USA.

References

[1] C. M. Klais, M. D. Ober, A. P. Ciardella, and L. A. Yannuzzi, "Central serous chorioretinopathy," in *Retina*, S. J. Ryan, D. R. Hinton, A. P. Schachat, and C. P. Wilkinson, Eds., vol. 2, pp. 1135–1161, Elsevier Mosby, Philadelphia, Pa, USA, 4th edition, 2006.

[2] W. M. Chan, T. Y. Lai, R. Y. Lai et al., "Photodynamic therapy for chronic central serous chorioretniopathy," *Retina*, vol. 23, pp. 752–763, 2003.

[3] Y. Imamura, T. Fujiwara, R. Margolis, and R. F. Spaide, "Enhanced depth imaging optical coherence tomography of the choroid in central serous chorioretinopathy," *Retina*, vol. 29, no. 10, pp. 1469–1473, 2009.

[4] I. Maruko, T. Iida, Y. Sugano, A. Ojima, M. Ogasawara, and R. F. Spaide, "Subfoveal choroidal thickness after treatment of central serous chorioretinopathy," *Ophthalmology*, vol. 117, no. 9, pp. 1792–1799, 2010.

[5] N. M. Bressler, "Treatment of ARMD with PDT study group. Photodynamic therapy of subfoveal choroidal neovascularization in age-related macular degeneration with verteporfin: two year results of 2 randomized clinical trials-tap report 2," *Archives of Ophthalmology*, vol. 123, no. 9, pp. 1283–1285, 2005.

[6] R. Margolis and R. F. Spaide, "A pilot study of enhanced depth imaging optical coherence tomography of the choroid in normal eyes," *American Journal of Ophthalmology*, vol. 147, no. 5, pp. 811–815, 2009.

Hindawi Publishing Corporation
Journal of Ophthalmology
Volume 2011, Article ID 725362, 4 pages
doi:10.1155/2011/725362

Clinical Study

Spectral Domain OCT: An Aid to Diagnosis and Surgical Planning of Retinal Detachments

Graham Auger and Stephen Winder

Department of Ophthalmology, Royal Hallamshire Hospital, Glossop Road, South Yorkshire, Sheffield S10 2JF, UK

Correspondence should be addressed to Stephen Winder, stephen.winder@sth.nhs.uk

Received 6 April 2011; Revised 29 August 2011; Accepted 20 September 2011

Academic Editor: Eduardo Buchele Rodrigues

Regmatogenous retinal detachments need prompt intervention particularly when macula is on. Unfortunately this is not always easy to ascertain clinically and the chronicity of the event is often muddled in patient's histories. Developments in optical coherence tomography (OCT) have allowed high-resolution axial scans which have enabled the characterisation of retinal changes in retinal detachments. In this paper, we show the changes in retinal morphology observed by spectral domain OCT and how this can be used to plan appropriate surgical intervention.

1. Introduction

Rhegmatogenous retinal detachments referred in an acute nature require prompt surgical repair. However, studies have shown that surgery is best done during normal working hours [1]. Given the pressures on theatre use it is important to be able to assess the retinal detachment and to ascertain the urgency of planning surgical intervention. One of the most important features is the involvement of the macula and fovea that is macula on or macula off. In cases of macula-off retinal detachments, visual outcome is less dependent on prompt surgery and surgical correction can be delayed [1]. Macula-on retinal detachments, however, should have their surgery expedited, the main concern being the conversion to a macula-off situation which has a much poorer visual prognosis [1].

The assessment of rhegmatogenous retinal detachments is multifactorial; in an otherwise normal eye visual acuity is an easy measure of macula involvement with the 6/60 patient being macula off and 6/6 macula on [1]. Similarly the onset of symptoms and the age of the retinal detachment is important, as chronic detachments can be more stable and surgery can be safely delayed [1]. Also the extent of detachment and position of the retinal break can also help predict the progression of an acute macula on retinal detachment [1]. However, in certain situations the macula-on or macula-off question is not easily answered; visual acuities may be misleading; examination of the detachment may be difficult due to poor views often due to vitreous hemorrhage and chronicity may be difficult to ascertain in patients with vague histories.

High-speed spectral domain optical coherence tomography (OCT) offers a noninvasive tool to evaluate retinal microstructural changes in a number of eye pathologies. Newer systems using spectral domain calculations have improved data acquisition speeds compared with conventional time-domain OCT equipment allowing much greater axial resolution [2]. Given the greater resolution a number of characteristic changes seen in retinal detachment have been observed. In this paper, we discuss two cases where spectral domain OCT and an understanding of the histological changes have enabled a clearer diagnosis and planning of treatment.

2. Case 1

Our first case is a seventy-five-year-old gentleman who presented with a vague history of blurred vision for six weeks. Visual acuity was 6/24 and examination revealed a pseudophakic inferotemporal macula-off retinal detachment. The reduction in visual acuity was thought to be secondary to

vitreous haemorrhage as biomicroscopy assessment showed the detachment stopping inferior to the macula (Figure 1).

To confirm the macula status, a microstructural imaging analysis was performed using the Heidelberg Spectralis OCT scanner. Contrary to the biomicroscopy examination (Figure 1), this revealed a macula-off retinal detachment (Figure 2). Changes seen in the OCT scan were characteristic of an old retinal detachment with the presence of intraretinal cysts, undulation of outer retinal layers, and the hyperreflectivity in the photoreceptor layer (Figure 2). Secondary to these OCT findings, the surgical session was deprioritised and performed five days later. The surgical repair consisted of a three-port pars plana vitrectomy with perfluoropropane tamponade and cryotherapy. Postoperative visual outcome was good being 6/9 two months after surgery. Subsequent spectralis OCT one year following the retinal detachment shows restoration of normal retinal morphology with resolution of the intraretinal cysts, flattening of the retinal layers, and no hyperreflectivity seen (Figure 3).

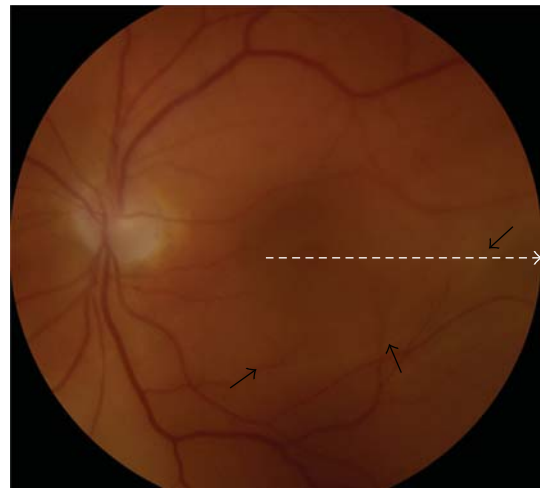

Figure 1: Colour fundus photograph of retinal detachment secondary to an inferior temporal retinal tear. Black arrows indicate the initially suspected margin of the retinal detachment. Dotted line depicts the direction of the OCT scan shown in Figure 2.

3. Case 2

Our next case was a fifty-year-old myopic female who presented on a Friday with a several-month history of floaters and visual distortion described as "looking through Vaseline." Visual acuity was reduced to 6/12. Biomicroscopic examination showed an inferior macula-off retinal detachment. Microstructural analysis of the macula was performed using a Heidelberg Spectralis OCT scan which confirmed a macula-off retinal detachment; however, the OCT scan revealed that the fovea was bisected by this detachment (Figure 4). Moreover, the macula microstructure seen in the OCT scan showed no retinal folds or hyperreflectivity present near the fovea. Indeed, the only morphological retinal detachment changes observed which indicated any chronicity were small intraretinal cysts present peripherally away from the fovea (Figure 4).

Given the OCT findings, she was treated as a macula-on retinal detachment patient, and surgery was expedited such that an emergency theatre session was organised within 24 hours on a Saturday morning. The surgical repair was a three-port pars plana vitrectomy using a sulphur hexaflouride tamponade and cryotherapy. After subsequent cataract surgery, vision had returned to 6/6 with normal OCT findings (scan not shown).

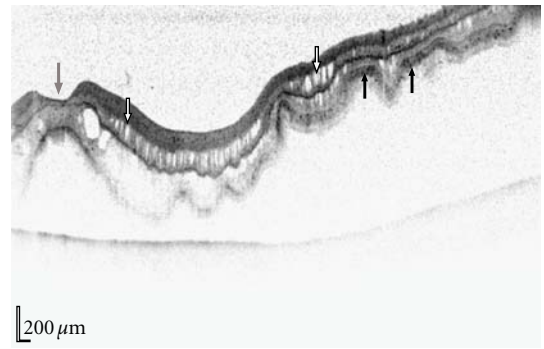

Figure 2: Horizontal spectralis OCT of the retinal detachment shown in Figure 1, scan direction is indicated by the white dotted line in Figure 1. Characteristic changes seen on OCT in retinal detachments are observed including retinal folds, intraretinal cysts (white arrows), and hyperreflectivity of the photoreceptor layer (black arrows). Fovea is denoted by a grey arrow.

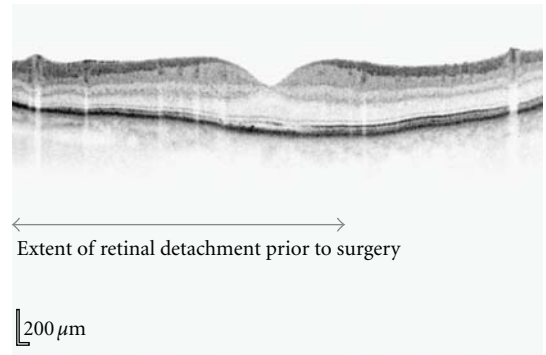

Figure 3: Postsurgical vertical OCT of the retinal detachment shown in Figures 1 and 2. The area of retinal detachment prior to surgery is represented by the bar below the OCT. Restoration of normal morphology has occurred one year following retinal detachment repair.

4. Discussion

The morphological changes seen in retinal detachment have previously been evaluated by OCT and are becoming clearer with newer systems using spectral domain calculations, which have improved data acquisition speeds to ~40 000 A-scans per second allowing much greater axial resolution to approximately 3.5 μm tissue resolution [2]. The transformations seen in retinal detachment include intraretinal cyst formation, intraretinal separation, and undulation of outer retinal layers [3, 4]. The disruption of the photoreceptor

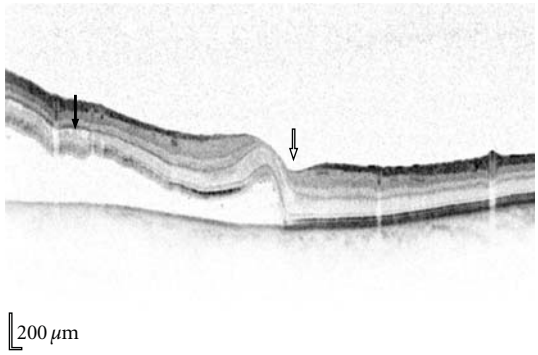

Figure 4: Acute retinal detachment that transects the fovea (white arrow), cystic changes are present peripherally (black arrow) but the fovea remains morphologically intact although shallowly detached from the pigmented epithelium.

inner and outer segment junction in macula-off rhegmatogenous retinal detachments is also seen both preoperatively [5] and postoperatively [6, 7]. Murine models comparing histology and OCT confirm these findings and also highlight the hyperreflectivity in the photoreceptor layer which may represent a cellular immune infiltration or misalignment of the photoreceptor layer [8]. These changes were all seen in our first case (Figure 2) proving that the retinal detachment had been present for a period of time prior to arrival in our unit and enabling appropriate de-prioritisation within a busy vitreoretinal service.

In our second case, in which the fovea was bisected by a retinal detachment, time of onset was in some doubt. Retinal thickness of the detached retina has been shown to be time dependent initially thickening then thinning with time [8, 9]; however the subfovea thickness was normal when scanned suggesting a recent event along with the absence of any intraretinal cysts, retinal undulations, and hyper reflectivity of the photoreceptor layer (Figure 4). Onset of retinal detachment is of importance, as experimental retinal detachments in cats have shown that although alterations in the outer nuclear layer occur after 1 hour, progressive loss of photoreceptors continues up to 13–30 days [10], with limited atrophy in cat retinas detached 3 to 7 days [11]. Macular involvement in retinal detachment has a bad prognosis for visual outcome [1]. However, patients that have no tomographic structural changes presumably due to recent foveal involvement have better clinical prognosis [4]. This is most likely secondary to less atrophy and death of the photoreceptors which has histopathologically been shown to be present in prolonged detachment of the retina [10–14]. Finally, the height of retinal detachment, which appears to affect the formation of multiple cystic cavities in the detached inner and outer neuronal layers, correlates with poor visual outcome [15, 16]. All of these features when taken into account suggested a good prognostic outcome for our second patient and hence prompt surgery resulting in an excellent visual recovery; an outcome that could have been considerably poorer if surgery had been delayed and fovea atrophy had occurred.

The ability to predict the outcome of operations obviously helps plan surgery. The morphological changes in retinal detachment seen in OCT scans give prognostic factors pertaining to visual outcome and thus help anticipate surgical outcomes. This paper has shown the two scenarios where surgical prioritisation is reversed, that is, from macula on to macula off and secondly, from macula off to macula on. In our first case, a chronic detachment was identified by OCT and allowed planning within the department for higher priority operations to take place. Conversely, the lack of subfoveal morphological changes in our second case led to the conclusion that the detachment was recent and prognosis good, thus surgery was expedited. Both cases highlight the superiority of OCT imaging against biomicroscopy. We suggest that if any doubt regarding the status of the macula exists, a routine noninvasive OCT should be performed to help clarify the situation prior to surgery.

References

[1] W. H. Ross, "Visual recovery after macula-off retinal detachment," *Eye*, vol. 16, no. 4, pp. 440–446, 2002.

[2] S. Alam, R. J. Zawadzki, S. Choi et al., "Clinical application of rapid serial fourier-domain optical coherence tomography for macular imaging," *Ophthalmology*, vol. 113, no. 8, pp. 1425–1431, 2006.

[3] N. Hagimura, K. Suto, T. Iida, and S. Kishi, "Optical coherence tomography of the neurosensory retina in rhegmatogenous retinal detachment," *American Journal of Ophthalmology*, vol. 129, no. 2, pp. 186–190, 2000.

[4] S. Y. Lee, S. G. Joe, J. G. Kim, H. Chung, and Y. H. Yoon, "Optical coherence tomography evaluation of detached macula from rhegmatogenous retinal detachment and central serous chorioretinopathy," *American Journal of Ophthalmology*, vol. 145, no. 6, pp. 1071–1076, 2008.

[5] H. Nakanishi, M. Hangai, N. Unoki et al., "Spectral-domain optical coherence tomography imaging of the detached macula in rhegmatogenous retinal detachment," *Retina*, vol. 29, no. 2, pp. 232–242, 2009.

[6] A. J. Smith, D. G. Telander, R. J. Zawadzki et al., "High-resolution fourier-domain optical coherence tomography and microperimetric findings after macula-off retinal detachment repair," *Ophthalmology*, vol. 115, no. 11, pp. 1923–1929, 2008.

[7] T. Wakabayashi, Y. Oshima, H. Fujimoto et al., "Foveal microstructure and visual acuity after retinal detachment repair. Imaging analysis by fourier-domain optical coherence tomography," *Ophthalmology*, vol. 116, no. 3, pp. 519–528, 2009.

[8] C. M. Cebulla, M. Ruggeri, T. G. Murray, W. J. Feuer, and E. Hernandez, "Spectral domain optical coherence tomography in a murine retinal detachment model," *Experimental Eye Research*, vol. 90, no. 4, pp. 521–527, 2010.

[9] H. Yetik, H. Guzel, and S. Ozkan, "Structural features of attached retina in rhegmatogenous retinal detachments," *Retina*, vol. 24, no. 1, pp. 63–68, 2004.

[10] C. C. Barr, "The histopathology of successful retinal reattachment," *Retina*, vol. 10, no. 3, pp. 189–194, 1990.

[11] D. H. Anderson, C. J. Guerin, and P. A. Erickson, "Morphological recovery in the reattached retina," *Investigative Ophthalmology and Visual Science*, vol. 27, no. 2, pp. 168–183, 1986.

[12] P. A. Erickson, S. K. Fisher, and D. H. Anderson, "Retinal detachment in the cat: the outer nuclear and outer plexiform layers," *Investigative Ophthalmology and Visual Science*, vol. 24, no. 7, pp. 927–942, 1983.

[13] D. J. Wilson and W. R. Green, "Histopathologic study of the effect of retinal detachment surgery on 49 eyes obtained post mortem," *American Journal of Ophthalmology*, vol. 103, no. 2, pp. 167–179, 1987.

[14] W. W. Lai, G. Y. O. Leung, C. W. S. Chan, I. Y. L. Yeung, and D. Wong, "Simultaneous spectral domain OCT and fundus autofluorescence imaging of the macula and microperimetric correspondence after successful repair of rhegmatogenous retinal detachment," *British Journal of Ophthalmology*, vol. 94, no. 3, pp. 311–318, 2010.

[15] A. Lecleire-Collet, M. Muraine, J. F. Ménard, and G. Brasseur, "Evaluation of macular changes before and after successful retinal detachment surgery using stratus-optical coherence tomography," *American Journal of Ophthalmology*, vol. 142, no. 1, pp. 176–179, 2006.

[16] L. S. Schocket, A. J. Witkin, J. G. Fujimoto et al., "Ultrahigh-resolution optical coherence tomography in patients with decreased visual acuity after retinal detachment repair," *Ophthalmology*, vol. 113, no. 4, pp. 666–672, 2006.

Hindawi Publishing Corporation
Journal of Ophthalmology
Volume 2011, Article ID 743670, 6 pages
doi:10.1155/2011/743670

Review Article

Simultaneous Confocal Scanning Laser Ophthalmoscopy Combined with High-Resolution Spectral-Domain Optical Coherence Tomography: A Review

Verônica Castro Lima,[1] Eduardo B. Rodrigues,[1] Renata P. Nunes,[1] Juliana F. Sallum,[1] Michel E. Farah,[1] and Carsten H. Meyer[2]

[1] *Retina Service, Department of Ophthalmology, Federal University of São Paulo, 04021-001 São Paulo, SP, Brazil*
[2] *Department of Ophthalmology, University of Bonn, 53012 Bonn, Germany*

Correspondence should be addressed to Verônica Castro Lima, vecastrolima@yahoo.com.br

Received 23 June 2011; Accepted 17 August 2011

Academic Editor: Fernando Penha

We aimed to evaluate technical aspects and the clinical relevance of a simultaneous confocal scanning laser ophthalmoscope and a high-speed, high-resolution, spectral-domain optical coherence tomography (SDOCT) device for retinal imaging. The principle of confocal scanning laser imaging provides a high resolution of retinal and choroidal vasculature with low light exposure. Enhanced contrast, details, and image sharpness are generated using confocality. The real-time SDOCT provides a new level of accuracy for assessment of the angiographic and morphological correlation. The combined system allows for simultaneous recordings of topographic and tomographic images with accurate correlation between them. Also it can provide simultaneous multimodal imaging of retinal pathologies, such as fluorescein and indocyanine green angiographies, infrared and blue reflectance (red-free) images, fundus autofluorescence images, and OCT scans (Spectralis HRA + OCT; Heidelberg Engineering, Heidelberg, Germany). The combination of various macular diagnostic tools can lead to a better understanding and improved knowledge of macular diseases.

1. Introduction

With the advent of novel technologies, both optical coherence tomography (OCT) and confocal scanning laser ophthalmoscopy (cSLO) have been introduced successfully into the routine clinical imaging for a wide spectrum of macular diseases. The combination of these two techniques in one instrument, which offers various subsequent advantages, including exact correlation of tomographic and topographic findings, has the potential to enhance further our understanding of disease pathogenesis, diagnosis, and patient management.

In this paper, we aimed to review the history, some of the technical aspects, and important clinical applications of a high-speed, high-resolution spectral-domain OCT (SDOCT) device which also is able to combine cSLO-based fluorescein and indocyanine green angiograms, infrared, blue reflectance ("red-free"), and fundus autofluorescence (FAF) images.

2. History

Based on the pioneering work of Webb et al. [1, 2], confocal scanning laser ophthalmoscopes (cSLOs) have been developed for clinical use. Although limited by the optical properties of the human eye, they are able to achieve high-contrast images of the posterior segment. Today most scanning laser systems record their images in real time with a fast frame rate.

Optical coherence tomography was initially reported by Huang and coworkers in 1991 [3] and has had a tremendous subsequent impact on *in vivo* imaging of retinal diseases. It has evolved as a noninvasive technique and allows for visualization of microstructural alterations of the retinal

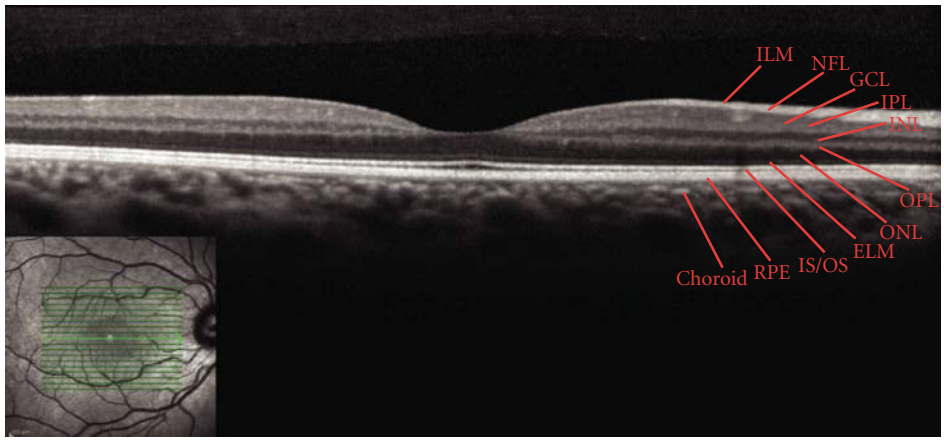

Figure 1: Example of a normal eye imaged with the *Spectralis* SDOCT. The infrared reflectance cSLO image (lower left) shows a normal fundus which corresponds to the normal SDOCT B-scan. The green lines represent the location, and the green arrow shows the exact orientation of the B-scan. All the retinal layers are indicated on the SDOCT scan (ILM: internal limiting membrane; NFL: nerve fiber layer; GCL: ganglion cell layer; IPL: inner plexiform layer; INL: inner nuclear layer; OPL: outer plexiform layer; ONL: outer nuclear layer; ELM: external limiting membrane; IS/OS: photoreceptor inner/outer segment junction; RPE: retinal pigment epithelium).

tomographic architecture. This imaging modality is now used widely by ophthalmologists for a range of indications and has become a standard diagnostic technique [4–16]. It provides images analogous to ultrasonography, but, instead of sound, it uses light waves to obtain a reflectivity profile of the tissue under investigation, measuring the time delay and magnitude of backscattered or reflected light by low-coherence interferometry.

The OCT technique available most widely in clinical practice is referred to as time-domain OCT, because the depth information of the retina is acquired as a sequence of samples over time. This can be performed either in longitudinal cross-sections perpendicular to or in the coronal plane parallel to the retinal surface. Recently, major advances have been made regarding the image resolution—notably the development of a high-resolution OCT—and in imaging speed, signal-to-noise ratio, and sensitivity with the introduction of an ultrahigh-resolution SDOCT [17–24]. In time-domain OCT and earlier ultrahigh-resolution OCT, reference mirrors move mechanically, limiting imaging speed. In SDOCT, the reference mirror is stationary and the OCT signal is acquired either by using a spectrometer as a detector or by varying the narrowband wavelength of the light source in time (swept source). Echo time delays of light are measured by acquiring the interference spectrum of the light signal and taking its Fourier transform [25, 26]. Increasing imaging speed allows for the acquisition of images within a fraction of second, thus minimizing motion artifacts [27]. It has also become possible to acquire three-dimensional volume OCT scans that achieve comprehensive retinal coverage [28].

The combination of OCT and cSLO in one instrument offers a number of subsequent advantages, including an accurate correlation of tomographic with topographic architecture of the retina, which opens new insights in the pathogenesis and morphological alterations of retinal diseases [29, 30]. Additionally a multimodality imaging system provides a complete view of the vitreous, retina and choroid, enabling clinicians to combine information from six different modes to assess the eye: fluorescein and indocyanine green angiographies, FAF, infra-red, red-free, and SD-OCT. Simultaneous high-resolution fundus imaging and SD-OCT with the *Spectralis* (Heidelberg Engineering, Heidelberg, Germany) offer high-quality images with the certainty of knowing the location, leading to a significantly better diagnosis and monitoring of the patient (Figure 1).

3. Technical Aspects

The imaging system cSLO/OCT (*Spectralis* HRA+OCT) combines high speed, high-resolution SDOCT images with simultaneous recording of fluorescein and indocyanine-green angiographies, digital infrared and blue reflectance, or FAF images. On the other hand, the *Spectralis* OCT has only two modes—SDOCT and infrared. Both SDOCT devices use a new proprietary eye-tracking technology, which locks onto a specific location on the retina and relocates the site at later exams to enhance the monitoring of disease progression and treatment decisions. For image clarity, the proprietary Heidelberg Noise Reduction feature takes the axial resolution from 7 microns to 3.5 microns. And the device dual-beam imaging captures a reference scan and cross-section simultaneously for reliably accurate registration.

Regarding the technical parameters of the SDOCT, 40 000 A-scans are acquired per second using an optical resolution of approximately 7 mm in depth (axial resolution) and 14 mm transversally (lateral optical resolution). The centre wavelength of the OCT light source is typically between 870 and 880 nm. OCT scans can be recorded simultaneously with fluorescein angiography, indocyanine-green angiography, FAF, infrared, and blue reflectance images. For the A-scans the scan depth is 1.8 mm/512 pixels, providing a digital axial resolution of 3.5 μm/pixel. *Spectralis* scans 100 times faster than time-domain OCT and 40% faster than most other

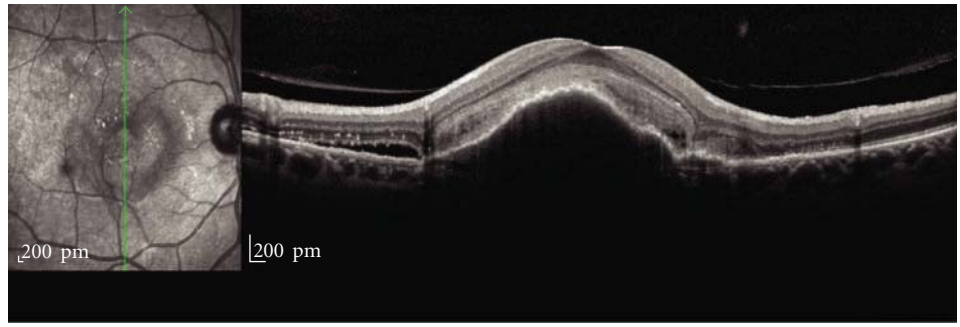

Figure 2: A 71-year-old man with a pigment epithelial detachment in the presence of neovascular AMD in the right eye. In the SDOCT scan the pigment epithelial detachment is readily visualized underneath the fovea associated with intraretinal cysts and subretinal fluid. It is also possible to identify the subretinal neovascular membrane and the vitreoretinal interface.

SDOCT instruments. B-scans cover a transversal range of 15, 20, or 30° field of view. In the high-speed mode scan widths are 384, 512, and 768 A-scans per B-scan with a lateral digital resolution of 11 μm/pixel and a scan rate of 89, 69 and 48 B-scans/second, respectively. In the high-speed mode, the vertical presentation of the OCT scan is magnified twice; therefore morphological alterations are presented disproportionately high in the vertical dimension. The accelerated imaging speed allows the acquisition of an image within a fraction of second, thus minimizing motion artefacts. Vertical and horizontal OCT scans are placed in the area of interest.

The high-resolution modes encompass a scan width of 768, 1024, and 1.536 A-scans per B-scan with a lateral digital resolution of 5 μm/pixel at a scan rate of 48, 37, and 25 B-scans/second, respectively. High-resolution fundus images provide clear cross-sectional scans of the retinal anatomical structure, including the retinal surface, intraretinal alterations, as well as subretinal morphologic pathologies.

Sequences of B-scans can be acquired to image a full volume. These volume scans can be obtained at 15, 20 and 30° field of view. The number of B-scans per volume can be adjusted from 12 to 96 B-scans per 10°. In addition, it is also possible to acquire 3D volumetric OCT scans for comprehensive analysis of the entire retina and, therefore, for 3D mapping of pathologic alterations within the retinal layers including the RPE.

4. Clinical Applications

The new technology of the SDOCT has improved the visualization of intraretinal morphologic features allowing the evaluation of the integrity of each retinal layer and *in vivo* visualization of microstructural morphology of the retina. The high-speed, high-resolution SDOCT (*Spectralis*) has been applied over the last few years to investigate morphological substrates for alterations in eyes with various macular disorders.

One of the most important clinical applications of this device is to help guiding diagnosis and treatment of patients with age-related macular degeneration (AMD). In early stages of AMD, drusen can be detected at their specific location [29]. Small drusen appears as localized detachments of the retinal pigment epithelium (RPE) with intact layered architecture of the photoreceptor segments. In large drusen, RPE elevation and derangement can be seen in association with a disrupted photoreceptor band. Additionally in cases of reticular drusen, another example of early AMD, the SDOCT scan shows alterations in the outer retinal and RPE layers. These ultrastructural characteristics may allow distinguishing subclasses of drusen and may allow identifying biomarkers for disease severity or risk of progression [31]. In cases of dry AMD with geographic atrophy, SDOCT scans also can confirm loss of the RPE monolayer along with atrophy of the outer neurosensory retinal layers. In most eyes with geographic atrophy the inner retinal layers are unchanged, whereas the outer retinal layers show alterations in all eyes. SDOCT provides adequate resolution for quantifying photoreceptor loss and allows visualization of reactive changes in the RPE cells in the junctional zone of geographic atrophy [30, 32, 33]. Finally SDOCT scans can be useful to delimitate and better visualize areas of pigment epithelium detachments (PEDs) and choroidal neovascular membranes in cases of wet or exudative AMD (Figure 2). The combination of the FA and the SDOCT with high-resolution and real-time mean image elaboration may enhance the detailed visualization of activity in new choroidal neovascularization, such as presence of subretinal, intraretinal, or sub-RPE fluid, intraretinal cysts, or a combination of them [34, 35]. The high sensitivity on neovascular activity expressed by the SDOCT features may be helpful in clinical practice, reducing the need of angiographies for treatment decisions [36].

It is well known that OCT imaging in patients with diabetic macular edema is able to reveal several structural changes in the retina, such as epiretinal membranes, intraretinal and subretinal fluid, and cystoid macular edema [37, 38]. It is a very useful tool for diagnosis, especially in challenging cases, and treatment followup. Only a limited number of studies using different SDOCT devices for assessing diabetic macular edema and diabetic retinopathy have been published [39–42]. In cases of diabetic macular edema, SDOCT has enabled us to analyze with more details the integrity of the outer retinal layers, which includes the external limiting membrane, the photoreceptors junction, the RPE, and Bruch's membrane. One first report using the *Spectralis* SDOCT showed the importance of the integrity

of the external limiting membrane and the photoreceptors junction as a prognostic feature of visual improvement after treatment for diabetic macular edema [42].

Spectral-domain OCT has dramatically improved the visualization of the vitreomacular interface and posterior hyaloid membrane and has become a very important tool for the diagnosis and followup of patients with alterations of the vitreoretinal interface. In cases of epiretinal membranes and macular pucker, vitreoretinal adhesions at the peak elevation and retinal wrinkling can be seen in the cSLO image. In the correspondent SDOCT cross-sectional image the wrinkling of the inner retinal surface and thickening of the neurosensory retina, particularly pronounced in the outer nuclear layer and the innermost neurosensory layers, can be observed [29]. Also, in cases of macular hole, besides other features that have been well described, SDOCT can demonstrate disruption of photoreceptors junction and imaging this structure is a method of assessing structural integrity of the photoreceptors before and after macular hole surgery [43].

The *Spectralis* SDOCT is a very useful tool for other macular pathologies, such as retinal vascular occlusive diseases with macular involvement, central serous chorioretinopathy, macular dystrophies, idiopathic perifoveal telangiectasia, and chloroquine retinopathy. There are few studies published in the literature showing its clinical applications. Important advantages with clinical significance of this new technology compared to the time-domain technology are the ability to better visualize the vitreoretinal interface and outer retinal layers, especially the photoreceptors junction, and the possibility to obtain 3-dimensional scans allowing to image structural changes of the vitreoretinal interface and the retina in large areas.

One advantage of the *Spectralis* OCT is the improved visualization of the choroid. Margolis and Spaide [44] described the measurement of the choroidal thickness using the enhanced depth imaging technique. It is described by positioning the device close enough to the eye to acquire an inverted image within a 5×30-degree area centered at the fovea and then performing manual measurements from the outer border of the RPE to the inner scleral border. In the normal studied eyes, the subfoveal choroid was thickest and grew thinner at more peripheral measurement points. Also choroidal thickness demonstrated a negative correlation with age. In different reports using the same technique, the author reported enhanced depth imaging of choroidal changes underneath a pigmented epithelial detachment in patients with exudative AMD, thus describing a novel disease entity termed age-related chorioretinal atrophy [45, 46]. The ability to visualize and quantify choroidal thickness is a very interesting area of research and may be limited to a few SDOCT devices which can overcome the technical limitations of imaging deeper structures such as analog-to-digital conversion, wavelength-dependent light scattering, and signal loss in the image path before Fourier transformation.

In conclusion, the combined cSLO/OCT system allows simultaneous recording and interpolation of topographic and tomographic images. Different cSLO imaging modes including infrared and blue reflectance, FAF and fluorescein or ICG angiography can be combined with simultaneous acquisition of OCT. This multimodality combination allows for a better understanding of the pathogenesis of several macular pathologies and improvement of diagnosis and management of patients with macular diseases.

Conflict of Interests

The authors have no financial interest in any equipment or technique described in the paper.

References

[1] R. H. Webb, G. W. Hughes, and O. Pomerantzeff, "Flying spot TV ophthalmoscope," *Applied Optics*, vol. 19, no. 17, pp. 2991–2997, 1980.

[2] R. H. Webb, G. W. Hughes, and F. C. Delori, "Confocal scanning laser ophthalmoscope," *Applied Optics*, vol. 26, no. 8, pp. 1492–1499, 1987.

[3] D. Huang, E. A. Swanson, C. P. Lin et al., "Optical coherence tomography," *Science*, vol. 254, no. 5035, pp. 1178–1181, 1991.

[4] M. R. Hee, J. A. Izatt, E. A. Swanson et al., "Optical coherence tomography of the human retina," *Archives of Ophthalmology*, vol. 113, no. 3, pp. 325–332, 1995.

[5] M. R. Hee, C. R. Baumal, C. A. Puliafito et al., "Optical coherence tomography of age-related macular degeneration and choroidal neovascularization," *Ophthalmology*, vol. 103, no. 8, pp. 1260–1270, 1996.

[6] C. A. Puliafito, M. R. Hee, C. P. Lin et al., "Imaging of macular diseases with optical coherence tomography," *Ophthalmology*, vol. 102, no. 2, pp. 217–229, 1995.

[7] J. S. Schuman, M. R. Hee, A. V. Arya et al., "Optical coherence tomography: a new tool for glaucoma diagnosis," *Current Opinion in Ophthalmology*, vol. 6, no. 2, pp. 89–95, 1995.

[8] J. S. Schuman, M. R. Hee, C. A. Puliafito et al., "Quantification of nerve fiber layer thickness in normal and glaucomatous eyes using optical coherence tomography: a pilot study," *Archives of Ophthalmology*, vol. 113, no. 5, pp. 586–596, 1995.

[9] A. Gaudric, B. Haouchine, P. Massin, M. Paques, P. Blain, and A. Erginay, "Macular hole formation: new data provided by optical coherence tomography," *Archives of Ophthalmology*, vol. 117, no. 6, pp. 744–751, 1999.

[10] D. S. Chauhan, R. J. Antcliff, P. A. Rai, T. H. Williamson, and J. Marshall, "Papillofoveal traction in macular hole formation: the role of optical coherence tomography," *Archives of Ophthalmology*, vol. 118, no. 1, pp. 32–38, 2000.

[11] P. Massin, C. Allouch, B. Haouchine et al., "Optical coherence tomography of idiopathic macular epiretinal membranes before and after surgery," *American Journal of Ophthalmology*, vol. 130, no. 6, pp. 732–739, 2000.

[12] P. Massin, B. Haouchine, A. Gaudric et al., "Macular traction detachment and diabetic edema associated with posterior hyaloidal traction ," *American Journal of Ophthalmology*, vol. 132, no. 4, pp. 599–600, 2001.

[13] P. Massin, A. Girach, A. Erginay, and A. Gaudric, "Optical coherence tomography: a key to the future management of patients with diabetic macular oedema," *Acta Ophthalmologica Scandinavica*, vol. 84, no. 4, pp. 466–474, 2006.

[14] H. Sánchez-Tocino, A. Alvarez-Vidal, M. J. Maldonado, J. Moreno-Montañés, and A. García-Layana, "Retinal thickness study with optical coherence tomography in patients with

diabetes," *Investigative Ophthalmology and Visual Science*, vol. 43, no. 5, pp. 1588–1594, 2002.

[15] R. F. Spaide, D. Wong, Y. Fisher, and M. Goldbaum, "Correlation of vitreous attachment and foveal deformation in early macular hole states," *American Journal of Ophthalmology*, vol. 133, no. 2, pp. 226–229, 2002.

[16] W. Soliman, B. Sander, and T. M. Jørgensen, "Enhanced optical coherence patterns of diabetic macular oedema and their correlation with the pathophysiology," *Acta Ophthalmologica Scandinavica*, vol. 85, no. 6, pp. 613–617, 2007.

[17] W. Drexler, U. Morgner, F. X. Kärtner et al., "In vivo ultrahigh-resolution optical coherence tomography," *Optics Letters*, vol. 24, no. 17, pp. 1221–1223, 1999.

[18] W. Drexler, U. Morgner, R. K. Ghanta, F. X. Kärtner, J. S. Schuman, and J. G. Fujimoto, "Ultrahigh-resolution ophthalmic optical coherence tomography," *Nature Medicine*, vol. 7, no. 4, pp. 502–506, 2001.

[19] W. Drexler, H. Sattmann, B. Hermann et al., "Enhanced visualization of macular pathology with the use of ultrahigh-resolution optical coherence tomography," *Archives of Ophthalmology*, vol. 121, no. 5, pp. 695–706, 2003.

[20] W. Drexler, U. Morgner, R. K. Ghanta et al., "New technology for ultrahigh resolution optical coherence tomography of the retina," in *The Shape of Glaucoma*, H. Lemij and J. S. Schuman, Eds., pp. 75–104, Kugler, Berlin, Germany, 2005.

[21] B. Cense, N. A. Nassif, T. C. Chen et al., "Ultrahigh-resolution high-speed retinal imaging using spectral-domain optical coherence tomography," *Optics Express*, vol. 12, no. 11, pp. 2435–2447, 2004.

[22] W. Drexler, "Ultrahigh-resolution optical coherence tomography," *Journal of Biomedical Optics*, vol. 9, no. 1, pp. 47–74, 2004.

[23] R. A. Leitgeb, W. Drexler, A. Unterhuber et al., "Ultrahigh resolution fourier domain optical coherence tomography," *Optics Express*, vol. 12, no. 10, pp. 2156–2165, 2004.

[24] M. Wojtkowski, T. Bajraszewski, I. Gorczynska et al., "Ophthalmic imaging by spectral optical coherence tomography," *American Journal of Ophthalmology*, vol. 138, no. 3, pp. 412–419, 2004.

[25] A. F. Fercher, C. K. Hitzenberger, G. Kamp, and S. Y. El-Zaiat, "Measurement of intraocular distances by backscattering spectral interferometry," *Optics Communications*, vol. 117, no. 1-2, pp. 43–48, 1995.

[26] G. Hausler and M. W. Lindner, "'Coherence radar' and "spectral radar"—new tools for dermatological diagnosis," *Journal of Biomedical Optics*, vol. 3, no. 1, pp. 21–31, 1998.

[27] E. A. Swanson, J. A. Izatt, M. R. Hee et al., "In vivo retinal imaging by optical coherence tomography," *Optics Letters*, vol. 18, no. 21, pp. 1864–1869, 1993.

[28] M. Wojtkowski, V. Srinivasan, J. G. Fujimoto et al., "Three-dimensional retinal imaging with high-speed ultrahigh-resolution optical coherence tomography," *Ophthalmology*, vol. 112, no. 10, pp. 1734–1746, 2005.

[29] H. M. Helb, P. C. Issa, M. Fleckenstein et al., "Clinical evaluation of simultaneous confocal scanning laser ophthalmoscopy imaging combined with high-resolution, spectral-domain optical coherence tomography," *Acta Ophthalmologica*, vol. 88, no. 8, pp. 842–849, 2010.

[30] U. E. Wolf-Schnurrbusch, V. Enzmann, C. K. Brinkmann, and S. Wolf, "Morphologic changes in patients with geographic atrophy assessed with a novel spectral OCT-SLO combination," *Investigative Ophthalmology and Visual Science*, vol. 49, no. 7, pp. 3095–3099, 2008.

[31] A. A. Khanifar, A. F. Koreishi, J. A. Izatt, and C. A. Toth, "Drusen ultrastructure imaging with spectral domain optical coherence tomography in age-related macular degeneration," *Ophthalmology*, vol. 115, no. 11, pp. 1883–1890, 2008.

[32] S. Bearelly, F. Y. Chau, A. Koreishi, S. S. Stinnett, J. A. Izatt, and C. A. Toth, "Spectral domain optical coherence tomography imaging of geographic atrophy margins," *Ophthalmology*, vol. 116, no. 9, pp. 1762–1769, 2009.

[33] M. Brar, I. Kozak, L. Cheng et al., "Correlation between spectral-domain optical coherence tomography and fundus autofluorescence at the margins of geographic atrophy," *American Journal of Ophthalmology*, vol. 148, no. 3, pp. 439–444, 2009.

[34] A. Hassenstein and C. H. Meyer, "Clinical use and research applications of Heidelberg retinal angiography and spectral-domain optical coherence tomography—a review," *Clinical and Experimental Ophthalmology*, vol. 37, no. 1, pp. 130–143, 2009.

[35] C. Cukras, Y. D. Wang, C. B. Meyerle, F. Forooghian, E. Y. Chew, and W. T. Wong, "Optical coherence tomography-based decision making in exudative age-related macular degeneration: comparison of time- vs spectral-domain devices," *Eye*, vol. 24, no. 5, pp. 775–783, 2010.

[36] A. Giani, D. D. Esmaili, C. Luiselli et al., "Displayed reflectivity of choroidal neovascular membranes by optical coherence tomography correlates with presence of leakage by fluorescein angiography," *Retina*, vol. 31, no. 5, pp. 942–948, 2011.

[37] S. Yamamoto, T. Yamamoto, M. Hayashi, and S. Takeuchi, "Morphological and functional analyses of diabetic macular edema by optical coherence tomography and multifocal electroretinograms," *Graefe's Archive for Clinical and Experimental Ophthalmology*, vol. 239, no. 2, pp. 96–101, 2001.

[38] T. Otani, S. Kishi, and Y. Maruyama, "Patterns of diabetic macular edema with optical coherence tomography," *American Journal of Ophthalmology*, vol. 127, no. 6, pp. 688–693, 1999.

[39] L. Yeung, V. C. Lima, P. Garcia, G. Landa, and R. B. Rosen, "Correlation between spectral domain optical coherence tomography findings and fluorescein angiography patterns in diabetic macular edema," *Ophthalmology*, vol. 116, no. 6, pp. 1158–1167, 2009.

[40] D. Koleva-Georgieva and N. Sivkova, "Assessment of serous macular detachment in eyes with diabetic macular edema by use of spectral-domain optical coherence tomography," *Graefe's Archive for Clinical and Experimental Ophthalmology*, vol. 247, no. 11, pp. 1461–1469, 2009.

[41] F. Forooghian, C. Cukras, C. B. Meyerle, E. Y. Chew, and W. T. Wong, "Evaluation of time domain and spectral domain optical coherence tomography in the measurement of diabetic macular edema," *Investigative Ophthalmology and Visual Science*, vol. 49, no. 10, pp. 4290–4296, 2008.

[42] W. Einbock, L. Berger, U. Wolf-Schnurrbusch, J. Fleischhauer, and S. Wolf, "Predictive factors for visual acuity of patients with diabetic macular edema interpreted form the spectralis HRA+OCT (Heidelberg Engineering)," *Investigative Ophthalmology & Visual Science*, vol. 49, Article ID 3473, 2008.

[43] L. K. Chang, H. Koizumi, and R. F. Spaide, "Disruption of the photoreceptor inner segment-outer segment junction in eyes with macular holes," *Retina*, vol. 28, no. 7, pp. 969–975, 2008.

[44] R. Margolis and R. F. Spaide, "A pilot study of enhanced depth imaging optical coherence tomography of the choroid in normal eyes," *American Journal of Ophthalmology*, vol. 147, no. 5, pp. 811–815, 2009.

[45] R. F. Spaide, "Enhanced depth imaging optical coherence tomography of retinal pigment epithelial detachment in age-related macular degeneration," *American Journal of Ophthalmology*, vol. 147, no. 4, pp. 644–652, 2009.

[46] R. F. Spaide, "Age-related choroidal atrophy," *American Journal of Ophthalmology*, vol. 147, no. 5, pp. 801–810, 2009.

Hindawi Publishing Corporation
Journal of Ophthalmology
Volume 2011, Article ID 764183, 6 pages
doi:10.1155/2011/764183

Case Report

High-Resolution Optical Coherence Tomography Retinal Imaging: A Case Series Illustrating Potential and Limitations

Olena Puzyeyeva,[1] Wai Ching Lam,[1] John G. Flanagan,[1,2] Michael H. Brent,[1] Robert G. Devenyi,[1] Mark S. Mandelcorn,[1] Tien Wong,[1] and Christopher Hudson[1,2]

[1] *Retina Research Group, Department of Ophthalmology and Vision Sciences, University of Toronto, Toronto, ON, Canada M5T 2S8*
[2] *School of Optometry, University of Waterloo, Waterloo, ON, Canada N2L 3G1*

Correspondence should be addressed to Christopher Hudson, chudson@uwaterloo.ca

Received 15 February 2011; Accepted 24 June 2011

Academic Editor: Eduardo Buchele Rodrigues

Purpose. To present a series of retinal disease cases that were imaged by spectral domain optical coherence tomography (SD-OCT) in order to illustrate the potential and limitations of this new imaging modality. *Methods*. The series comprised four selected cases (one case each) of age-related macular degeneration (ARMD), diabetic retinopathy (DR), central retinal artery occlusion (CRAO), and branch retinal vein occlusion (BRVO). Patients were imaged using the Heidelberg Spectralis (Heidelberg Engineering, Germany) in SD-OCT mode. Patients also underwent digital fundus photography and clinical assessment. *Results*. SD-OCT imaging of a case of age-related macular degeneration revealed a subfoveal choroidal neovascular membrane with detachment of the retinal pigment epithelium (RPE) and neurosensory retina. Using SD-OCT, the cases of DR and BRVO both exhibited macular edema with cystoid spaces visible in the outer retina. *Conclusions*. The ability of SD-OCT to clearly and objectively elucidate subtle morphological changes within the retinal layers provides information that can be used to formulate diagnoses with greater confidence.

1. Introduction

Over the past decade, the development of high-speed, wide-bandwidth tuneable light sources in conjunction with high-speed photodetectors has resulted in major gains in the horizontal and depth resolution of optical coherence tomography (OCT) based instrumentation, thereby dramatically improving visualization capabilities during retinal and optic nerve examination [1, 2]. As a result, OCT has found its place as a widely accepted imaging technique, especially in ophthalmology.

The principle of OCT is based on interferometry [3, 4]. In a typical early generation OCT system, visible light (i.e., to visualise the beam) and broadband, short-coherence length, near-IR light are coupled into one branch of a Michelson interferometer. The light is then split into two paths, one leading to a reference mirror and the second is focused onto the retina. Light is reflected and backscattered from refractive index interfaces within the retina according to the optical properties of each interface. The reflected light from the retina (i.e., the sample arm) and from the reference mirror is recoupled into the interferometer, to ultimately be detected after interference in the spectrometer. Using "time domain" OCT, reflection sites at various depths in the tissue can be sampled by changing the path length of the reference arm. However, this mechanism limits the acquisition speed (approx. 400 A-scans/s), is prone to motion artifacts because of the slow scan speed, and makes real-time imaging impossible. The reference-arm mirror is also scanned at a constant velocity, allowing depth scans to be made pixel by pixel across the retina.

SD-OCT has dramatically improved image resolution. Using SD-OCT, broadband interference is measured with spectrally distinct detectors using Fourier analysis (i.e., light signal frequency is modulated as a function of depth), thereby avoiding path length adjustment of the reference arm. The avoidance of depth scanning results in dramatic gains in imaging speed (i.e., 20,000 to 40,000 A-scans/s) and

improved signal-to-noise ratio [5], with an axial resolution of approximately 7 μm, thereby permitting the acquisition of high-resolution, histological detail of the retina captured from the living human eye over a wide field of view. The much improved scan speed of SD-OCT also permits 3D scanning, with minimal impact of eye movements. The SD-OCT scans can also be referenced to simultaneously acquired 2D en-face images, thereby ensuring the accurate spatial location of each OCT A-scan within the 3D image. An example of SD-OCT imaging of a healthy retina is shown in Figure 1.

In this study, we report on the clinical application of SD-OCT using a series of case reports of patients with clinically defined common and/or classic eye diseases in order to highlight some of the potential, the limitations, and the clinical utility of this technology.

2. Methods

Patients were imaged using the Heidelberg Spectralis HRA + OCT (Heidelberg Engineering, Heidelberg, Germany) in SD-OCT mode, using a scan field of 30 degrees horizontally and 15 degrees vertically and 19 to 25 OCT horizontal sections (one section at least every 240 μm). Patients also underwent pupil dilation, digital fundus photography, and clinical assessment. Digital fundus photography was undertaken using a Canon digital fundus camera (Canon CR-DGi, Canon Inc., Japan) with a resolution of 12.8 mega pixels. Clinical assessment comprised visual acuity, stereo fundus biomicroscopy, and binocular indirect ophthalmoscopy, as appropriate.

2.1. The Heidelberg Spectralis HRA and OCT. The Heidelberg Spectralis HRA and OCT (Heidelberg Engineering, Heidelberg, Germany; Software version-1.6.1.0) can be used in any one of six imaging modes, that is, SD-OCT, fluorescein angiography, indocyanine green angiography, autofluorescence, and red-free and infrared imaging. This paper details use of the instrument in SD-OCT mode only. The Heidelberg Spectralis utilizes a broadband light source centered at 870 nm (i.e., no visible light "beacon") to simultaneously measure multiple wavelengths, a prerequisite of SD-OCT imaging (Heidelberg Retina Angiograph 2 Operating Instructions). Simultaneous confocal scanning laser ophthalmoscopy is used to generate high-resolution images of the retinal surface, thereby providing precise location information of each A-scan within a cross-sectional SD-OCT image. SD-OCT scanning generates 40,000 A-scans/second with an axial resolution of 3.5 microns/pixel digital (7 microns optical) and a transverse resolution of 14 microns [6]. Alignment software continuously tracks any eye movement during image acquisition and then adjusts the position of the A-scan on the retinal surface to ensure accurate registration of cross-sectional OCT images. Using eye tracking and registration technology, multiple images are obtained from a precise location to then be averaged and filtered to remove random noise from the final image. The same eye tracking/registration technology is used to ensure that the instrument automatically rescans images that are influenced by blink artifacts. Similarly, follow-up images are derived from the same area of retina, thereby eliminating subjective placement of the scan by the operator.

3. Case Reports

This series comprised four selected cases (one case each) of age-related macular degeneration (ARMD), diabetic retinopathy (DR), central retinal artery occlusion (CRAO), and branch retinal vein occlusion (BRVO).

3.1. Case 1: Exudative Age-Related Macular Degeneration (ARMD) (Figure 2). A 81-year-old female patient had a 20-year history of hypertension and a one-year history of type 2 diabetes. At first presentation, her best corrected visual acuity (VA) in the right (OD) and left (OS) eyes was 20/50 and 20/70, respectively. Intraocular pressures (IOPs) were 18 mmHg OD and 20 mmHg OS. Retinal examination revealed a large choroidal neovascular membrane (CNVM) and a probable serous pigment epithelium detachment (PED) OD and soft macular drusen OS (not shown).

3.2. Case 2: Treated Proliferative Diabetic Retinopathy with Clinically Significant Diabetic Macular Edema (Figure 3). A 51-year-old male patient presented with a 15 year history of type 2 diabetes, having taken oral medications for the first 11 years and having used insulin for the past 4 years. Past ocular history included laser photocoagulation in both eyes. At the initial visit, the best corrected visual acuity was 20/30 (OD) and 20/70 (OS) with IOPs of 20 mmHg OD and OS.

3.3. Case 3: Central Retinal Artery Occlusion (Figure 4). A 69-year-old male patient had a medical history of stroke and type 2 diabetes for fifteen years. He presented in the clinic with sudden and absolute vision loss OD. Visual acuity was Counting Fingers at 0.3 meters OD and 20/40 OS.

3.4. Case 4: Branch Retinal Vein Occlusion (Figure 5). A 78-year-old male patient had a 10 year history of hypertension. His past ocular history included cataract surgery to both eyes. The patient complained of blurry vision OS for the past 4 months. At the initial visit, the visual acuity was Counting Fingers at 0.07 meters OD and 20/200 OS with an intraocular pressure of 24 mmHg and 18 mmHg.

4. Discussion

SD-OCT imaging technology was used to acquire images of patients with various retinal diseases in order to evaluate the clinical utility, potential, and limitations of the technique. Both SD-OCT and conventional clinical techniques showed choroidal neovascular membrane and pigment epithelial detachment (case of ARMD); neovascularisation at the disc and elsewhere, fibrosis, epiretinal membrane, and laser scars (case of DR); retinal edema and haemorrhages (case of

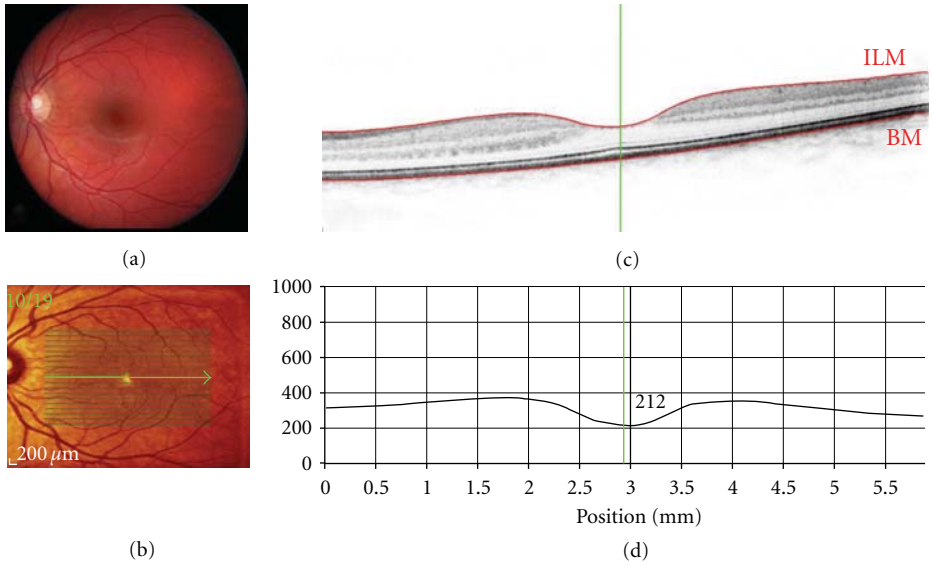

Figure 1: Spectral-domain (SD-OCT) optical coherence tomography of a healthy retina (OS): Scan parameters: infrared scan angle 30°; OCT scan angle 20°; pattern size 20°×15°, 19 sections (244 μm between B-scans). (a) Conventional fundus camera image. (b) SD-OCT en-face image showing overlaid OCT scan lines (green) and scan area. The green arrow shows the position of the scan line used to generate the cross-sectional retinal OCT image (i.e., (c)). (c) Cross-sectional image of the retina depicts the vitreous cavity (upper, optically clear area), the internal limiting membrane (segmented by the upper red line marked ILM, the intervening retinal layers, Bruch's membrane which is segmented by the lower red line marked BM, and the underlying choroid (lower). The vertical green line defines the position of the retinal thickness measure along the cross-sectional retinal thickness profile. (d) Cross-sectional retinal thickness profile corrected for tilt.

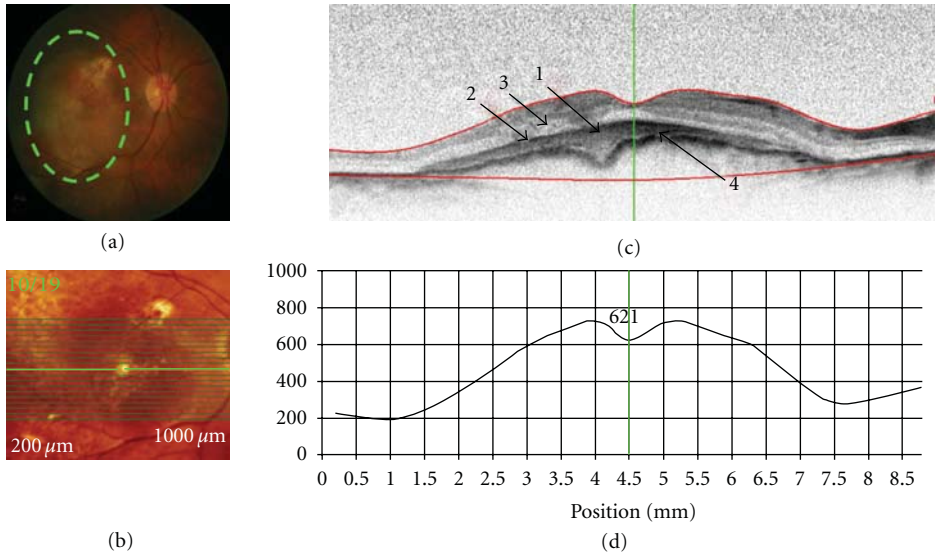

Figure 2: SD-OCT retinal scan of a patient with exudative age-related macular degeneration (OD). Scan parameters: infrared scan angle 30°; OCT scan angle 30°; pattern size 30°×15°, 19 sections (244 μm between B-scans). (a) The conventional fundus camera image showed a large choroidal neovascular membrane (CNVM) situated beneath the macula with a probable serous pigment epithelium detachment (PED). (b) SD-OCT en-face image centered on the fovea. The green highlighted line shows the position of the scan line used to generate the cross-sectional retinal OCT image (i.e., (c)). (c) The cross-sectional retinal image revealed a subfoveal CNVM (arrow "1") with a pigment epithelial detachment (PED) (arrow "2") and possible neurosensory retinal detachment (arrow "3") with apparent thickening and wrinkling of the Bruch's membrane/RPE complex. (d) Cross-sectional retinal thickness profile revealed increased thickness of the retina due to the CNVM. The lower red segment line (shown in (c)) fails to fit the true position of Bruch's membrane (arrow "4") in the area of the CNVM.

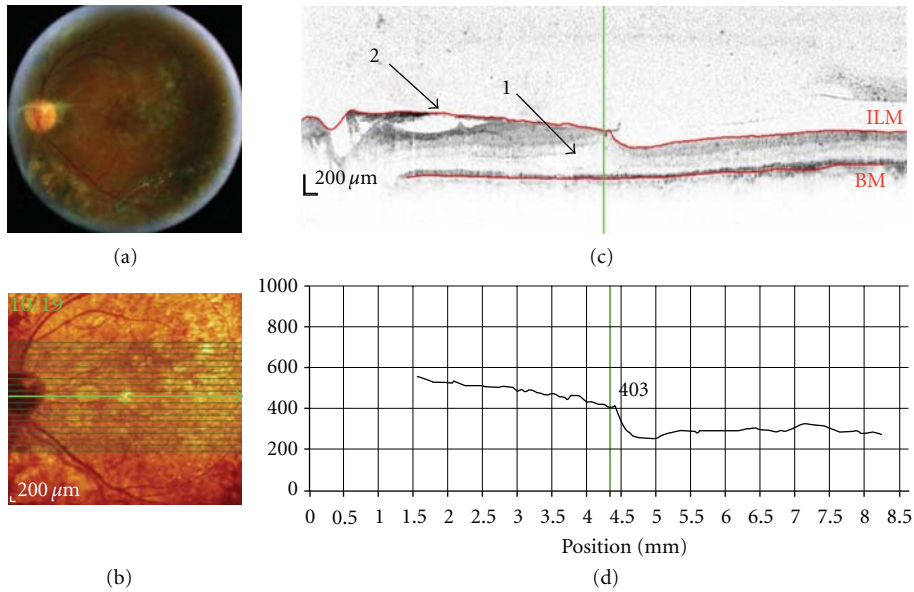

Figure 3: SD-OCT of a patient with proliferative diabetic retinopathy and clinically significant diabetic macular edema (DME) (OS). Scan parameters: infrared scan angle 30°; OCT scan angle 30°; pattern size 30°×15°, 19 sections (240 μm between B-scans). (a) The conventional fundus camera image showed clinically significant DME, fibrous tissue/epiretinal membrane temporal to the optic nerve head (ONH) extending towards the fovea and inferior to the fovea, neovascularisation at the ONH and also at the inferior macula and laser scars in the macula area and outside of the major retinal arcades. (b) SD-OCT en-face image centered on the fovea. The green arrow shows the position of the scan line used to generate the cross-sectional retinal OCT image (i.e., (c)). (c) The cross-sectional retinal image revealed cystoid spaces temporal to the ONH and extending close to the fovea in the outer retina (arrow "1"). The fibrous tissue/epiretinalmembrane can also be seen, located between the ONH and fovea (arrow "2"). (d) The cross-sectional retinal thickness profile revealed increased retinal thickness especially nasally to the fovea.

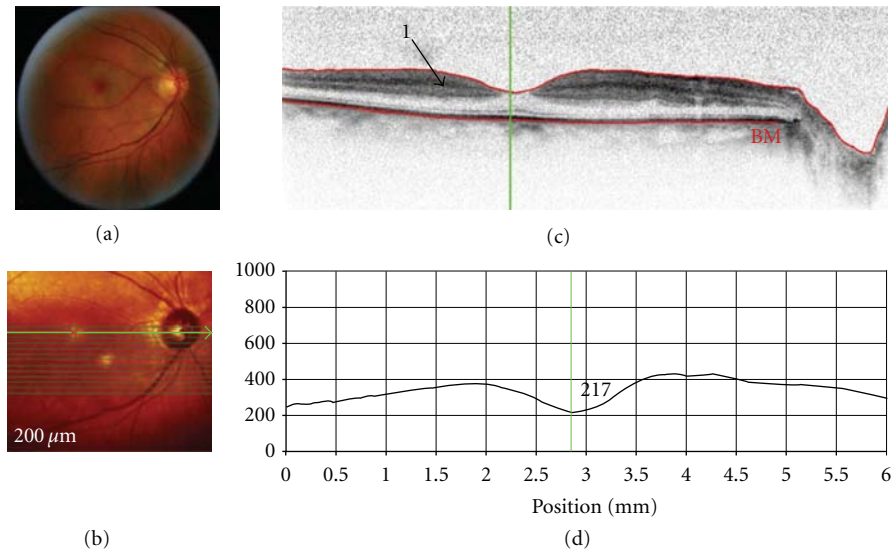

Figure 4: SD-OCT of a patient with central retinal artery occlusion (OD). Scan parameters: infrared scan angle 30°; OCT scan angle 30°; pattern size 30°×10°, 13 sections (243 μm between B-scans). (a) The conventional fundus camera image revealed a classic "cherry red spot" and white infarctions (ischemic areas) along the major vessel arcades and around the macula. (b) SD-OCT en-face image centered approximately 2° below the fovea. The green arrow shows the position of the scan line used to generate the cross-sectional retinal OCT image (i.e., (c)). (c) The cross-sectional retinal image showed a thickening and increased reflectance (arrow "1") of the inner retinal layers. (d) The cross-sectional retinal thickness profile revealed increased retinal thickness that was especially apparent as an exaggerated foveal pit (indicating swelling of the parafoveal retina).

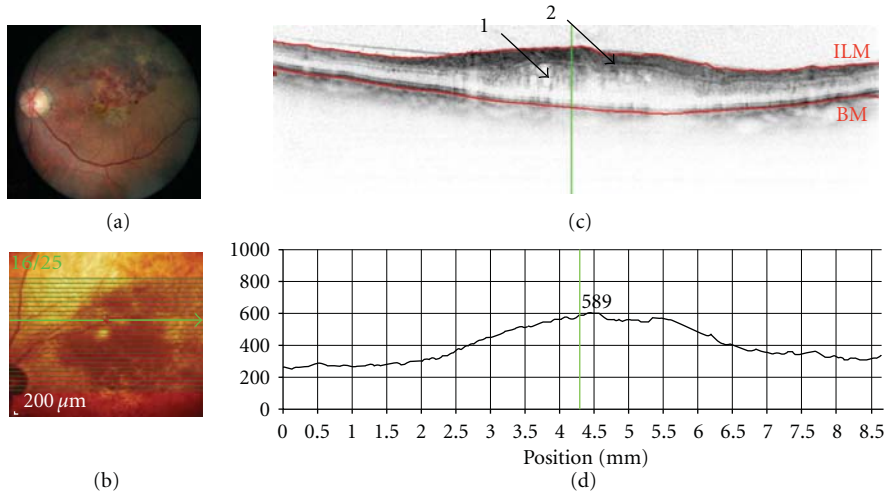

Figure 5: SD-OCT of a patient with branch retinal vein occlusion (OS). Scan parameters: infrared scan angle 30°; OCT scan angle 30°; pattern size 30°×20°, 25 sections (243 μm between B-scans). (a) The conventional fundus camera imaging revealed numerous hemorrhages and edema in the superior temporal retina with macular involvement. The macula was yellow and edematous. (b) SD-OCT en-face image of the fundus (note that the cross-sectional image is located approximately 5° superior to the superior ONH margin). The green arrow shows the position of the scan line used to generate the cross-sectional retinal OCT image (i.e., (c)). (c) The cross-sectional retinal image showed retinal edema with fluid cysts in the outer retina (arrow "1") and an *apparently* thickened inner retina with superficial hemorrhages (arrow "2") which "shadow" the underlying retinal details. (d) The lower red segment line (shown in (c)) fails to fit the true position of Bruch's membrane; the line was positioned based on visible parts of Bruch's membrane. The cross-sectional retinal thickness profile revealed a markedly thickened retina in the center of the BRVO (retinal thickness is close to 600 μm).

BRVO). In some circumstances, SD-OCT provided visualization of morphological changes associated with retinal diseases that were either not immediately visible or not at all visible, using conventional clinical techniques. For example, SD-OCT revealed neurosensory retinal detachment and Bruch's/retinal pigment epithelium wrinkling (case of ARMD); cystoid spaces localised in the outer retina (case of DR); thickening and increased reflectance of inner retina (case of CRAO); localisation of depth of macular edema and of haemorrhages (case of BRVO). Thus, SD-OCT revealed structural retinal changes that are not visible by 2-dimensional limited fundus photography. Conversely, the presence of colour information within the digital fundus photography images may be advantageous, while SD-OCT uses a narrow spectrum of wavelengths and therefore has limited colour information. For example, in the case of the CRAO, conventional digital fundus photography showed the presence of infarction more prominently than the cSLO and SD-OCT imaging.

Previous studies have shown that SD-OCT reveals retinal pathology that was not visible using TD-OCT, such as intra-retinal cysts and subretinal fluid [7]. SD-OCT also adds information to complete the clinical picture providing more detailed resolution of retinal changes, such as full-thickness folds of the RPE and intraretinal edema in case of RPE detachment, BRVO, toxoplasma chorioretinitis, and polypoidal choroidal vasculopathy [8]. A feature of the Heidelberg Spectralis instrument is the ability to undertake multiple mode imaging in addition to SD-OCT, including fluorescein angiography, indocyanine green angiography and autofluorescence, and red-free and infrared imaging. These additional imaging modes also provide further information about retinal pathology that can aid diagnosis and management. A description of these imaging modes is provided elsewhere [9, 10].

The ability of SD-OCT to clearly and objectively elucidate subtle morphological changes within the retinal layers provides information that could potentially be useful in the treatment of retinal diseases. This feature provides SD-OCT with a clear superiority over other clinical techniques that do not possess the same resolution. First, high-resolution cross-sectional images allow better visualization of the vitreoretinal interface, the vitreous, retinal structures, and the choroid. Furthermore, 3D images depict volumetric topographic retinal morphology that can be registered relative to images acquired at a different time point and, therefore, change in retinal morphology can be calculated. Second, while taking a follow-up image of a particular patient, the software is capable of automatically and accurately registering images so that the identical retinal area is used to calculate change. This added functionality eliminates the possibility of human error and makes it easier to analyze the data with greater validity. However, automated segmentation of the internal limiting membrane and Bruch's membrane sometimes requires manual adjustment prior to analysis in patients with retinal diseases.

Nevertheless, SD-OCT has its limitations. This paper clearly demonstrates that hyperreflective lesions such as exudates and haemorrhages, as well as major retinal vessels, resulted in shadowing of the underlying retinal structures, and thereby details of the underlying morphology are lost. In the case exhibiting choroidal neovascular membrane

(i.e., Case 1), and diabetic retinopathy/macular edema where the retinal thickness was over 400 μm, it was hard to discern the underlying pathology and choroid.

5. Conclusion

SD-OCT imaging technology offers a previously unattainable resolution of retinal morphology. The ability of SD-OCT to clearly and objectively elucidate subtle morphological changes within the retinal layers provides information that can be used to potentially formulate diagnoses earlier and with greater confidence. The current generation of SD-OCT instruments will not replace clinical retinal evaluation but do offer further information that can be valuable from a clinical perspective.

Statement Summary

This study illustrates the potential and limitations of SD-OCT imaging technology. It demonstrated the ability of SD-OCT to clearly and objectively elucidate subtle morphological changes within the retinal layers that are not visible using conventional clinical techniques. Such information may be useful for the earlier diagnosis and treatment of retinal diseases.

Acknowledgments

This paper received funding from the Vision Science Research Program (VSRP), Canadian Institute of Health Research (CIHR), and an anonymous donor. John Flanagan is a consultant for Heidelberg Engineering. This study was presented at the Association for Research in Vision and Ophthalmology Annual Meeting (Fort Lauderdale, USA, 2009).

References

[1] W. Drexler, "Cellular and functional optical coherence tomography of the human retina: the cogan lecture," *Investigative Ophthalmology and Visual Science*, vol. 48, no. 12, pp. 5340–5351, 2007.

[2] W. Drexler and J. G. Fujimoto, "State-of-the-art retinal optical coherence tomography," *Progress in Retinal and Eye Research*, vol. 27, no. 1, pp. 45–88, 2008.

[3] Z. Ma, R. K. Wang, F. Zhang, and J. Yao, "High-speed spectral domain optical coherence tomography for imaging of biological tissues," in *Proceedings of the Optics in Health Care and Biomedical Optics: Diagnostics and Treatment II*, B. Chance, M. Chen, A. E. T. Chiou, and Q. Luo, Eds., vol. 5630 of *Proceedings of SPIE*, pp. 286–294, Beijing, China, November 2004.

[4] M. Wojtkowski, R. Leitgeb, A. Kowalczyk, T. Bajraszewski, and A. F. Fercher, "In vivo human retinal imaging by Fourier domain optical coherence tomography," *Journal of Biomedical Optics*, vol. 7, no. 3, pp. 457–463, 2002.

[5] J. F. De Boer, B. Cense, B. H. Park, M. C. Pierce, G. J. Tearney, and B. E. Bouma, "Improved signal-to-noise ratio in spectral-domain compared with time-domain optical coherence tomography," *Optics Letters*, vol. 28, no. 21, pp. 2067–2069, 2003.

[6] Heidelberg Enginneering, "Spectralis hardware operating instructions," Technical Specifications, pp. 22–25, 2007.

[7] D. M. Luviano, M. S. Benz, R. Y. Kim et al., "Selected clinical comparisons of spectral domain and time domain optical coherence tomography," *Ophthalmic Surgery Lasers & Imaging*, vol. 40, no. 3, pp. 325–328, 2009.

[8] M. Singh and C. K. L. Chee, "Spectral domain optical coherence tomography imaging of retinal diseases in Singapore," *Ophthalmic Surgery Lasers & Imaging*, vol. 40, no. 3, pp. 336–341, 2009.

[9] A. Hassenstein and C. H. Meyer, "Clinical use and research applications of Heidelberg retinal angiography and spectral-domain optical coherence tomography—a review," *Clinical & Experimental Ophthalmology*, vol. 37, no. 1, pp. 130–143, 2009.

[10] H. M. Helb, P. Charbel Issa, M. Fleckenstein et al., "Clinical evaluation of simultaneous confocal scanning laser ophthalmoscopy imaging combined with high-resolution, spectral-domain optical coherence tomography," *Acta Ophthalmologica*, vol. 88, no. 8, pp. 842–849, 2010.

Hindawi Publishing Corporation
Journal of Ophthalmology
Volume 2011, Article ID 692574, 9 pages
doi:10.1155/2011/692574

Research Article

Assessing Errors Inherent in OCT-Derived Macular Thickness Maps

Daniel Odell,[1] Adam M. Dubis,[2] Jackson F. Lever,[3] Kimberly E. Stepien,[1] and Joseph Carroll[1,2,4]

[1] *Department of Ophthalmology, Medical College of Wisconsin, Milwaukee, WI 53226, USA*
[2] *Department of Cell Biology, Neurobiology, & Anatomy, Medical College of Wisconsin, Milwaukee, WI 53226, USA*
[3] *Department of Ophthalmology, William Beaumont Hospital, Royal Oak, MI 48073, USA*
[4] *Department of Biophysics, Medical College of Wisconsin, Milwaukee, WI 53226, USA*

Correspondence should be addressed to Joseph Carroll, jcarroll@mcw.edu

Received 27 January 2011; Accepted 24 June 2011

Academic Editor: Eduardo Buchele Rodrigues

SD-OCT has become an essential tool for evaluating macular pathology; however several aspects of data collection and analysis affect the accuracy of retinal thickness measurements. Here we evaluated sampling density, scan centering, and axial length compensation as factors affecting the accuracy of macular thickness maps. Forty-three patients with various retinal pathologies and 113 normal subjects were imaged using Cirrus HD-OCT. Reduced B-scan density was associated with increased interpolation error in ETDRS macular thickness plots. Correcting for individual differences in axial length revealed modest errors in retinal thickness maps, while more pronounced errors were observed when the ETDRS plot was not positioned at the center of the fovea (which can occur as a result of errant fixation). Cumulative error can exceed hundreds of microns, even under "ideal observer" conditions. This preventable error is particularly relevant when attempting to compare macular thickness maps to normative databases or measuring the area or volume of retinal features.

1. Introduction

Optical coherence tomography (OCT) provides high-resolution, cross-sectional tomographic images of the human retina and permits direct evaluation of retinal thickness [1]. In recent years the development of spectral-domain OCT (SD-OCT) technology has greatly increased imaging speed and resolution relative to earlier time-domain technology. SD-OCT has become invaluable in the management of a variety of retinal diseases including neovascular age-related macular degeneration (AMD) [2–5] and diabetic macular edema [6, 7]. This utility is due primarily to the ability to extract estimates of retinal thickness across the macula (to aid in clinical diagnosis and treatment decisions).

Previous studies on the application of SD-OCT to retinal pathology have uncovered multiple sources of error that dramatically decrease the accuracy of these macular thickness measurements [8, 9]. Perhaps the most obvious source of error is imprecise retinal layer segmentation, which can result from poor signal quality of the SD-OCT image or the outright failure in the segmentation algorithm itself in otherwise high-quality images [8, 10, 11]. Additional errors inherent to the system can be elucidated by evaluating the reproducibility of SD-OCT systems [9, 12–17]. These reproducibility studies capture all errors inherent to the basic operation of the SD-OCT system and represent a baseline level of error that could reasonably be expected even under the best circumstances.

However, there are additional sources of inaccuracy that have received considerably less attention and are independent of segmentation and operator errors. Rather they pertain to instrument sampling and processing protocols. For example, Sadda et al. compared central subfield thickness values from volumes containing 128 B-scans to less densely sampled volumes [18]. As B-scan density is reduced, less retinal area is sampled, leading to less data being included in the retinal thickness calculation. The reduction in data led to differences, or errors, in retinal thickness measurements,

the magnitude of which increased as sampling density was decreased [18]. Here, we further examined B-scan density as well as factors that are related to assumptions about the patient being imaged, such as errant fixation and variation in axial length among patients. Taken together, these variables compromise the accuracy of macular thickness maps. While the degree of inaccuracy depends on the patient, the significance of the inaccuracy depends on the application of the retinal thickness data.

2. Materials and Methods

2.1. Subjects. One hundred thirteen normal subjects (55 male, 58 female) age 18 years and older were recruited for SD-OCT imaging (mean ± standard deviation = 27.3 ± 8.3 years). Normal subjects had normal color vision assessed with the Neitz Test of Color Vision [19] and no history of refractive surgery or any vision-limiting ocular pathology. Forty-three patients (18 male, 25 female) with various retinal pathologies were also recruited (mean ± standard deviation = 40.7 ± 20.1 years). Pathology included macular dystrophy ($n = 9$), blue cone monochromacy ($n = 3$), X-linked high myopia ($n = 4$), basal laminar drusen ($n = 5$), retinitis pigmentosa ($n = 2$), AMD ($n = 3$), plaquenil toxicity ($n = 3$), diabetic macular edema ($n = 3$), macular telangectasia ($n = 2$), central artery occlusion ($n = 2$), and one each of oligocone trichromacy, posterior epithelial detachment, oculocutaneous albinism, punctate inner choroidopathy, achromatopsia, cystoid macular edema, and acute zonal occult outer retinopathy. Informed consent was obtained from all subjects after explanation of the nature and possible consequences of the study. All research on human subjects followed the tenets of the Declaration of Helsinki and was approved by the Institutional Review Board at Children's Hospital of Wisconsin.

2.2. SD-OCT Retinal Imaging. Volumetric SD-OCT images of the macula were obtained using the Cirrus HD-OCT (Carl Zeiss Meditec, Dublin, Calif, USA). Volumes were nominally 6 mm × 6 mm and consisted of 128 B-scans (512 A-scans/B-scan). The internal fixation target of the system was used, which consists of a large green asterisk on a red background, and focus of the LSO fundus image was optimized using built-in focus correction. In addition, the polarization setting was optimized using the built-in function for each eye. Retinal thickness was calculated using the built-in Macular Analysis software on the Cirrus (software version 5.0), which is automatically determined by taking the difference between the ILM and RPE boundaries [20]. The positions of the foveal center and retinal thickness data from each volume scan were exported for offline analysis using the Zeiss Cirrus Research Browser (version 5.0). All volumes were manually examined for accuracy of the ILM and RPE segmentation and relative accuracy of the Autofovea function.

2.3. Manipulation of Macular Thickness Maps. In order to evaluate the acquisition and analysis parameters of interest, we needed to be able to manipulate these macular thickness maps off line. Custom Matlab (Mathworks, Natick, Mass, USA) software was used to generate early treatment diabetic retinopathy study (ETDRS) thickness maps from the .dat files exported from the Zeiss Cirrus Research Browser. As shown in Figure 1, there is good agreement between ETDRS segment thicknesses derived from the on-board Cirrus software and our offline Matlab program, thus demonstrating the fidelity of the data export and validating our use of these Matlab-derived ETDRS maps for subsequent analysis.

To assess the interpolation error in volumetric retinal thickness maps due to decreased B-scan sampling, we created undersampled versions of the retinal thickness volumes exported from the Cirrus system. These maps used thickness values from 8 (every 16th B-scan), 16 (every 8th B-scan), 32 (every 4th B-scan), or 64 (every other B-scan) of the 128 B-scans initially collected. Complete thickness maps were then created by interpolating between these evenly spaced B-scans (using a Matlab spline interpolation function). This enabled point-by-point comparison between the native macular thickness map and the undersampled ones, as well as comparison between the corresponding ETDRS plots. In all ETDRS comparisons, mean differences were computed using absolute differences.

Most SD-OCT systems assume foveal fixation; however there is frequently significant discrepancy between the location of the fovea and the preferred retinal locus of fixation. Even among individuals with no retinal pathology, there is modest variation in fixation and there is evidence that suggests that the foveal center is not always used for fixation [21–24]. We used the Autofovea function of the Cirrus HD-OCT to identify the location of the foveal pit and generated an ETDRS plot centered at this location and a second plot centered at the middle of the volume (the default setting on most other SD-OCT systems). Manual inspection of each volume confirmed that the fovea was identified by the Autofovea function (though in more severe macular pathology we have seen the algorithm fail). Comparing these two ETDRS plots provides an estimate of the potential error due to improper anchoring of the plot to the scan center. Moreover, as we had access to the (x, y) coordinate of the fovea within each nominal 6 mm × 6 mm volume, we examined error as a function of the displacement of each subject's fixation from the center of his or her foveal pit.

The scan length reported by SD-OCT systems (when reported in mm) is relative, not absolute. This is because the scanning mirrors are calibrated to a model eye, which assumes a fixed axial length (typically around 24 mm). However there exist significant individual differences in retinal magnification (primarily caused by differences in axial length); thus the actual scan length will vary from person to person. In fact, using normative axial length data [25] to correct for ocular magnification [26], we estimate that approximately one-third of individuals would have a scan length that deviates by more than 0.3 mm from the expected length (with a maximum deviation of nearly 1 mm). We obtained axial length measurements using the Zeiss IOL Master (Carl Zeiss Meditec, Dublin, Calif, USA) and subsequently calibrated the lateral scale of each subject's SD-OCT scans in order to generate revised ETDRS plots.

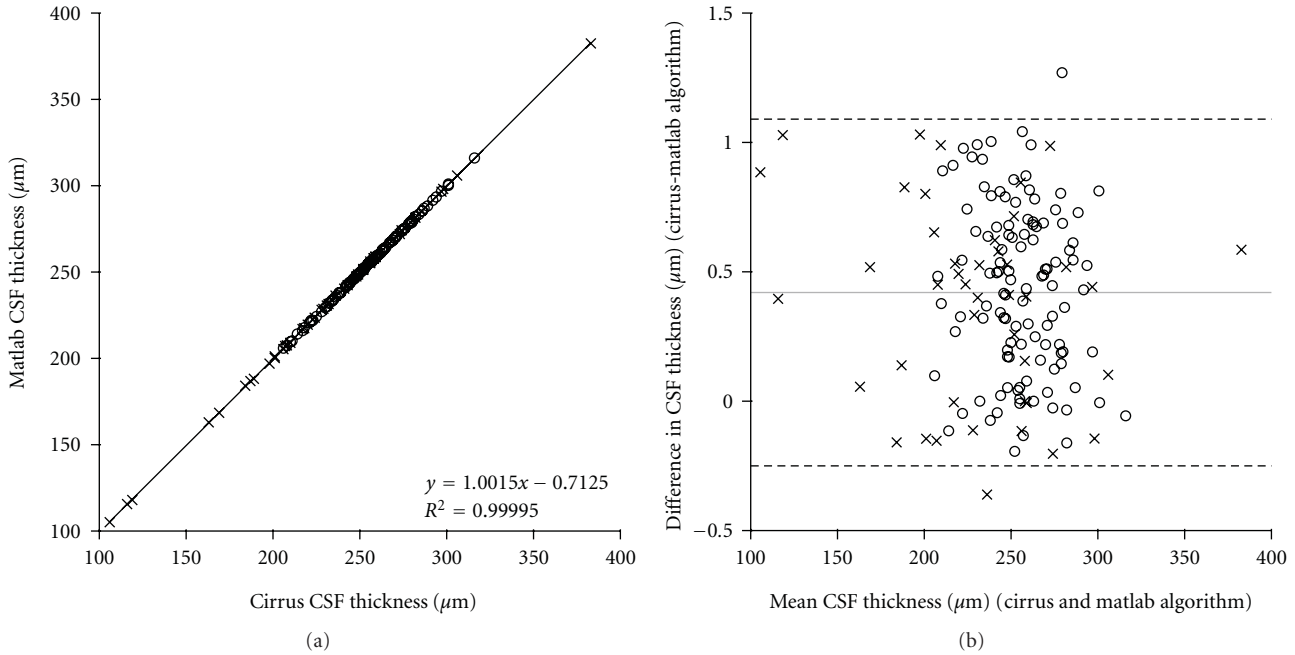

(a) (b)

Figure 1: A custom MatLab program was designed to generate ETDRS thickness plots from the raw thickness data exported using the Cirrus Research Browser. (a) Central subfield thickness values taken directly from the Cirrus correlate highly with those obtained from our Matlab-based algorithm. (b) Bland-Altman plot further reveals excellent agreement between the two measurements. Gray line represents the mean difference between the measurements (0.42 μm), and the dashed lines represent 95% confidence limits (1.09 μm and -0.25 μm). These data indicate virtually no loss in accuracy when using the MatLab derived thickness maps for subsequent analysis. *Open circles*: normals; *crosses*: pathology subjects; CSF = central subfield.

These plots were then compared to those derived assuming a 24.46 mm axial length (that of the Cirrus model eye).

3. Results

3.1. Effect of B-Scan Sampling Density on Accuracy of Retinal Thickness Measurements. Despite the macular volume scan nominally subtending a 6 mm × 6 mm area, the entire retinal area within that volume is not actually scanned. As shown in Figure 2, even a scan using 512 A-scans/B-scan and 128 B-scans only samples 29% of the retinal area within the volume. Using 37 high-resolution B-scans results in less than 10% of the retinal area within the volume actually being scanned. As only retina that gets scanned can actually contribute to plots of retinal thickness measurements, this undersampling can significantly affect the integrity of the resultant macular thickness maps.

At first glance, assessment of the effect of B-scan density on macular thickness maps suggests that despite reducing the number of B-scans, the general contour of the map remains qualitatively similar (Figure 3(a)). However in reality, interpolation between B-scans causes overrepresentation and underrepresentation of different features within a given retinal volume (Figure 3(b)). As shown in the normal example, since sampling is being reduced in the vertical direction, the superior and inferior aspects of the fovea show equal magnitude of underrepresentation and overrepresentation of retinal thickness, respectively. This effect is greatly enhanced in a subject with dominant drusen, wherein error is generated not only in the central fovea but also broadly across the retinal volume.

We found that in the normal individuals for the central 1 mm subfield, the mean (± standard deviation) absolute error was 0.19 ± 0.15 μm with 64 B-scans, 1.17 ± 0.69 μm with 32 B-scans, 7.15 ± 2.35 μm with 16 B-scans, and 22.98 ± 7.54 μm with 8 B-scans. When expressed as a percentage of subfield thickness we find that the mean percentage error was 0.07 ± 0.06% with 64 B-scans, 0.47 ± 0.29% with 32 B-scans, 2.85 ± 1.08% with 16 B-scans, and 9.19 ± 3.52% with 8 B-scans. We found similar differences in the individuals with retinal pathology. For the central 1 mm subfield, the mean (± standard deviation) absolute error was 0.31 ± 0.36 μm with 64 B-scans, 1.36 ± 1.17 μm with 32 B-scans, 6.35 ± 3.64 μm with 16 B-scans, and 19.56 ± 11.08 μm with 8 B-scans. When expressed as a percentage of subfield thickness we find that the mean percentage error was 0.13 ± 0.15% with 64 B-scans, 0.63 ± 0.56% with 32 B-scans, 3.03 ± 2.14% with 16 B-scans, and 9.56 ± 6.92% with 8 B-scans. Previous data reveal that the coefficient of repeatability for central subfield measurements on the Cirrus is about 4.96 μm, indicating that 32 B-scans is sufficient sampling to generate accurate ETDRS thickness plots.

However, as shown in the difference plots in Figure 3, at neighboring retinal locations where the retinal contour is changing, retinal thickness measurements are in error in opposing directions. Thus, reporting retinal thickness for a subregion that averages spatially (i.e., ETDRS plots) will not reveal the true extent of the error imparted by undersampling. In order to quantify the effect of B-scan density on the accuracy of retinal thickness at any given point within the 6 mm × 6 mm volume, we examined the error per pixel ("A scan") within the volume. In this case, the

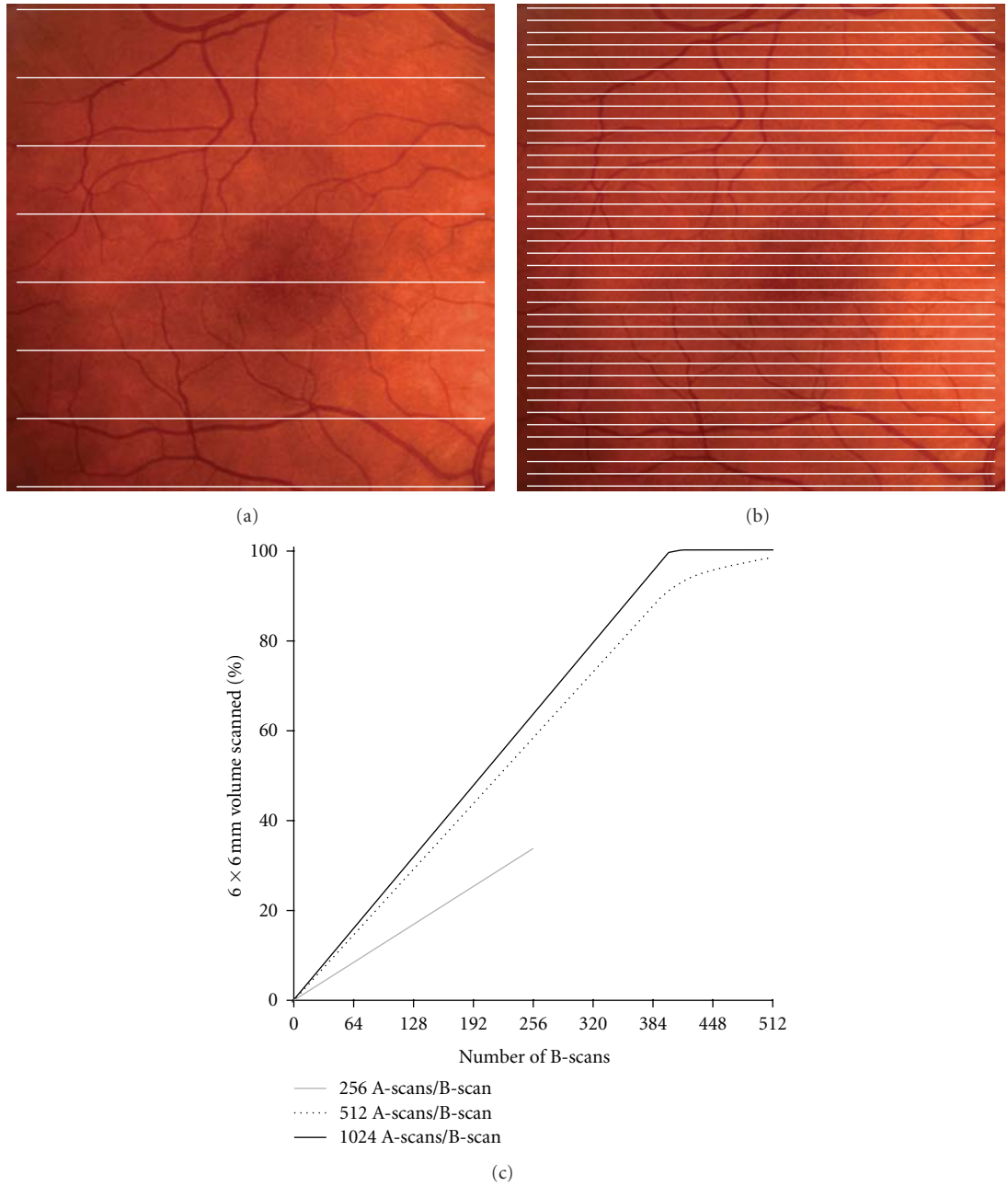

Figure 2: Reduction in B-scan sampling results in less retinal area being scanned. (a) Eight simulated B-scans spaced 750 μm apart over a 6 mm $\times$ 6 mm volume. At this sampling, assuming a 15 μm spot size and 512 A scans/B-scan, only 1.8% of the volume is scanned. (b) Sixty-four simulated B-scans spaced 94 μm apart over a 6 mm $\times$ 6 mm volume. At this sampling, only 15% of the volume is scanned. (c) Percentage of OCT volume scanned as a function of B-scan density. Complete sampling of the retinal volume at 512 A scans/B-scan would require nearly 600 B-scans.

retinal thickness measurements utilizing all 128 B-scans were considered to be absolutely accurate for comparison to the undersampled volumes. At 32 B-scans, our analysis revealed that these interpolation errors could be as high as 5.5 μm per pixel and 7.5 μm per pixel in the normal and pathology groups, respectively. There are 65,536 pixels in each of our thickness maps, native or undersampled. In both groups, on average, the error per pixel increases as the number of B-scans used to construct the retinal thickness map decreases (Figure 4).

3.2. Position of SD-OCT Volume with Respect to the Fovea and ETDRS Plot Accuracy. We compared ETDRS thickness plots derived by placing the center of the ETDRS grid on the foveal center to those plots centered on the subject's actual fixation point. We found these plots to differ by over 100 μm in some normal individuals (sum of the error in all nine ETDRS segments), with the mean error being 14.4 $\pm$ 19.3 μm (Figure 5(a)). In the 43 pathology cases, the mean error was 30.4 $\pm$ 40.9 μm, with some individuals exceeding 200 μm of total error in their ETDRS plots (Figure 5(b)). Of course if

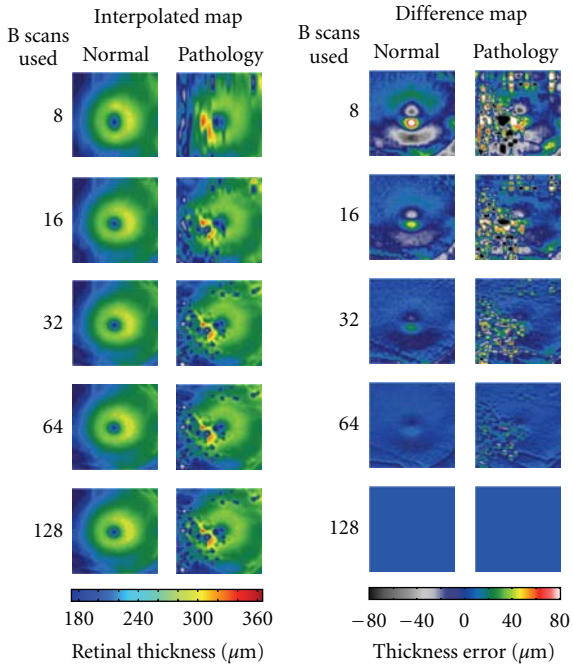

Figure 3: Two examples of how interpolation between B-scans results in inaccurate macular thickness maps. (a) Undersampled thickness maps from a single normal subject and one with dominant drusen retain relatively similar qualitative appearance to that of their respective 128 B-scan maps. (b) The thickness differences between the standard of 128 scans and each sequential level of B-scan density show the areas of the macula most effected by undersampling in a normal subject and a subject with dominant drusen. Even with 32 B-scans significant error is generated through the central fovea (where the contour is changing most rapidly) in a normal subject. This effect is greatly enhanced in the subject with drusen wherein error is generated not only in the central fovea but also broadly across the entire scanning area.

eccentric fixation is identified by the OCT operator, the scan location can be repositioned prior to image acquisition to help reduce this error. For two pathology cases, we acquired one scan at their normal eccentric fixation location and a second after moving the scan to be visually centered on the fovea. At their normal fixation position, these subjects had ETDRS plots that deviated by 74.5 μm and 101.9 μm from an ETDRS plot precisely positioned at the foveal center (using our offline MatLab program). Even after the operator acquired a second scan intentionally centered on the fovea to the best of their ability, ETDRS errors persisted of 16.3 μm and 17.8 μm. Regardless, for both normal subjects and subjects with retinal pathology, the greater the distance between the fovea and the center of the SD-OCT volume, the less accurate the ETDRS thickness map. In just the central subfield thickness, not correcting for scan position results in a mean error of 3.18 $\pm$ 6.09 μm in the normal subjects (with a maximum error of 32 μm) and 10.50 $\pm$ 19.43 μm in the patients with retinal pathology (with a maximum error of 104 μm). On average, the central subfield error accounts for 14% and 22% of the total ETDRS error in the normal and pathology patients, respectively.

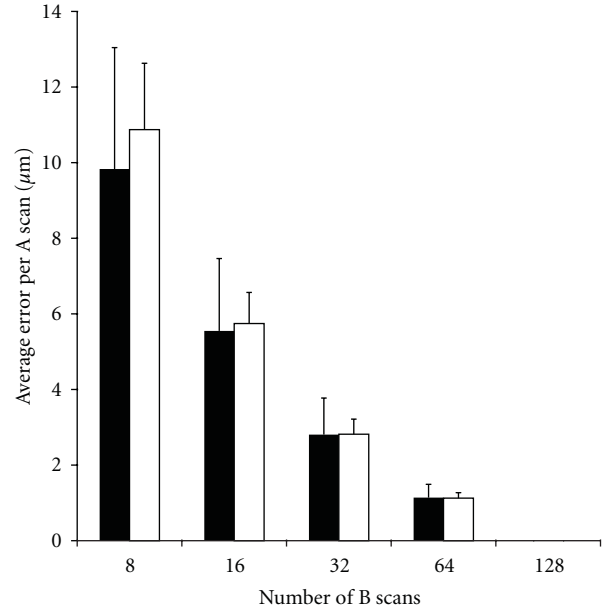

Figure 4: The impact of undersampling for retinal thickness measurements. As fewer B-scans are used, the average error per pixel (A scan) increases. This value was obtained by first subtracting each undersampled macular thickness map from the native 128 B-scan thickness map and then dividing the difference by the number of pixels (A scans).

3.3. The Effect of Ocular Magnification on ETDRS Plot Accuracy. Axial length varied in our normal subjects from 21.56 to 28.36 mm and in pathology patients from 21.87 to 30.13 mm. Using each subject axial length to correct the lateral scale of the nominal 6 mm SD-OCT scan, we determined that actual scan sizes range from about 5.29 to 6.96 mm for our normal population and 5.36 to 7.4 mm for our pathological population. We used these corrected scan dimensions to derive corrected ETDRS plots, where the rings were actually 1 mm, 3 mm, and 6 mm in diameter. In comparing these plots to the uncorrected ones, we found that the summed error for the nine ETDRS segments was as much as 44.9 μm, with 37 out of 113 (32%) subjects having more than 20 μm of total error. For subjects with retinal pathology the summed error for the nine ETDRS segments was as much as 77.3 μm, and 13 out of 43 (30%) showed more than 20 μm of total error (Figure 6). In just the central subfield alone, the error was as much as 7.86 μm (with an average of 2.56 $\pm$ 1.85 μm) for the normals and as much as 12.33 μm (with an average of 2.84 $\pm$ 2.46 μm) in the individuals with retinal pathology. In both groups, the error increased with increasing difference in axial length from that of the model eye (24.46 mm).

3.4. The Combined Error due to Ocular Magnification and Scan Positioning. As illustrated above, not correcting for axial length and not positioning the scan at the center of the fovea introduces significant error in the corresponding ETDRS thickness plots. Taken together, these artifacts tend to have a cumulative negative effect on the accuracy of the

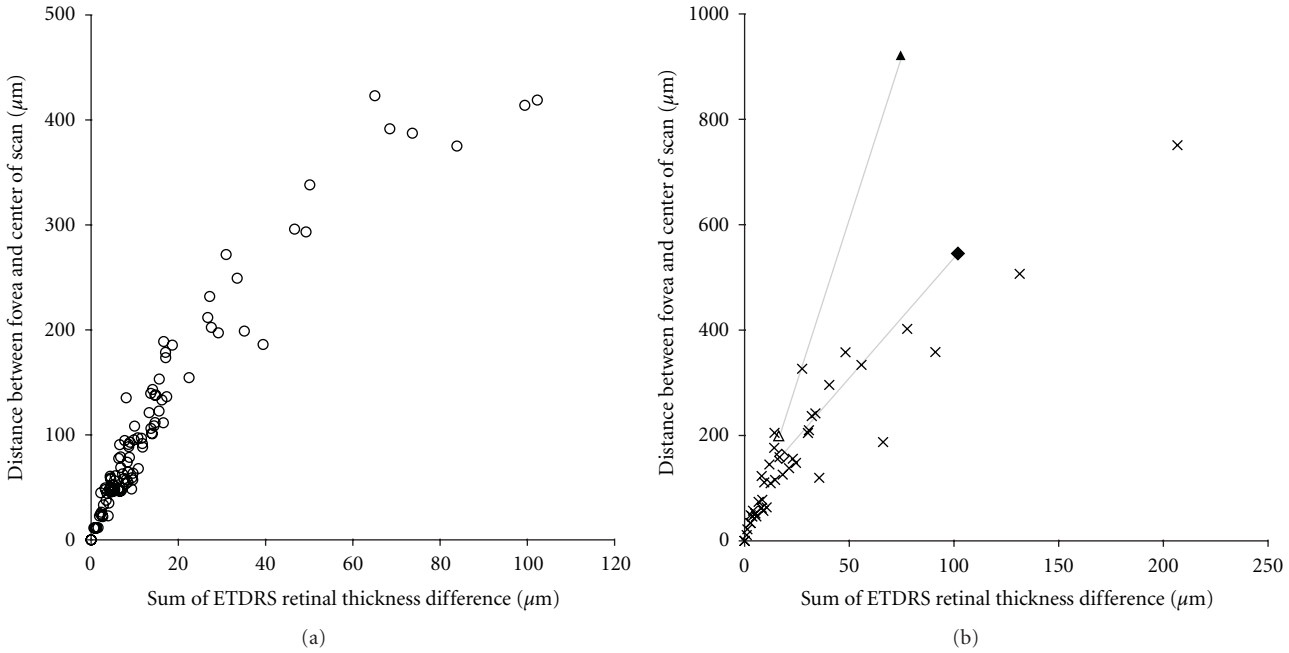

Figure 5: Measuring the effect of scan position on accuracy of ETDRS thickness plots. For each subject, we estimated this error by comparing the raw ETDRS thickness plot to one that has been repositioned to be centered on their fovea. In the normal individuals (a), the summed error across the nine ETDRS segments could be as much as 100 μm, while in individuals with pathology (b) the error could exceed 200 μm. For some pathology cases, nonfoveal fixation can be compensated for by moving the location of the OCT scan. For 2 individuals, we acquired scans at their eccentric fixation location (filled triangle and diamond) and a second scan after the operator manually moved the scan to be centered on the fovea (open triangle and diamond, connected by thin gray lines). Even when using the repositioned scan, residual error remains, though it is on the order of that observed for the other patients.

ETDRS plots. For example, in considering just the central subfield thickness, not correcting for axial length or scan position results in a mean error of 4.53 $\pm$ 5.77 μm in the normal subjects (with a maximum combined error of 33 μm) and 11.29 $\pm$ 19.18 μm in the patients with retinal pathology (with a maximum combined error of 105 μm).

4. Discussion

This study examined the effects of preventable operational and analytic aspects of the SD-OCT on the overall accuracy of ETDRS retinal thickness plots. Scan density, position of the scan with respect to the foveal center, and magnitude of subject axial length differential all contribute to significant error in computing retinal thickness from SD-OCT volumes. An important point to consider is the cumulative nature of the errors reported here; these parameters should all be accounted for when developing normative databases or analyzing specific retinal features within individual patient data. While the errors were estimated using a single SD-OCT device (Cirrus HD-OCT), they are generic to SD-OCT imaging in general. The issue of scan positioning is typically something that can be addressed by the operator by repositioning the ETDRS grid (either manually or using an automatic function like Autofovea). Currently, correcting the lateral scale of OCT data/images requires offline correction by the user.

In comparing our results to previously published data, we find similarities and differences. In an examination of B-scan density, Sadda et al. concluded that 32 B-scans result in only a minimal change in retinal thickness [18]. Our data also show that when examining maps of retinal thickness that are based on spatially integrating individual thickness values (i.e., ETDRS), reduced B-scan sampling has minimal impact. However, if interested in deriving absolute measures of retinal thickness at any given point, reduction to 32 B-scans (a value suggested to provide accurate retinal thickness maps), results in an average error of around 3 μm per pixel. While this average error is within the system resolution on commercial SD-OCT systems, it is worth keeping in mind that the error at any one pixel can be much larger, since not all pixels will contribute equally to the total error (which is implicit in computing an average error). We feel this more accurately reflects the "real" cost of undersampling, and this would significantly limit the ability to make precise measurements of retinal features (e.g., drusen). This highlights the importance of considering how the SD-OCT data is going to be used when deciding how densely to sample the retina.

It is well documented that differences in axial length result in different ocular magnification of retinal images and thus can affect the accuracy of measurements of retinal features [27]. With respect to OCT, axial length has been shown to influence measurements of retinal nerve fiber

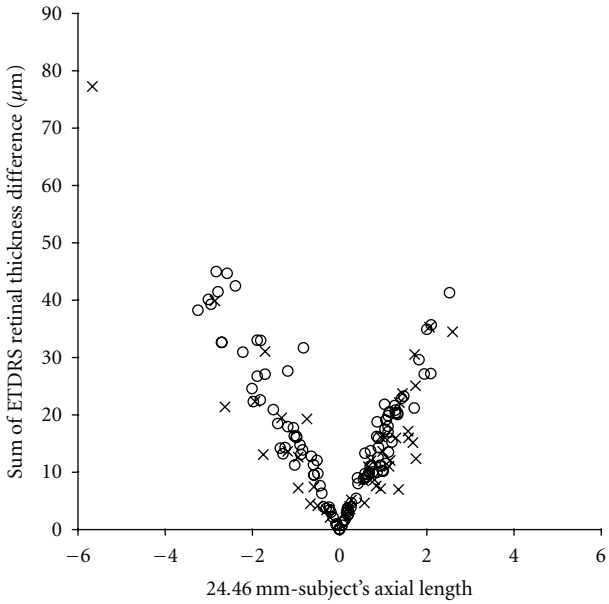

Figure 6: The effect of axial length on the accuracy of ETDRS thickness plots. For each subject, we compared the raw ETDRS thickness plot assuming a 6 mm scan size to an ETDRS thickness plot using a scan length corrected for their axial length. As the deviation in axial length increases, the error in ETDRS thickness plots (sum of all nine ETDRS segments) becomes greater, both for the normal subjects (open circles) and the pathology subjects (crosses).

layer (RNFL) thickness [28–31]. This of course is based on the fact that RNFL measures are presumed to be taken at a fixed distance from the optic nerve; thus individual differences in ocular magnificent would result in the RNFL being measured at the wrong location. Here we demonstrate that individual differences in ocular magnification also affect the accuracy of macular thickness maps. If the distribution of axial lengths in a normative database does not match that of the subject population being studied, misinterpretation can occur. Perhaps more important than retinal thickness maps is the fact that not correcting the nominal scan length for differences in axial length will obviate making reliable measurements in the lateral dimension within a given OCT dataset. This could include measuring the area of geographic atrophy, the size of a macular hole, or the size of a druse. Despite this, some SD-OCT systems still output lateral scale bars on their images that are given in μm or provide calipers with which to make lateral measurements in μm, despite no correction for axial length having been made. One should avoid using such scale bars to report absolute length measurements, as they are simply not accurate without first taking into account ocular magnification.

There have also been previous examinations of the effect of fixation on the accuracy of OCT thickness measurements. In glaucoma, it has been shown that if the circular scan is not centered on the ONH, the RNFL thickness measurements are inaccurate [32]. Campbell et al. [33] examined how intentionally shifting the center of macular volume OCT scans (Stratus time-domain) affected central subfield thickness measurements for 10 normal subjects. They found that scan decentration of 0.50 mm resulted in foveal thickness measurements that were in error by about 45%. For our normal subjects, the average decentration of the SD-OCT volume with respect to the foveal center was 0.09 mm and the average error of foveal thickness measurements was about 35%. While this is roughly consistent with the finding of Campbell et al. [33], some discrepancy would be expected given our use of SD-OCT (instead of time domain) and our ability to precisely determine the exact misalignment between the two scans being compared (whereas the previous study would have be confounded by errors due to normal fixational instability). Currently, the Cirrus HD-OCT will automatically position the ETDRS grid over the center of the fovea (after the scan is taken). While this results in a more accurate ETDRS map, it may not be valid to compare these maps to a database in which the ETDRS maps were not centered on the fovea, though in the case of the Cirrus database, good centration of the volume on the fovea was an inclusion criterion. It is generally important to ensure that the scan parameters used to develop the normative database match that of the on-board scan protocol. Moreover, the subject composition (race and gender) may also need to be considered when comparing a specific patient to a particular normative database [12].

There are several limitations to the present study. First, in our examination of B-scan sampling, we used 128 B-scans as the "truth". This was simply due to a limitation of the specific SD-OCT device being used. However, as we showed in Figure 2, 128 B-scans (at 512 A scans/B-scan) only sample 29% of the nominal 6 m $\times$ 6 mm volume. Thus these volumes are likely already in error compared to an isotropic volume of 512 B-scans. With the expected availability of even faster OCT systems, it will be important to quantify the level of inaccuracy systematically across more densely sampled volumes. In addition, we likely underestimate the real effect of undersampling, as we used simulated thickness maps. If one were to really only acquire 32 B-scans, this could affect the accuracy of segmentation as many OCT devices use 3D approaches to make correct assignment of layers. A second limitation is that we corrected for ocular magnification using a linear scaling based on axial length. There are other methods to correct for ocular magnification [26], and the exact method used for the correction would influence the measured differences in retinal image magnification. Finally, we did not subanalyze different pathologies. It seems likely that different retinal pathology would suffer more (or less) than others. Intuitively, one can conclude that the more uniform the retinal thickness contoured (as might occur in retinitis pigmentosa, where the retina is uniformly thin), the less impact the B-scan sampling, axial length, and scan position would have. Likewise, retinal pathology that results in significant peaks and troughs in retinal thickness (macular holes, AMD, diabetic macular edema) might be more significantly influenced by these parameters. A more detailed, disease-specific analysis is required to clarify this issue.

It is important to keep in mind that the relevance of these errors of course ultimately depends on the clinical application. For monitoring patients over time, relative differences in retinal thickness would be generally unaffected by axial length, though comparing populations of patients (such as in a clinical trial) where there may be differences in axial length between the groups could result in significant error. If one uses the same sampling density, then the accuracy of these longitudinal measurements of retinal thickness will be on the order of that reported for previous repeatability and reproducibility studies. However, in instances where one is interested in correlating a measure of retinal thickness over a specific retinal area (e.g., central subfield thickness) with some other measure of vision (such as treatment response) these errors could reveal correlations that do not exist or hide ones that do exist. Moreover, where one is interested in making absolute measurements in the lateral dimension, such as foveal pit morphology [12, 34] or drusen volume [35], it is critical that these sources of error be removed.

Acknowledgments

J. Carroll is the recipient of a Career Development Award from the Research to Prevent Blindness. This study was supported by NIH Grants R01EY017607, P30EY001931, and T32EY014537, the Gene and Ruth Posner Foundation, the Thomas M. Aaberg, Sr., Retina Research Fund, and an unrestricted departmental grant from Research to Prevent Blindness. This investigation was conducted in a facility constructed with support from Research Facilities Improvement Program Grant no. C06 RR-RR016511 from the National Center for Research Resources, National Institutes of Health. The authors thank P. M. Summerfelt for technical assistance. Both D. Odell and A. M. Dubis contributed equally to this work.

References

[1] D. Huang, E. A. Swanson, C. P. Lin et al., "Optical coherence tomography," *Science*, vol. 254, no. 5035, pp. 1178–1181, 1991.

[2] G. A. Lalwani, P. J. Rosenfeld, A. E. Fung et al., "A variable-dosing regimen with intravitreal ranibizumab for neovascular age-related macular degeneration: year 2 of the PrONTO study," *American Journal of Ophthalmology*, vol. 148, no. 1, pp. 43–58, 2009.

[3] M. Ritter, J. Elledge, C. Simader et al., "Evaluation of optical coherence tomography findings in age-related macular degeneration: a reproducibility study of two independent reading centres," *British Journal of Ophthalmology*, vol. 95, no. 3, pp. 381–385, 2011.

[4] A. E. Fung, G. A. Lalwani, P. J. Rosenfeld et al., "An optical coherence tomography-guided, variable dosing regimen with intravitreal ranibizumab (Lucentis) for neovascular age-related macular degeneration," *American Journal of Ophthalmology*, vol. 143, no. 4, pp. 566–583, 2007.

[5] S. Schmitz-Valckenberg, M. Fleckenstein, A. P. Göbel, T. C. Hohman, and F. G. Holz, "Optical coherence tomography and autofluorescence findings in areas with geographic atrophy due to age-related macular degeneration," *Investigative Ophthalmology & Visual Science*, vol. 52, no. 1, pp. 1–6, 2011.

[6] D. E. Baskin, "Optical coherence tomography in diabetic macular edema," *Current Opinion in Ophthalmology*, vol. 21, no. 3, pp. 172–177, 2010.

[7] B. Y. Kim, S. D. Smith, and P. K. Kaiser, "Optical coherence tomographic patterns of diabetic macular edema," *American Journal of Ophthalmology*, vol. 142, no. 3, pp. 405–412, 2006.

[8] I. Krebs, S. Hagen, W. Brannath et al., "Repeatability and reproducibility of retinal thickness measurements by optical coherence tomography in age-related macular degeneration," *Ophthalmology*, vol. 117, no. 8, pp. 1577–1584, 2010.

[9] U. E. K. Wolf-Schnurrbusch, L. Ceklic, C. K. Brinkmann et al., "Macular thickness measurements in healthy eyes using six different optical coherence tomography instruments," *Investigative Ophthalmology & Visual Science*, vol. 50, no. 7, pp. 3432–3437, 2009.

[10] N. G. Ghazi, T. Kirk, S. Allam, and G. Yan, "Quantification of error in optical coherence tomography central macular thickness measurement in wet age-related macular degeneration," *American Journal of Ophthalmology*, vol. 148, no. 1, pp. 90–96, 2009.

[11] P. A. Keane, P. S. Mand, S. Liakopoulos, A. C. Walsh, and S. R. Sadda, "Accuracy of retinal thickness measurements obtained with Cirrus optical coherence tomography," *British Journal of Ophthalmology*, vol. 93, no. 11, pp. 1461–1467, 2009.

[12] M. Wagner-Schuman, A. M. Dubis, R. N. Nordgren et al., "Race- and sex-related differences in retinal thickness and foveal pit morphology," *Investigative Ophthalmology & Visual Science*, vol. 52, no. 1, pp. 625–634, 2011.

[13] M. Parravano, F. Oddone, B. Boccassini et al., "Reproducibility of macular thickness measurements using Cirrus SD-OCT in neovascular age-related macular degeneration," *Investigative Ophthalmology & Visual Science*, vol. 51, no. 9, pp. 4788–4791, 2010.

[14] F. Forooghian, P. F. Stetson, S. A. Meyer et al., "Relationship between photoreceptor outer segment length and visual acuity in diabetic macular edema," *Retina*, vol. 30, no. 1, pp. 63–70, 2010.

[15] C. K. S. Leung, C. Y. L. Cheung, R. N. Weinreb et al., "Comparison of macular thickness measurements between time domain and spectral domain optical coherence tomography," *Investigative Ophthalmology & Visual Science*, vol. 49, no. 11, pp. 4893–4897, 2008.

[16] M. N. Menke, S. Dabov, and V. Sturm, "Comparison of three different optical coherence tomography models for total macular thickness measurements in healthy controls," *Ophthalmologica*, vol. 223, no. 6, pp. 352–356, 2009.

[17] A. C. Sull, L. N. Vuong, L. L. Price et al., "Comparison of spectral/Fourier domain optical coherence tomography instruments for assessment of normal macular thickness," *Retina*, vol. 30, no. 2, pp. 235–245, 2010.

[18] S. R. Sadda, P. A. Keane, Y. Ouyang, J. F. Updike, and A. C. Walsh, "Impact of scanning density on measurements from spectral domain optical coherence tomography," *Investigative Ophthalmology & Visual Science*, vol. 51, no. 2, pp. 1071–1078, 2010.

[19] M. Neitz and J. Neitz, "A new mass screening test for color-vision deficiencies in children," *Color Research and Application*, vol. 26, pp. S239–S249, 2001.

[20] J. E. Legarreta, G. Gregori, O. S. Punjabi, R. W. Knighton, G. A. Lalwani, and C. A. Puliafito, "Macular thickness measurements in normal eyes using spectral domain optical coherence tomography," *Ophthalmic Surgery Lasers and Imaging*, vol. 39, no. 4, pp. S43–S49, 2008.

[21] H. E. Bedell, "A functional test of foveal fixation based upon differential cone directional sensitivity," *Vision Research*, vol. 20, no. 6, pp. 557–560, 1980.

[22] B. S. Zeffren, R. A. Applegate, A. Bradley, and W. A. J. Van Heuven, "Retinal fixation point location in the foveal avascular zone," *Investigative Ophthalmology & Visual Science*, vol. 31, no. 10, pp. 2099–2105, 1990.

[23] N. M. Putnam, H. J. Hofer, N. Doble, L. Chen, J. Carroll, and D. R. Williams, "The locus of fixation and the foveal cone mosaic," *Journal of Vision*, vol. 5, no. 7, pp. 632–939, 2005.

[24] K. Y. Li, P. Tiruveedhula, and A. Roorda, "Intersubject variability of foveal cone photoreceptor density in relation to eye length," *Investigative Ophthalmology & Visual Science*, vol. 51, no. 12, pp. 6858–6867, 2010.

[25] S. Stenstrom, "Investigation of the variation and the correlation of the optical elements of human eyes," *American Journal of Optometry & Archives of American Academy of Optometry*, vol. 25, no. 7, pp. 340–350, 1948, translated by D. Woolf.

[26] D. F. Garway-Heath, A. R. Rudnicka, T. Lowe, P. J. Foster, F. W. Fitzke, and R. A. Hitchings, "Measurement of optic disc size: equivalence of methods to correct for ocular magnification," *British Journal of Ophthalmology*, vol. 82, no. 6, pp. 643–649, 1998.

[27] A. G. Bennett, A. R. Rudnicka, and D. F. Edgar, "Improvements on Littmann's method of determining the size of retinal features by fundus photography," *Graefe's Archive for Clinical and Experimental Ophthalmology*, vol. 232, no. 6, pp. 361–367, 1994.

[28] S. Bayraktar, Z. Bayraktar, and O. F. Yilmaz, "Influence of scan radius correction for ocular magnification and relationship between scan radius with retinal nerve fiber layer thickness measured by optical coherence tomography," *Journal of Glaucoma*, vol. 10, no. 3, pp. 163–169, 2001.

[29] C. K. S. Leung, S. Mohamed, K. S. Leung et al., "Retinal nerve fiber layer measurements in myopia: an optical coherence tomography study," *Investigative Ophthalmology & Visual Science*, vol. 47, no. 12, pp. 5171–5176, 2006.

[30] F. M. Rauscher, N. Sekhon, W. J. Feuer, and D. L. Budenz, "Myopia affects retinal nerve fiber layer measurements as determined by optical coherence tomography," *Journal of Glaucoma*, vol. 18, no. 7, pp. 501–505, 2009.

[31] C. K. S. Leung, A. C. K. Cheng, K. K. L. Chong et al., "Optic disc measurements in myopia with optical coherence tomography and confocal scanning laser ophthalmoscopy," *Investigative Ophthalmology & Visual Science*, vol. 48, no. 7, pp. 3178–3183, 2007.

[32] S. Asrani, B. Edghill, Y. Gupta, and G. Meerhoff, "Optical coherence tomography errors in glaucoma," *Journal of Glaucoma*, vol. 19, no. 4, pp. 237–242, 2010.

[33] R. J. Campbell, S. G. Coupland, R. R. Buhrmann, and P. J. Kertes, "Effect of eccentric and inconsistent fixation on retinal optical coherence tomography measures," *Archives of Ophthalmology*, vol. 125, no. 5, pp. 624–627, 2007.

[34] A. M. Dubis, J. T. McAllister, and J. Carroll, "Reconstructing foveal pit morphology from optical coherence tomography imaging," *British Journal of Ophthalmology*, vol. 93, no. 9, pp. 1223–1227, 2009.

[35] S. R. Freeman, I. Kozak, L. Cheng et al., "Optical coherence tomography-raster scanning and manual segmentation in determining drusen volume in age-related macular degeneration," *Retina*, vol. 30, no. 3, pp. 431–435, 2010.

Hindawi Publishing Corporation
Journal of Ophthalmology
Volume 2011, Article ID 285296, 5 pages
doi:10.1155/2011/285296

Case Report

Spectral Domain Optical Coherence Tomography in Diffuse Unilateral Subacute Neuroretinitis

Carlos Alexandre de A. Garcia Filho,[1,2] Ana Claudia Medeiros de A. G. Soares,[3] Fernando Marcondes Penha,[2] and Carlos Alexandre de Amorim Garcia[1]

[1] *Departamento de Oftalmología, Universidade Federal do Rio Grande do Norte, 59072-970 Natal, RN, Brazil*
[2] *Departamento de Oftalmología, Universidade Federal de São Paulo, 04021-001 São Paulo, SP, Brazil*
[3] *Departamento de Oftalmología, Santa Casa de Misericordia de São Paulo, 01221-020 São Paulo, SP, Brazil*

Correspondence should be addressed to Carlos Alexandre de A. Garcia Filho, caagf@yahoo.com.br

Received 28 February 2011; Accepted 20 June 2011

Academic Editor: Fernando M. Penha

Purpose. To describe the SD-OCT findings in patients with diffuse unilateral subacute neuroretinitis (DUSN) and evaluate CRT and RNFL thickness. *Methods*. Patients with clinical diagnosis of DUSN who were submitted to SD-OCT were included in the study. Complete ophthalmologic examination and SD-OCT were performed. Cirrus scan strategy protocols used were 200×200 macular cube, optic nerve head cube, and HD-5 line raster. *Results*. Eight patients with DUSN were included. Mean RNFL thickness was 80.25 μm and 104.75 μm for affected and normal eyes, respectively. Late stage had mean RNFL thickness of 74.83 μm compared to 96.5 μm in early stage. Mean CMT was 205.5 μm for affected eyes and 255.13 μm for normal fellow eyes. *Conclusion*. RNFL and CMT were thinner in DUSN eyes compared to normal eyes. Late-stage disease had more pronounced thinning compared to early-stage patients. This thinning in RNFL and CMT may reflect the low visual acuity in patients with DUSN.

1. Introduction

Diffuse unilateral subacute neuroretinitis (DUSN) is an inflammatory and infectious disease characterized by insidious and usually severe loss of peripheral and central vision [1]. Clinical features are manifested in early and late stages [1]. The acute phase is characterized by swelling of the optic disc, vitritis, and recurrent crops of evanescent, multifocal, white-yellowish lesions at the outer retina and choroid [2]. The chronic phase presents with optic nerve atrophy, narrowing of retinal vessels and focal or diffuse pigmentary changes [3]. Parasites of different sizes and several species of nematodes have been reported as the etiology of DUSN, including *Toxocara canis, Baylisascaris procyonis,* and *Ancylostoma caninum*, but most of these reports do not present conclusive evidence [4, 5].

Optical coherence tomography (OCT) is a noncontact, noninvasive diagnostic technique that allows measurement of central retinal thickness (CRT) retinal nerve fiber layer (RNFL) thickness and provides important information about the anatomy of the retina and choroid. The development of spectral domain OCT (SD OCT) considerably improved retinal imaging.

The purpose of this study is to describe SD-OCT findings in patients with DUSN and evaluate CRT and RNFL thickness with this image device.

2. Patients and Methods

This is a retrospective study in which a medical record review was performed at the Department of Ophthalmology, Federal University of Rio Grande do Norte, Brazil between January 2010 and January 2011. The study was approved by the institutional Review Board, and informed consent was obtained from all patients. Subjects with a diagnosis of DUSN were identified. Eyes included in the study had a minimum of 3 months followup. Patients had clinical diagnosis of DUSN based on Gass and Scelfo criteria, and both

Table 1: Clinical data of patients with DUSN and SD-OCT findings.

	Stage of disease	Age	Gender	Eye	RNFL thickness	RNFL fellow eye	CMT	CMT fellow eye	Foveal aspect	Initial VA	Final VA	Worm
Case 1	Early	14	Male	OS	87 μ	105 μ	201 μ	246 μ	No foveal depression	CF	20/60	Present
Case 2	Early	15	Male	OD	106 μ	112 μ	214 μ	249 μ	Normal foveal depression	20/200	20/25	Present
Case 3	Late	10	Female	OS	88 μ	113 μ	184 μ	259 μ	No foveal depression	CF	CF	Absent
Case 4	Late	25	Male	OD	67 μ	92 μ	217 μ	247 μ	No foveal depression	CF	CF	Absent
Case 5	Late	19	Male	OD	82 μ	102 μ	228 μ	253 μ	No foveal depression	20/200	20/60	Absent
Case 6	Late	17	Male	OS	87 μ	114 μ	256 μ	285 μ	Normal foveal depression	HM	HM	Absent
Case 7	Late	23	Male	OS	49 μ	100 μ	163 μ	253 μ	No foveal depression	CF	CF	Present
Case 8	Late	13	Male	OD	76 μ	100 μ	181 μ	249 μ	No foveal depression	CF	CF	Absent
Mean	NA	17	NA	NA	80.250 μ	104.75 μ	205.5 μ	255.13 μ	NA	NA	NA	NA

RNFL: retinal nerve fiber layer.
CMT: central macular thickness.
CF: counting fingers.
HM: hand motion.
NA: not applicable.

early-stage and late-disease patients who underwent SD-OCT (Carl Zeiss Meditec, Dublin, Calif) were included. Any other ocular disease was considered exclusion criteria.

All patients were submitted to complete ophthalmologic examination, including best corrected visual acuity (BCVA), slit lamp examination, tonometry, fundoscopy, and optical coherence tomography with cirrus. Strategy protocols used to obtain images were macular cube 200×200 for the central retinal thickness map, optic nerve head cube for retinal nerve fiber layer (RNFL) analysis, and HD-5 line raster to observe macular and foveal aspects.

The following data were collected and recorded: age, sex, initial and final best correct visual acuity (BCVA), affected eye, disease stage, and presence of the worm. Statistical analysis was performed using *Paired Student's t-test*.

3. Results

A total of 8 patients with clinical diagnosis of DUSN were included in the study. Mean age of affected patients was 17 years (13–25 yr). Out of 8 patients, 7 were male. Late-stage disease was found in 6 patients. The subretinal worm was identified in only 3 patients, 2 were in early-stage disease and 1 in the chronic stage. All patients in whom the worm was identified were treated with photocoagulation to destroy it.

Table 1 summarizes clinical and OCT findings for all patients included in the study.

Mean RNFL thickness of the affected eyes was 80.25 μm compared to 104.75 μm in the normal contralateral eyes ($P = 0.0005$). There was a difference in RNFL thickness measurements when the early-stage disease (mean RNFL thickness = 96.5 μm) was compared to late-stage disease (mean RNFL thickness = 74.83 μm).

Central macular thickness was assessed using macular cube strategy. Mean central macular thickness of affected eyes was 205.5 μm compared to 255.13 μm in the normal contralateral eyes ($P = 0.0004$). Macular thickness was similar in early- and late-stage disease (207.5 μm and 204.8 μm, resp.).

With respect to foveal anatomy, 6 out of 8 patients had alterations in foveal contour with a loss of foveal depression, despite diminished central retinal thickness. Neither the early- or late-stage disease patients presented focal or diffuse defects at the junction of the inner and outer segments of photoreceptors (IS/OS junction).

3.1. Cases Report. Case 1 is a 14-year-old male patient in early-stage disease with a 15-day history of low visual acuity in his left eye. Visual acuity was 20/20 in the right eye and counting fingers in the left eye. Biomicroscopy revealed mild vitritis. Fundus examination revealed multifocal, evanescent, white-yellowish lesions near the superior temporal arcade and the presence of a subretinal worm adjacent to the lesions. The worm was destroyed using photocoagulation and visual acuity improved to 20/60. Figure 1 illustrates SD-OCT findings for this patient. Figure 1(a) shows abnormal foveal architecture with a thinning in central macular thickness (201 μ compared to 246 μ in the fellow eye). Figure 1(b)

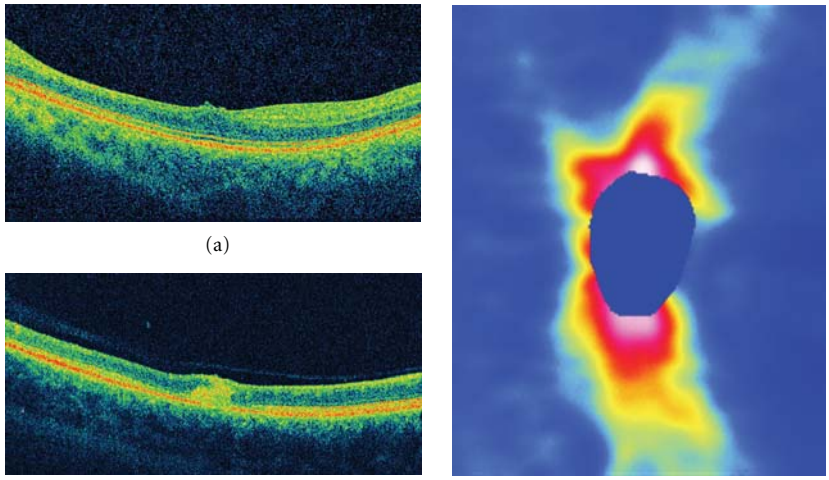

(a)

(b) (c)

Figure 1: (a) Abnormal foveal architecture in a patient with early-stage DUSN. (b) B-scan in the area the worm was located showing an increased intraretinal reflectivity corresponding to the worm and the surrounded inflammatory reaction. (c) RNFL map with a diffuse thinning.

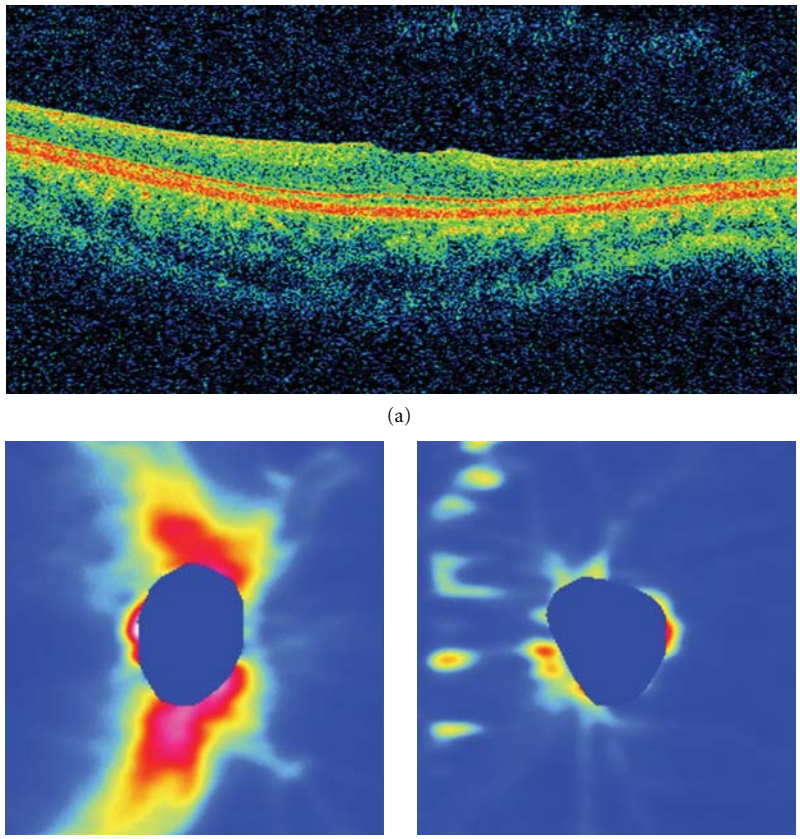

(a)

(b) (c)

Figure 2: (a) B-scan in the foveal area in a patient with late-stage DUSN presenting a reduced macular thickness and loss of normal foveal contour. RNFL thickness map in the normal eye (b) and a diffuse and pronounced RNFL thinning in the affected eye (c).

shows increased intraretinal hyperreflectivity in the area in which the subretinal worm was located. Figure 1(c) shows the RNFL map with a diffuse thinning. Average thickness is 87 μ compared to 105 μ in the normal fellow eye.

Case 7 is a 23-year-old male patient in late-stage DUSN who presented with a 6-month history of low visual acuity. Initial visual acuity was 20/20 in the right eye and counting finger in the left. Fundus examination revealed optic nerve pallor, narrowing of vessels, and diffuse pigmentary changes. The subretinal worm was identified in the nasal retina, and prompt laser photocoagulation was performed. Despite treatment, visual acuity remained counting fingers 90 days after treatment. SD-OCT features for this patient are presented in Figure 2. Figure 2(a) shows the B-scan in the foveal area, with reduced macular thickness and loss of normal foveal contour. Figures 2(b) and 2(c) illustrates the RNFL map in the normal eye and a diffuse and pronounced RNFL thinning in the affected eye.

4. Discussion

DUSN is an infectious disease caused by a subretinal nematode leading to inflammation and degeneration of the retina and retinal pigment epithelium. The pathogenesis of DUSN appears to involve a local toxic tissue effect on the outer retina caused by products released by the worm and a diffuse toxic reaction involving inner and outer retinal layers [1].

This toxic reaction resulting in inflammation may lead to retinal, RNFL, and optic nerve damage. Previous studies reported a reduction in RNFL thickness in patients with late-stage DUSN using the GDx nerve fiber analyzer [6] and Stratus OCT [7, 8]. In a study with 38 patients diagnosed with late-stage DUSN, Gomes et al. reported a significant decrease in RNFL thickness and a correlation with the low visual acuity presented by these patients [7]. Casella et al. reported the presence of RNFL atrophy even in patients with good visual acuity [8]. Cunha et al. reported an intraretinal worm using a Stratus OCT [9].

The ability of SD-OCT to acquire high-speed (at least 20,000 A-scans per second, compared to 400 A-scans per second for the tome domain OCT), high-resolution (axial resolution of 5 μ, compared to 10 μ in the Stratus OCT), and high-density three-dimensional images of the macula allows the capture of real retinal geometry that is less affected by eye movements. The high-density, averaged B-scans can be used to evaluate subtle changes in the retinal anatomy [10].

In our study, we assessed RNFL thickness in both early- and late-stage DUSN with SD-OCT. All patients in late stage disease presented with a significant decrease in RNFL thickness, and this correlates with the low visual acuity found in these patients (Table 1). All patients in early stage improved visual acuity after treatment. Case 1 improved from counting fingers to 20/60, while patient 2 achieved final visual acuity of 20/25. RNFL was reduced in patient 1 and normal in patient 2. SD-OCT retinal nerve fiber layer map also correlates with retinal thinning (Figures 2(b) and 2(c)). There seems to be a difference between RNFL thickness values between early- and late-stage disease, but as the number of patients in early-stage disease was small, it was not possible to perform statistical analysis.

Central macular thickness was also assessed in this case series. All patients, including early- and late-stage disease, presented with thinning in the central macular area measurement compared to the normal fellow eye. Early- and late-stage disease had similar values in CMT. Foveal appearance was abnormal in 6 patients. There was thinning in CMT, and the foveal depression was absent.

The worm was identified in only 3 patients (2 in early stage and 1 in late stage), but we were able to perform scans over the area in which the worm was located in only 1 patient. The precise location of the worm could not be identified, but intraretinal hyperreflectivity can be seen in Figure 1(b). This may correspond to the worm and surrounded inflammation caused by its presence.

Despite the small number of cases, the study showed clear changes in RNFL and macular thickness caused by the releases of worm toxins.

Although SD-OCT may help in identifying RNFL and CMT thinning in patients with DUSN and that these findings correlate with disease stage and visual acuity in these patients, the diagnosis of this condition is still based on the clinical features.

References

[1] J. D. M. Gass and R. A. Braunstein, "Further observations concerning the diffuse unilateral subacute neuroretinitis syndrome," *Archives of Ophthalmology*, vol. 101, no. 11, pp. 1689–1697, 1983.

[2] C. A. de A. Garcia, A. H. B. Gomes, C. A. de A. Garcia Filho, and R. N. G. Vianna, "Early-stage diffuse unilateral subacute neuroretinitis: improvement of vision after photocoagulation of the worm," *Eye*, vol. 18, no. 6, pp. 624–627, 2004.

[3] C. A. A. Garcia, A. H. B. Gomes, R. N. G. Vianna, J. P. S. Filho, C. A. A. G. Filho, and F. Oréfice, "Late-stage diffuse unilateral subacute neuroretinitis: photocoagulation of the worm does not improve the visual acuity of affected patients," *International Ophthalmology*, vol. 26, no. 1-2, pp. 39–42, 2005.

[4] M. A. Goldberg, K. R. Kazacos, W. M. Boyce, E. Ai, and B. Katz, "Diffuse unilateral subacute neuroretinitis: morphometric, serologic, and epidemiologic support for Baylisascaris as a causative agent," *Ophthalmology*, vol. 100, no. 11, pp. 1695–1701, 1993.

[5] J. D. M. Gass, "Diffuse unilateral subacute neuroretinitis," in *Stereoscopic Atlas of Macular Disease: Diagnosis and Treatment*, J. D. M. Gass, Ed., pp. 622–628, Mosby-Year Book Inc, St Louis, Mo, USA, 4th edition, 1997.

[6] C. A. de Amorim Garcia, A. G. F. de Oliveira, C. E. N. de Lima, F. N. Rocha, and C. A. de Amorim Garcia Filho, "Retinal nerve fiber layer analysis using GDx® in 49 patients with chronic phase DUSN," *Arquivos Brasileiros de Oftalmologia*, vol. 69, no. 5, pp. 631–635, 2006.

[7] A. H. Gomes, C. A. de Amorim Garcia, P. de Souza Segundo, C. A. de Amorim Garcia Filho, and A. C. de Amorim Garcia, "Optic coherence tomography in a patient with diffuse unilateral subacute neuroretinitis," *Arquivos Brasileiros de Oftalmologia*, vol. 72, no. 2, pp. 185–188, 2009.

[8] A. M. B. Casella, M. E. Farah, E. C. de Souza, R. Belfort, and A. P. Miyagusko Taba Oguido, "Retinal nerve fiber layer atrophy as relevant feature for diffuse unilateral subacute neuroretinitis (DUSN): case series," *Arquivos Brasileiros de Oftalmologia*, vol. 73, no. 2, pp. 182–185, 2010.

[9] L. P. Cunha, L. V. F. Costa-Cunha, E. C. de Souza, and M. L. R. Monteiro, "Intraretinal worm documented by optical coherence tomography in a patient with diffuse unilateral subacute neuroretinitis: case report," *Arquivos Brasileiros de Oftalmologia*, vol. 73, no. 5, pp. 462–463, 2010.

[10] M. Wojtkowski, V. Srinivasan, J. G. Fujimoto et al., "Three-dimensional retinal imaging with high-speed ultrahigh-resolution optical coherence tomography," *Ophthalmology*, vol. 112, no. 10, pp. 1734–1746, 2005.

Hindawi Publishing Corporation
Journal of Ophthalmology
Volume 2011, Article ID 706849, 4 pages
doi:10.1155/2011/706849

Research Article

Fundus Autofluorescence and Spectral Domain OCT in Central Serous Chorioretinopathy

Luiz Roisman, Daniel Lavinsky, Fernanda Magalhaes, Fabio Bom Aggio, Nilva Moraes, Jose A. Cardillo, and Michel E. Farah

Department of Ophthalmology, Federal University of São Paulo, Paulista School of Medicine, 04025-011 São Paulo, SP, Brazil

Correspondence should be addressed to Luiz Roisman, luizroi@yahoo.com.br

Received 28 November 2010; Accepted 20 June 2011

Academic Editor: Fernando M. Penha

Background. To describe the standard autofluorescence (FAF), the near infrared autofluorescence (NIA) and optical coherence tomography (OCT) patterns in central serous chorioretinopathy, correlating them with fluorescein angiography. *Methods*. Cross-sectional observational study, in which patients with at least seven months of CSC underwent ophthalmologic examination, fundus photography, FAF, NIA, fluorescein angiography (FA), and spectral-domain OCT. *Results*. Seventeen eyes of thirteen patients were included. The presentation features were a mottled hyperFAF in the detached area and areas with pigment mottling. NIA images showed areas of hyperNIA similar to FAF and localized areas of hypoNIA, which correlated with the points of leakage in the FA. OCT showed pigment epithelium detachment at the location of these hypoNIA spots. *Discussion*. FAF showed increased presence of fluorophores in the area of retinal detachment, which is believed to appear secondary to lipofuscin accumulation in the RPE or the presence of debris in the subretinal fluid. NIA has been related to the choroidal melanin content and there were areas of both increased and decreased NIA, which could be explained by damage ahead the retina, basically RPE and choroid. These findings, along with the PEDs found in the areas of hypoNIA, support the notion of a primary choroidal disease in CSC.

1. Introduction

Central serous chorioretinopathy (CSC) is an idiopathic syndrome of young to middle-aged adults, characterized by serous detachment of the neurosensory retina with focal and multifocal areas of leakage at the level of the retinal pigment epithelium (RPE), predominantly affecting the macular area [1]. Patients often complain of blurred central vision, micropsia, and metamorphopsia [2]. This idiopathic syndrome has been associated with systemic corticosteroid therapy [3] and emotional distress [4]. In most cases, CSC resolves spontaneously within six months, with good visual prognosis [5]. Prolonged and recurrent macular detachment in some cases, however, may cause degenerative changes in the subfoveal RPE and neurosensory retina with poor visual outcome [6].

The understanding of the physiopathology of CSC remains limited due to the lack of significant histopathologic studies. Investigational and diagnostic tools such as fluorescein and indocyanine green angiography have provided some insight into the mechanism of this disease [7]. Optical coherence tomography (OCT) has provided additional data about central macular detachments [8], development of retinal atrophy, and the correlation with visual acuity in resolved central serous chorioretinopathy [9]. Fundus autofluorescence (FAF) photography (488 nm) provides functional images of the fundus by employing the stimulated emission of light from endogenous fluorophores, the most significant being lipofuscin. In the case of RPE cells, the buildup of lipofuscin is related in large part to the phagocytosis of damaged photoreceptor outer segments and altered molecules retained within lysosomes, which eventually become lipofuscin [10–12]. Moreover, near infrared fundus autofluorescence (NIA) imaging (787 nm) is able to study the RPE, the choriocapillaris, and choroid, by determining melanin fluorescence [13].

The purpose of this study was to describe NIA and SD-OCT findings in CSC, correlating them with fluorescein angiography (FA). To our knowledge, this is the first study that investigates the correlation between the clinical findings and different imaging modalities, specially with NIA.

Table 1

	FAF (%)			NIA(%)		
	hypoFAF	mixedFAF	hyperFAF	hypoNIA	mixedNIA	hyperNIA
Detached area ($N = 10$)	10	20	70	30	20	50
Leakage spot ($N = 13$)	23.1	×	76.9	92.3	×	7.7
Window defect area ($N = 8$)	12.5	12.5	75	62.5	32.5	0
Overall image ($N = 17$)	17.6	11.8	70.6	58.8	17.6	23.5
PED ($N = 22$)				63.6	×	36.4

2. Materials and Methods

This is a retrospective, cross-sectional study were patients with CSC were included from September 2008 to May 2009 at the Federal University of Sao Paulo. This study was conducted in accordance with the Declaration of Helsinki and was approved by the ethics committee of the Federal University of Sao Paulo. All patients had experienced symptoms for at least 7 months and none of them had previous treatment.

Each patient underwent ophthalmologic examination, color fundus photography, FAF and NIA imaging, fluorescein angiography (FA), and HRA Spectralis spectral-domain OCT (SD-OCT) (Heidelberg Engineering, Heidelberg, Germany). The OCT protocol used was volume in the SD-OCT. The volume size was individualized for each patient. FAF, NIA, and FA imaging were performed with the Heidelberg Retina Angiograph 2 system (HRA2, Heidelberg, Germany). FAF and NIA images were recorded at 488 nm, using a barrier filter for detection of emitted light above 500 nm, and 787 nm, respectively. At least 5 single AF images of 512×512 pixels were acquired with each method. Several images were aligned and a mean image was calculated after detection and correction of eye movements using image analysis software.

Abnormal AF was defined as either increased or decreased fundus AF in comparison with background fundus AF [13], and classified as either hyperautofluorescence, hypo-autofluorescence, or mixed autofluorescence (no clear predominance).

3. Results

We included 17 eyes of 13 patients, eight males, and five females, presenting CSC with a mean time of complaint of 12.7 months, ranging from 7 months to 2 years, with age ranging from 26 to 53 years (mean age of 39.3 years). Two individuals had history of using steroids, but had stopped the use for at least 6 months. Fifteen patients had a relapsing desease and two were in the first episode.

Fluorescein angiography showed in 8 (47%) eyes focal leakage, in 1 (5.9%) multifocal leakage, in 4 (23.5%) multiple window defect with diffuse leakage, and in 4 (23.5%) no leakage.

Ten eyes exhibited serous retinal detachment. Of those, 1 presented with multifocal leakage, 7 with focal leakage, and 2 with RPE changes and multiple windows defects. The detached area revealed hyperFAF in 7 (70%), mixedFAF in 2 (20%), and hypoFAF in 1 (10%). HypoNIA could be seen in 5 (50%), mixedNIA in 2 (20%), and hyperNIA in 3 (30%).

The areas of window defects seen at FA in 8 eyes showed hyperFAF in 6 (75%), mixedFAF and hypoFAF in 1 eye each (12.5%). Concerning NIA of the window defects areas, we could find 5 eyes indicating hypoNIA (62.5%) and 3 mixedNIA (37.5%).

The overall FAF images revealed hyperFAF in 12 (70.6%) eyes, hypoFAF in 3 (17.6%) eyes, and mixed FAF in 2 (11.8%) eyes. The overall NIA images presented hyperNIA in 4 (23.5%) eyes, hypoNIA in 10 (58.8%), and mixed NIA in 3 (17.6%) eyes. Twelve of thirteen eyes with leakage showed a hypoNIA exactly at the leaking spot. A hypoFAF was found in 3 eyes in the leakage site. The location of autofluorescence alterations were perimacular, following the leakage and the RPE damage sites (Table 1).

The Spectralis OCT images revealed 10 (58.8%) foveal neurosensory retinal detachment. The mean foveal retinal thickness was 332.6 μm, ranging from 220 to 533 μm. Pigment epithelium detachment (PED) in foveal and/or extrafoveal spots was identified in 11 of the 13 patients, in a total of 22 PEDs in 15 of 17 eyes. Twelve (54.5%) were foveals and ten extra foveals (45.4%). We could observe in 5 eyes a substantial RPE irregularity, characterized by RPE undulations, 2 of them without PED.

A hyperNIA spot in the NIA images could be seen in 8 (36.4%) of the PEDs and in 14 (63.6%) corresponding to hypoNIA sites. In 7 (31.8% of all PEDs) of the 14 PEDs that corresponded to hypoNIA images, we could identify a hyperNIA "ring." In 14 (63.6%) of the PEDs, we found that the PED corresponded exactly with the leakage spot detected in FA, and 7 (31.8%) PEDs corresponded to window defect areas in FA, while 1 (4.5%) PED did not correlate with FA alterations. The 14 PEDs that correlated with the point of leakage showed a hyperNIA point in 5 (35.7%) PEDs, hypoNIA with hyperNIA "ring" in 4 (28.6%), and hypoNIA without ring in 5 (35.7%) of the leakage PEDs (Figures 1, 2 and 3).

4. Discussion

NIA is not a common used modality of the HRA2, but its importance when studying the choroid and outer retina had been described before [13]. Recently, Kellner et al. suggests that NIA is a reliable method for RPE evaluation in AMD [14]. It can be very helpful for conditions such as CSC, in which the choroid appears to be primarily involved. In the present study, it was shown that the mostly hypofluorescent spots on NIA images corresponded to pigment epithelium detachments on OCT and to leakage points on fluorescein

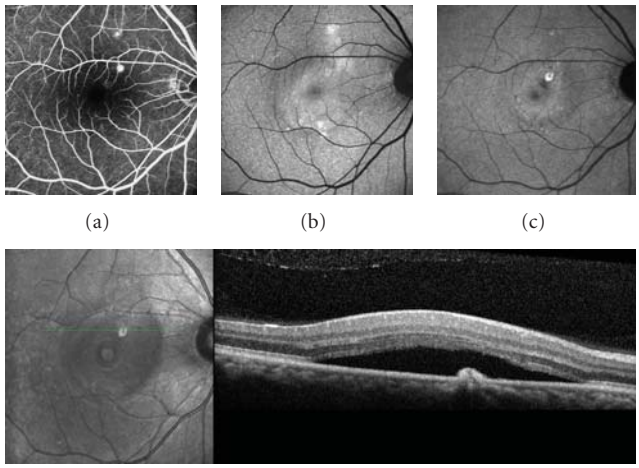

(a) (b) (c)

(d)

Figure 1: Patient with 12 months of history of CSC in the right eye. (a) Two dots spots of leakage in the angiography; (b) standard FAF, presenting with diffuse hyperFAF; (c) NIA, showing suprafoveal hypofluorescent point surrounded by a ring of hyperAF, corresponding exactly with the PEDs in (d); (d) SD-OCT exhibiting the PED and neurosensorial retinal detachment.

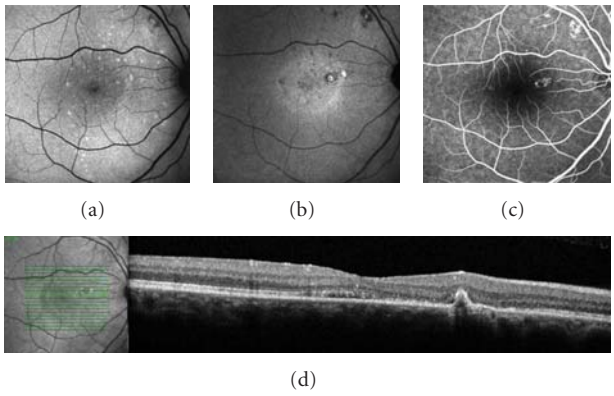

(a) (b) (c)

(d)

Figure 2: Patient with 9 months of history of CSC in the right eye. (a) Standard FAF, showing mottled hyperFAF spots; (b) NIA, presenting macular and supratemporal to the optic disk hypofluorescent points—the macular spot surrounded by a ring of hyperAF, corresponding exactly with the PED in (d); (c) spots of leakage in the angiography; (d) SD-OCT exhibiting the PED.

angiography. The hypoNIRAF spot could identify the leakage points in 12 (70.6%) of the eyes and the ring of hyperNIA around these hypofluorescent spots found in 31.8% of all PEDs could represent "pooling" of RPE cells because of the PEDs or local RPE folding, but further studies are needed to confirm this hypothesis.

The FAF images showed hyperFAF in the great majority of the cases, probably due to accumulation of lipofuscin and other fluorophores, as described by Spaide and Klancnik [7]. We found a much weaker correlation between a hypoFAF spot at the leakage site, as reported by Framme et al. [15],

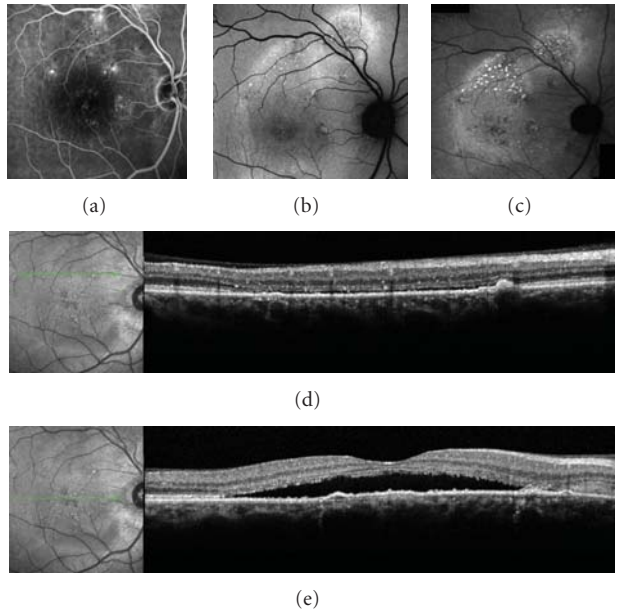

(a) (b) (c)

(d)

(e)

Figure 3: Patient with 18 months of history of CSC in the right eye. (a) dots spots of leakage in the angiography; (b) standard FAF, showing diffuse superior hyperFAF; (c) NIA, showing three hypofluorescent spots around the macula, some of them corresponding exactly with the PEDs in (d) and (e); (d) and (e) SD-OCT exhibiting the PEDs and neurosensorial retinal detachment.

detected only in 3 eyes, comparing to 12 eyes with a hypoNIA spot in the same situation.

Ayata et al. [16] had similar findings in acute CSC, also presenting hypoNIA corresponding to the area of the serous retinal detachment and to the leakage point. Interestingly, he also found hypoNIA spots that were not leaking on angiogram, hypothesizing that the pathological site of the chorioretinal disturbance could be more extensive than expected. We had the opportunity to correlate the NIA images to OCT, and the hipoNIA spots, corresponding or not to leaking points, presented a PED or RPE focal irregularity, sustaining a choroidal etiology for CSC.

Almost 60% of NIA examinations showed diffuse hypoNIA, although almost 25% displayed hyperNIA. These results may represent different stages of the disease. We did not observe the minute defect described by Fujimoto et al. [17] in any of the cases, although we confirmed the relation between the PED and the leakage site, seen in more than 63% of PEDs. The presence of leakage in the PEDs spots could help explain the CSC recurrence, the persistence of retinal detachment and symptoms in some cases, as the PEDs are active, in terms of leakage and lower RPE absorption.

One of the most interesting findings of this study, was the correlation of the PED in the SD-OCT with the hypoNIA spot and the point of leakage in the fluorescein angiography (FA). Almost 60% of PEDs corresponded to leaking sites that corresponded to hypoNIA areas, and twelve of thirteen eyes that showed leakage had a hypoNIA spot exactly at the leaking spot. Although FA is still an important exam for the management of CSC, these findings may be useful in

guiding the treatment, since OCT and NIA may provide the location of leakage points by means of a noninvasive, dye-free examination, providing safety and precision for the patient and the doctor, matching with the treatment safety pursuit, as we can expect from the subthreshold diode micropulse photocoagulation [18]. This is a retrospective, not controlled or randomized study, evaluating chronic CSC eyes. A larger sampled study, including acute cases, are warranted to confirm these preliminary results.

References

[1] M. Moschos, D. Brouzas, C. Koutsandrea et al., "Assessment of central serous chorioretinopathy by optical coherence tomography and multifocal electroretinography," *Ophthalmologica*, vol. 221, no. 5, pp. 292–298, 2007.

[2] D. M. Robertson, "Argon laser photocoagulation treatment in central serous chorioretinopathy," *Ophthalmology*, vol. 93, no. 7, pp. 972–974, 1986.

[3] G. Chaine, M. Haouat, C. Menard-Molcard et al., "Central serous chorioretinopathy and systemic steroid therapy," *Journal Francais d'Ophtalmologie*, vol. 24, no. 2, pp. 139–146, 2001.

[4] R. Conrad, N. F. Weber, M. Lehnert, F. G. Holz, R. Liedtke, and N. Eter, "Alexithymia and emotional distress in patients with central serous chorioretinopathy," *Psychosomatics*, vol. 48, no. 6, pp. 489–495, 2007.

[5] M. Wang, I. C. Munch, P. W. Hasler, C. Prünte, and M. Larsen, "Central serous chorioretinopathy," *Acta Ophthalmologica*, vol. 86, no. 2, pp. 126–145, 2008.

[6] A. E. Jalkh, N. Jabbour, and M. P. Avila, "Retinal pigment epithelium decompensation. I. Clinical features and natural course," *Ophthalmology*, vol. 91, no. 12, pp. 1544–1548, 1984.

[7] R. F. Spaide and J. M. Klancnik, "Fundus autofluorescence and central serous chorioretinopathy," *Ophthalmology*, vol. 112, no. 5, pp. 825–833, 2005.

[8] M. Wang, B. Sander, H. Lund-Andersen, and M. Larsen, "Detection of shallow detachments in central serous chorioretinopathy," *Acta Ophthalmologica Scandinavica*, vol. 77, no. 4, pp. 402–405, 1999.

[9] C. M. Eandi, J. E. Chung, F. Cardillo-Piccolino, and R. F. Spaide, "Optical coherence tomography in unilateral resolved central serous chorioretinopathy," *Retina*, vol. 25, no. 4, pp. 417–421, 2005.

[10] F. C. Delori, C. K. Dorey, G. Staurenghi, O. Arend, D. G. Goger, and J. J. Weiter, "In vivo fluorescence of the ocular fundus exhibits retinal pigment epithelium lipofuscin characteristics," *Investigative Ophthalmology and Visual Science*, vol. 36, no. 3, pp. 718–729, 1995.

[11] A. Von Ruckmann, F. W. Fitzke, and A. C. Bird, "Distribution of fundus autofluorescence with a scanning laser ophthalmoscope," *British Journal of Ophthalmology*, vol. 79, no. 5, pp. 407–412, 1995.

[12] G. E. Eldred and M. L. Katz, "Fluorophores of the human retinal pigment epithelium: separation and spectral characterization," *Experimental Eye Research*, vol. 47, no. 1, pp. 71–86, 1988.

[13] C. N. Keilhauer and F. C. Delori, "Near-infrared autofluorescence imaging of the fundus: visualization of ocular melanin," *Investigative Ophthalmology and Visual Science*, vol. 47, no. 8, pp. 3556–3564, 2006.

[14] U. Kellner, S. Kellner, and S. Weinitz, "Fundus autofluorescence (488 nm) and near-infrared utofluorescence (787 nm) visualize different retinal pigment epithelium alterations in patients with age-related macular degeneration," *Retina*, vol. 30, no. 1, pp. 6–15, 2010.

[15] C. Framme, A. Walter, B. Gabler, J. Roider, H. G. Sachs, and V. P. Gabel, "Fundus autofluorescence in acute and chronic-recurrent central serous chorioretinopathy," *Acta Ophthalmologica Scandinavica*, vol. 83, no. 2, pp. 161–167, 2005.

[16] A. Ayata, S. Tatlipinar, T. Kar, M. Unal, D. Ersanli, and A. H. Bilge, "Near-infrared and short-wavelength autofluorescence imaging in central serous chorioretinopathy," *British Journal of Ophthalmology*, vol. 93, no. 1, pp. 79–82, 2009.

[17] H. Fujimoto, F. Gomi, T. Wakabayashi, M. Sawa, M. Tsujikawa, and Y. Tano, "Morphologic changes in acute central serous chorioretinopathy evaluated by Fourier-Domain optical coherence tomography," *Ophthalmology*, vol. 115, no. 9, pp. 1494–1500, 2008.

[18] S. N. Chen, J. F. Hwang, L. F. Tseng, and C. J. Lin, "Subthreshold diode micropulse photocoagulation for the treatment of chronic central serous chorioretinopathy with juxtafoveal leakage," *Ophthalmology*, vol. 115, no. 12, pp. 2229–2234, 2008.

Hindawi Publishing Corporation
Journal of Ophthalmology
Volume 2011, Article ID 385058, 12 pages
doi:10.1155/2011/385058

Review Article

Optical Coherence Tomography of Retinal and Choroidal Tumors

Emil Anthony T. Say, Sanket U. Shah, Sandor Ferenczy, and Carol L. Shields

Oncology Service, Wills Eye Institute, Thomas Jefferson University, Suite 1440, 840 Walnut Street, Philadelphia, PA 19107, USA

Correspondence should be addressed to Carol L. Shields, carol.shields@shieldsoncology.com

Received 16 February 2011; Accepted 7 May 2011

Academic Editor: Eduardo Buchele Rodrigues

Optical coherence tomography (OCT) has revolutionized the field of ophthalmology since its introduction 20 years ago. Originally intended primarily for retina specialists to image the macula, it has found its role in other subspecialties that include glaucoma, cornea, and ocular oncology. In ocular oncology, OCT provides axial resolution to approximately 7 microns with cross-sectional images of the retina, delivering valuable information on the effects of intraocular tumors on the retinal architecture. Some effects include retinal edema, subretinal fluid, retinal atrophy, photoreceptor loss, outer retinal thinning, and retinal pigment epithelial detachment. With more advanced technology, OCT now provides imaging deeper into the choroid using a technique called enhanced depth imaging. This allows characterization of the thickness and reflective quality of small (<3 mm thick) choroidal lesions including choroidal nevus and melanoma. Future improvements in image resolution and depth will allow better understanding of the mechanisms of visual loss, tumor growth, and tumor management.

1. Introduction

Since its inception in 1991, optical coherence tomography (OCT) has found wide applications in medicine including gastroenterology, dermatology, cardiology, and ophthalmology [1–4]. Traditional time domain OCT, sold commercially in 1995 and used primarily by retina and glaucoma specialists, has been largely replaced by Spectral or Fourier domain OCT that provides higher resolution images (4–7 um) and faster scanning speeds (up to 40,000 scans per second) that could translate to broader application of OCT for other ophthalmic subspecialties including pediatric ophthalmology, oculoplastics, and ocular oncology [5–8].

OCT is a valuable diagnostic tool for evaluation of tissue architecture of the postequatorial fundus (inner retina, outer retina, retinal pigment epithelium (RPE), and choroid). In ocular oncology, OCT allows for diagnosis, treatment planning, and monitoring response. Traditionally, OCT was primarily used to image the neurosensory retina and the retinal pigment epithelium (RPE) with outstanding resolution, but the choroid and sclera have been poorly imaged. Today, software upgrades and new imaging techniques allow longer scan lengths, enhanced depth imaging (EDI), and three-dimensional reconstruction. These newer features allow demonstration of more peripheral tumors, higher resolution images of anatomy deep to the retina, and improved characterization of intraocular tumors [8–10]. Herein we review clinical features of posterior segment intraocular tumors on OCT and its applications in the management of these lesions.

2. Choroidal Nevus

Choroidal nevi are the most common intraocular tumor. Population studies show higher prevalence of these tumors in Caucasians (6.5%) compared to Asians (1.4%) [11]. Nevi are typically pigmented, with smooth margins and with overlying drusen, measuring less than 5 mm in basal diameter and 3 mm in thickness. They often do not cause visual symptoms and more importantly are generally benign. It has been estimated, however, that 1 in 8845 choroidal nevi undergoes malignant transformation into melanoma [12]. Although the odds appear minimal, careful evaluation and followup of all choroidal nevi is advised. Factors predictive of nevus transformation into melanoma include thickness greater than 2 mm, the presence of subretinal fluid, orange

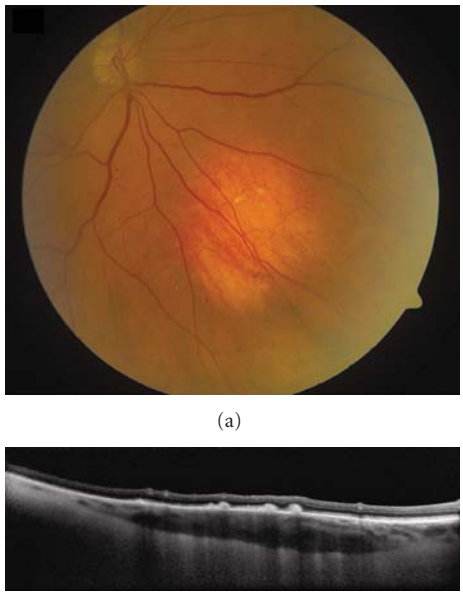

(a)

(b)

Figure 1: Choroidal nevus. (a) Amelanotic choroidal nevus with overlying RPE alterations and areas of RPE atrophy. (b) EDI OCT image shows both anterior and posterior margins of the lesion. There is gradual transition between the hyperreflective inner choroid and hyporeflective outer choroid. There is loss of choriocapillaris over the main lesion. Multifocal excrescences of the RPE are also present, suggestive of drusen.

pigment, juxtapapillary location, and symptoms of blurred vision or photopsia [13]. The presence of any one factor gives a relative risk of 1.9, three factors 7.4, and the presence of all five will give a relative risk of 27.1 [14].

OCT features of choroidal nevus have been extensively documented but are limited mostly to its effects on the overlying retina and the anterior choroidal surface [8]. Shields and associates compared the frequency of retinal findings by clinical examination to OCT [15]. They found that OCT has a higher sensitivity than clinical examination in detection of overlying retinal edema (15% by OCT versus 3% by clinical examination), subretinal fluid (26% versus 16%), retinal thinning (22% versus 0%), and RPE detachment (12% versus 2%) [15]. OCT also enabled the examiners to characterize retinal edema (cystoid versus noncystoid) and determine the status of overlying photoreceptors [15]. These features are significant, since foveal edema and RPE detachment were found to be predictive of 3 or more lines of vision loss (RR = 22.16 and 9.02, resp.) and a final visual outcome worse than 20/200 (RR = 12.80 and 18.72, resp.) [16]. Overlying photoreceptor loss can also explain associated visual field defects in some patients. Findings localized to the RPE are also visualized readily by OCT. OCT evidence of overlying drusen manifests as small dome-shaped elevations at the level of the RPE/Bruch's membrane [15] (Figure 1). Nevus-related drusen are found in 41% of choroidal nevi imaged by OCT and are also visualized by ophthalmoscopy [15].

On OCT, the choroidal findings in nevi are limited to the anterior surface and include hyporeflectivity in 62%, isoreflectivity in 29%, and hyperreflectivity in 9% [15]. Anterior choroidal reflectivity is affected by overlying RPE alterations and the amount of pigmentation [15]. The OCT findings reflect pigment within the mass and do not correlate to internal reflectivity and acoustic quality by ultrasonography, which imply density of cellularity [15].

3. Choroidal Melanoma

Uveal melanoma is the most common primary intraocular malignancy, and 90% develop in the choroid [17]. They often present as a pigmented, elevated, choroidal mass with associated orange pigment and subretinal fluid. Most choroidal melanomas can be differentiated from benign nevi because melanoma is much larger in size. However, approximately 30% of choroidal melanomas are small ($\leq$3 mm thickness) and difficult to differentiate from nevi by clinical examination alone [17]. In these cases, OCT can be helpful in the detection of melanoma-related features in the overlying retina such as subretinal fluid [15]. Subretinal fluid associated with melanoma shift with positioning and may cause intermittent blurred vision or flashes. Overall, 15% and 25% of uveal melanomas metastasize in 5 and 10 years [17]. Shields and associates found subretinal fluid to be a significant risk for metastasis in 8033 cases of uveal melanoma, so detection of even subtle subretinal fluid by OCT could be vital to patient prognosis [17].

Subretinal fluid is an important characteristic related to underlying choroidal melanoma. Muscat and coworkers studied 20 untreated choroidal melanoma and detected subretinal fluid using time domain OCT in all cases [18]. Espinoza and colleagues also used time domain OCT to describe an active OCT pattern, wherein a localized serous retinal detachment was associated with an overlying retina of normal thickness, a feature that was highly associated with documented tumor growth ($P = 0.033$) and future treatment ($P = 0.014$) [19]. In contrast, a chronic OCT pattern, wherein the overlying retina was thinned, contains intraretinal cysts and with RPE thickening was associated with a long-standing lesion more likely to remain dormant [19]. Sayanagi and coworkers used 3D spectral domain OCT and found a significantly higher prevalence of subretinal fluid (91% versus 14%), retinal edema (61% versus 14%), and subretinal deposits (61% versus 11%) in choroidal melanoma compared with nevi [10]. Singh and associates used spectral domain OCT to describe dispersed accumulation of subretinal deposits corresponding to orange pigment over a small choroidal melanoma that had not been found with time domain OCT [20]. Spectral domain OCT was also capable of detecting early vitreous seeding as highly reflective 20–30 micron spheroidal bodies in the vitreous [21]. The limitation of OCT for choroidal melanoma lies in the difficulty of imaging the overlying retina for large melanomas and the inability to image past the anterior choroidal surface [19]. Reflectivity of the anterior choroid in melanoma is variable even with spectral domain OCT [20] (Figure 2).

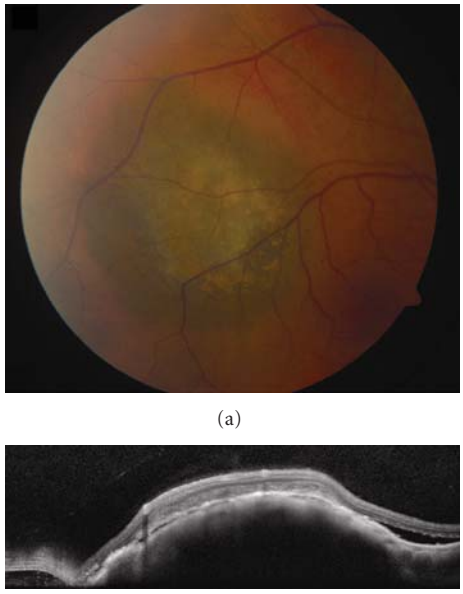

(a)

(b)

Figure 2: Choroidal melanoma. (a) Small choroidal melanoma with overlying RPE hyperplasia and diffuse orange pigment accumulation. (b) Spectral domain OCT clearly demonstrates subretinal fluid that could have been missed by clinical examination alone. Overlying the dome-shaped elevation of the choroid is a thickened irregular RPE and thickening of the outer retinal layers.

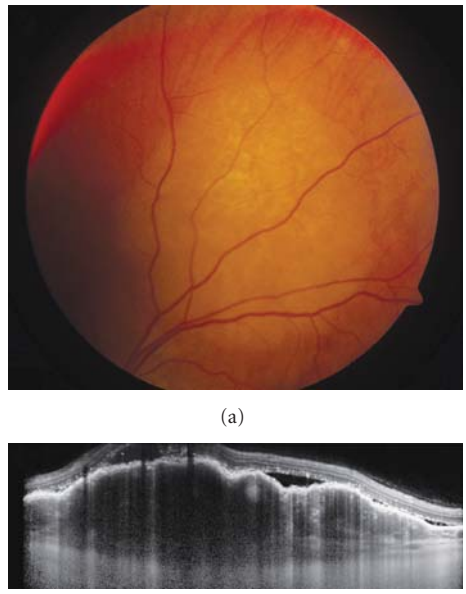

(a)

(b)

Figure 3: Choroidal metastasis. (a) Amelanotic choroidal metastasis in a patient with breast cancer. (b) EDI OCT reveals both the anterior and posterior margins of the metastasis allowing measurement of tumor thickness and characterization of its internal structure. Multiple nodular elevations of the RPE can also be seen with thickening of the RPE, overlying subretinal fluid, and hyperreflective deposits within the neurosensory detachments presumably from tumor cells or macrophages.

In addition to examination of the overlying retina and RPE, OCT has been used to monitor treatment response and complications following radiotherapy for choroidal melanoma. Horgan and associates performed pre- and postplaque radiotherapy OCT and found that the mean time to onset of radiation maculopathy was 12 months [22]. The authors also reported that 17% had macular edema by OCT at 6 months, 40% at 12 months, and 61% at 24 months [22]. In comparison, radiation maculopathy was detected by clinical examination alone 1% by 6 months, 12% at 12 months, and 29% at 24 months [22]. Further, OCT enabled the authors to classify macular edema into extrafoveolar noncystoid (grade 1), extrafoveolar cystoid (grade 2), foveolar noncystoid (grade 3), mild-moderate foveolar cystoid (grade 4), and severe foveolar cystoid (grade 5) [22]. This qualitative classification correlated with quantification of central foveolar thickness. In such cases, both OCT and visual acuity can be used to monitor treatment response following laser photocoagulation, intravitreal anti-VEGF, and intravitreal triamcinolone for radiation macular edema.

4. Choroidal Metastasis

The choroid is the most common site of metastasis in the eye because of its vascularity. Patients usually present with painless blurring of vision, and 66% will have a prior history of systemic cancer, most commonly the breast in women and the lungs in men [23]. Among the 34% without a history of systemic cancer, the lung is the most common primary site after workup [23]. Clinically, choroidal metastasis appears as a solitary, nonpigmented choroidal mass with associated shifting subretinal fluid [23]. They can occasionally be associated with overlying RPE alterations and brown pigment accumulation corresponding to lipofuscin.

OCT of choroidal metastasis demonstrates a dome-shaped elevation of the neurosensory retina and RPE with adjacent subretinal fluid (Figure 3). It can also be associated with retinal edema, intraretinal cysts, and thickening and detachment of the RPE. Natesh and associates found highly reflective subretinal deposits corresponding to RPE clumping overlying the tumor on clinical examination [24]. Arevalo and colleagues also found highly reflective points within neurosensory detachment in 14.2% of cases and concluded that these points "may correspond to retinal compromise by cancer cells or macrophages containing lipofuscin and melanin granules" [25]. Choroidal features are also limited to the anterior surface as with all choroidal tumors, and they often have variable reflectivity [10]. In addition to its diagnostic capabilities, OCT is valuable in monitoring treatment response, since resolution of subretinal fluid and return of normal retinal architecture has been documented following therapy [25, 26].

5. Choroidal Hemangioma

Choroidal hemangiomas are benign vascular tumors that are either circumscribed or diffuse based on the extent

of choroidal involvement [27]. Circumscribed choroidal hemangioma is usually orange colored, round, located in the posterior pole, and exhibits overlying retinal edema, subretinal fluid, and RPE alterations [28]. Choroidal hemangioma shows high internal reflectivity and acoustic solidity on ultrasonography, while often demonstrating a bright early filling and a characteristic late "wash out" on indocyanine green angiography [28]. On MRI, it is hyperintense to vitreous on T1, and isointense on T2, unlike most intraocular tumors, which are hypointense on T2 [28]. The diffuse variant usually extends to involve the entire choroid and is often associated with an ipsilateral facial hemangioma (nevus flammeus) that together comprise the Sturge-Weber syndrome [27, 28].

Ramasubramanian and colleagues described OCT findings in circumscribed choroidal hemangioma and found subretinal fluid (19%), retinal edema (42%), retinal schisis (12%), macular edema (24%), and localized photoreceptor loss (35%) [29]. The same group also described OCT findings in diffuse choroidal hemangioma and reported subretinal fluid (28%), retinal edema (14%), and photoreceptor loss (43%) [29]. Acute leakage from choroidal hemangioma demonstrates subretinal fluid with preserved photoreceptor layer and normal retinal thickness, whereas chronic leakage displays loss of photoreceptors, retinoschisis, and intraretinal edema associated with subretinal fluid [8] (Figure 4). By OCT, the anterior tumor surface is hyporeflective [10]. Currently, OCT has been used to monitor response to treatment by photodynamic therapy, transpupillary thermotherapy, plaque radiation, or laser photocoagulation. Blasi and associates performed photodynamic therapy on 25 cases of circumscribed choroidal hemangioma and reported a decrease in central foveal thickness and restoration of foveal anatomy following treatment after 5 years [30].

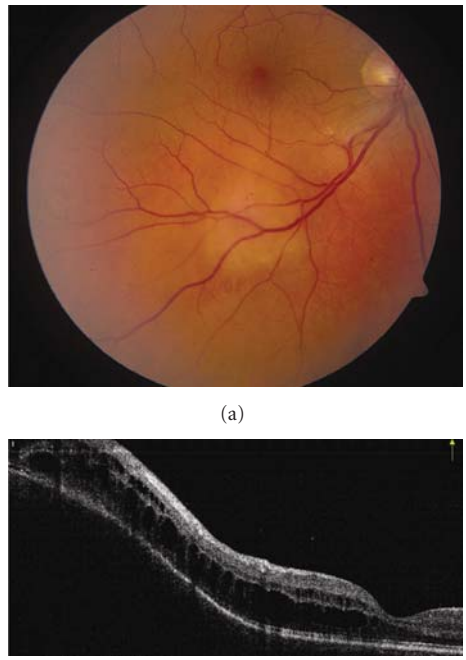

(a)

(b)

Figure 4: Choroidal hemangioma. (a) Choroidal hemangioma along inferotemporal arcade with subtle exudation seen inferonasal and inferotemporal to the foveola. (b) Time domain OCT shows dome-shaped elevation of its posterior border with overlying retinoschisis and retinal edema.

6. Choroidal Osteoma

Choroidal osteoma is a rare, osseous tumor often found in young females. This tumor appears as an orange-yellow plaque in the juxtapapillary region or macula but can demonstrate areas of whitening when decalcified. This tumor is benign but has the capacity to grow. Long-term studies have shown growth rates of 41–51%, choroidal neovascularization in 31–47%, and final visual outcome worse than 20/200 in 56–58% after 10 years [31, 32]. The mechanisms of visual loss include subretinal fluid, choroidal neovascularization, and photoreceptor loss. Shields and colleagues followed 74 eyes with choroidal osteoma to find subretinal fluid and tumor decalcification as factors predictive of poor visual outcome or loss of 3 or more lines of vision [32].

The internal structure of choroidal osteoma is difficult to evaluate with OCT and is limited to its anterior surface [8]. The overlying inner retina is often preserved while changes in the outer retinal layers, namely, the photoreceptors and the RPE, are often observed [8]. The RPE can sometimes be continuous with the inner surface of the underlying tumor, and the degree of calcification affects the amount of light transmission [8, 33, 34] (Figure 5). Shields and coworkers reported on the OCT features of choroidal osteoma and reported heterogeneity that largely depends on the amount of calcification [35]. Calcified portions of the tumor reveal mostly intact inner (100%) and outer (95%) retinal layers, a distinct RPE (57%), and mild transmission of light (95%) [35]. In contrast, decalcified portions of the tumor reveal intact inner retinal layers (90%), thinned outer retinal layers (100%), an indistinct RPE (90%), and marked light transmission into the tumor (70%) [35]. They also described focal areas of shadowing behind areas of RPE hyperplasia [35]. The anterior tumor surface was hyperreflective in 48% and isoreflective in 52% if calcified but was mostly hyperreflective (90%) when decalcified [35].

7. Lymphoid Tumors

Intraocular lymphoid tumors can occur in different parts of the eye with varying prognostic implications. There are two basic types, the vitreoretinal type and the uveal type. Vitreoretinal lymphoma accounts for most cases and are primarily diffuse large b-cell lymphomas [36]. They are aggressive tumors, highly associated with central nervous system lymphomas [36]. Patients are often elderly and immunocompetent or young and immunocompromised. Clinically, they present as bilateral multifocal yellowish deposits in the retina, subretina, or sub-RPE with overlying vitreous opacities. Pigment migration and RPE clumping can sometimes be visible overlying the tumor as brown leopard spots.

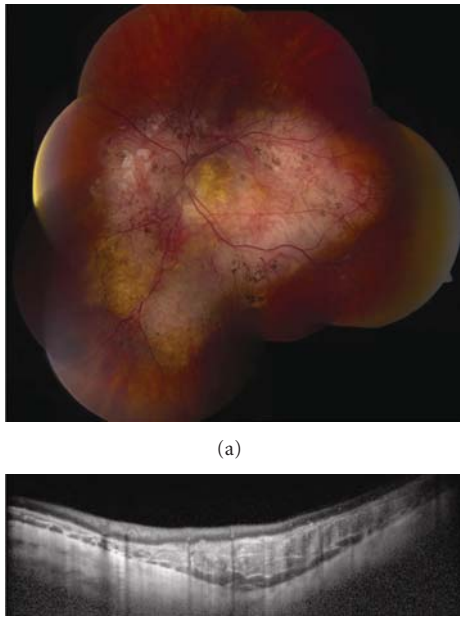

(a)

(b)

Figure 5: Choroidal osteoma. (a) Decalcified circumpapillary choroidal osteoma with associated pigment migration and RPE atrophy. (b) EDI OCT demonstrates replacement of the normal choriocapillaris with a dense hyperreflective mass with a scalloped posterior border and an adjacent hyporeflective space anterior to the sclera. The main lesion is almost continuous with the overlying RPE. Overlying neurosensory retina is thinned with the loss of the outer layers.

Uveal lymphoid tumors involve the choroid, ciliary body, and iris, often with conjunctival and orbital components. Most are extranodal marginal zone b-cell lymphoma although a benign reactive lymphoid hyperplasia subtype exists that presents similarly albeit less aggressive [36]. Choroidal lymphoid tumors are usually unilateral. They present as multifocal orange-yellow choroidal infiltrates resembling those from white dot syndromes [36]. In time, they can involve the entire uveal tract causing a diffuse thickening of the uvea on ultrasonography often with a small round echolucency behind the sclera [37]. The overlying retina and vitreous remain clear; however, the fornix or conjunctiva can be involved as "salmon patches" [36]. Compared to vitreoretinal lymphoma, uveal lymphomas are more indolent, but an association with systemic lymphoma exists.

Diagnosis of all intraocular lymphoid tumors should be done with a biopsy, either from an associated conjunctival or forniceal involvement or through vitrectomy and fine needle biopsy of the involved ocular tissue. Ancillary testing is not absolutely necessary although it can provide insight on the extent of involvement. OCT in vitreoretinal lymphomas may show dome-shaped elevations of the RPE or small nodular RPE irregularities from sub-RPE tumor deposits, retinal elevation or thickening from tumor infiltration, and cystoid macular edema from associated inflammatory reaction [38–40] (Figure 6). Fardeau and associates examined 61 eyes with vitreoretinal lymphoma confirmed through vitreous biopsies and found that 41.7% had nodular elevations of the RPE [40]. The authors also reported a significantly thinner central foveal thickness compared to eyes with posterior uveitis other than lymphoma [40]. OCT performed in choroidal lymphoma shows regular intermittent placoid choroidal thickening and loss of choriocapillaris [41]. The overlying RPE and neurosensory retina is unaffected and retains its regular, smooth contour [41].

8. Congenital Hypertrophy of the Retinal Pigment Epithelium

Congenital hypertrophy of the retinal pigment epithelium (CHRPE) is a benign, flat, and pigmented lesion rarely associated with vision loss or visual field defects. This tumor is often unilateral and solitary but can occasionally be multifocal or grouped in a bear-track distribution. Familial adenomatous polyposis and Gardner's syndrome have been associated with a variant, wherein lesions appear in a haphazard multifocal distribution, and individual CHRPE has irregular borders and an atrophic "tail." Shields and coworkers reported atrophic lacunae in 43% occupying a median 5% of the total area [42]. In their series of 330 patients with 337 lesions, growth in basal dimensions was documented by photographic comparison in 46%, while 5 (1.4%) lesions had a nodular elevation within CHRPE [42].

OCT imaging of CHRPE can be difficult due to its peripheral location but could potentially be better captured using longer scan lengths by new-generation spectral domain OCT. Shields and colleagues described overlying retinal thinning and photoreceptor loss in all patients with CHRPE that likely account for visual field defects [43]. The neurosensory retina overlying CHRPE was only 68% the thickness of adjacent normal retina [43]. Pigmented CHRPE has 52% thicker RPE than adjacent normal retina that prevents light transmission and shadows the underlying choroid [43]. Nonpigmented CHRPE, on the other hand, has large areas of lacunae with thinner RPE that allow transmission of light and partial visualization of the choroid [43] (Figure 7).

9. Combined Hamartoma of the Retina and Retinal Pigment Epithelium

A typical appearance of combined hamartoma of the retina and RPE is an elevated grey mass of the retina blending imperceptibly with surrounding retina and RPE without retinal detachment, or vitreous inflammation. There is often an associated preretinal fibrosis with traction on the adjacent retina. In a classic report by Schachat and associates from the Macula Society, vascular tortuosity was present in 93%, vitreoretinal surface abnormalities in 78%, pigmentation in 87%, and associated lipid exudation in 7% [44]. Shields and coworkers analyzed 77 cases based on macular versus extramacular location and reported more visual acuity loss $\geq$3 Snellen lines in the macular group (60% versus 13%) [45].

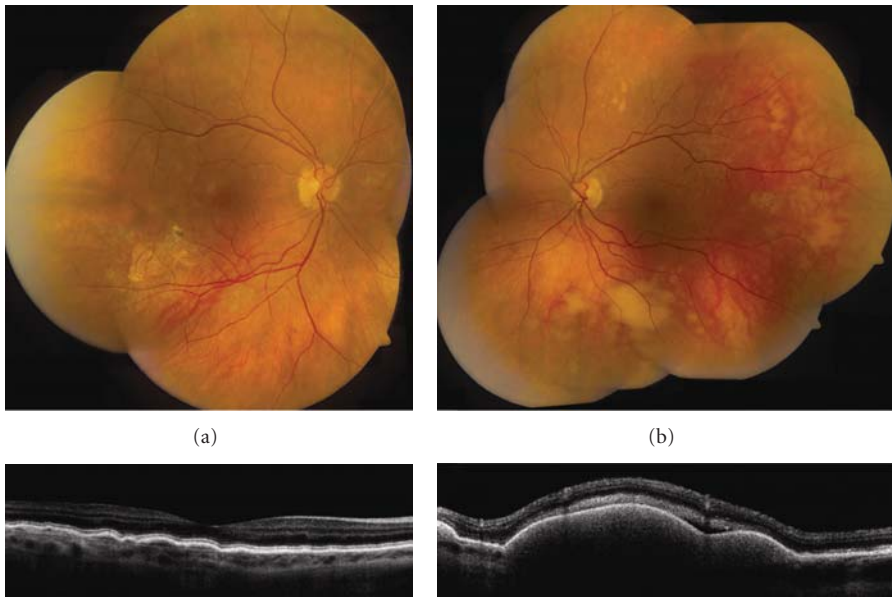

Figure 6: Vitreoretinal lymphoma. (a, b) Bilateral vitreoretinal lymphoma with multifocal cream-colored subretinal infiltrates. (c) Time domain OCT of the right eye reveals multiple nodular elevations of the RPE from deposits in the sub-RPE space. (d) Time domain OCT of the left eye shows multiple dome-shaped elevations of the RPE from more extensive infiltrates and subretinal fluid.

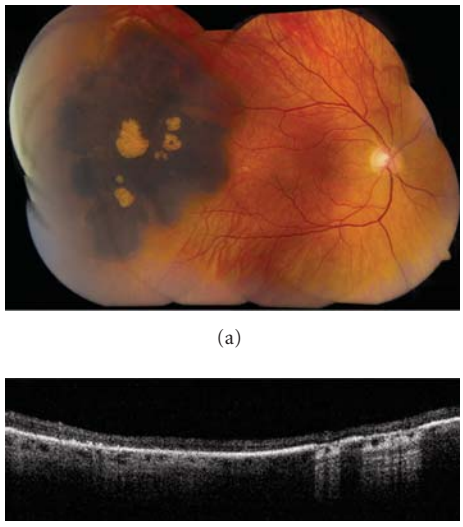

Figure 7: Congenital hypertrophy of the retinal pigment epithelium (CHRPE). (a) Large, peripheral CHRPE with centrally located lacunae. (b) Time domain OCT shows thinning of the overlying retina and loss of photoreceptors, posterior shadowing of the choroid in pigmented regions and light transmission to the underlying choroid in scans along lacunae.

Shields and colleagues described time domain OCT features in 11 cases of combined hamartoma of the retina and RPE, reporting anatomic disorganization with loss of identifiable retinal layers in all cases [46] (Figure 8). OCT evidence of epiretinal membrane was found in 91%, and mean retinal thickness was 766 um [46]. In their series, OCT images showed intact RPE in cases without significant posterior shadowing. Spectral domain OCT has been reported recently but did not add significant information to traditional time domain OCT [47].

10. Retinoblastoma

Retinoblastoma is the most common primary intraocular tumor in children. What used to be a malignancy with a dismal survival rate now has the highest cure rate in developed countries with the introduction of chemoreduction [48]. Retinoblastoma appears as a yellow-white retinal mass with feeding vessels when entirely intraretinal. When exhibiting an endophytic growth pattern, it is characterized by overlying vitreous seeds. Exophytic retinoblastoma, on the other hand, is associated with serous retinal detachment and occasional subretinal seeds. A rare diffuse pattern of growth is characterized by horizontal rather than vertical growth and can masquerade as uveitis [49].

Individual retinoblastoma tumors appear on OCT as thickening and disorganization of the neurosensory retina with posterior shadowing possibly from inherent calcification [5] (Figure 9). Associated subretinal fluid or intraretinal cysts are clearly visualized on OCT when present [5, 50]. The role of OCT lies in its ability to image the macula, particularly the fovea. This is important in children with retinoblastoma, since restoration of normal foveal anatomy may be achieved following treatment [51]. Further, differentiation from an organic (i.e., macular edema and loss of photoreceptors)

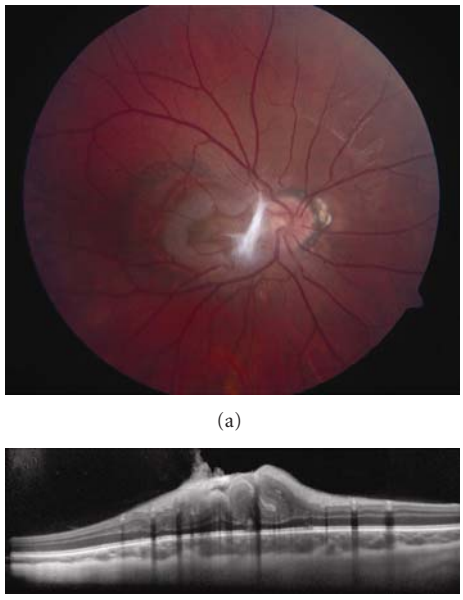

(a)

(b)

Figure 8: Combined hamartoma of the retina and RPE. (a) Macular combined hamartoma of the retina and RPE with dense preretinal fibrosis at its nasal border. (b) EDI OCT demonstrates gradual transition from the normal adjacent inner retinal layers to a disorganized mass with an overlying tuft of preretinal fibrosis. The outer plexiform layer, external limiting membrane, photoreceptor inner segment-outer segment junction, the RPE, and underlying choroid are intact.

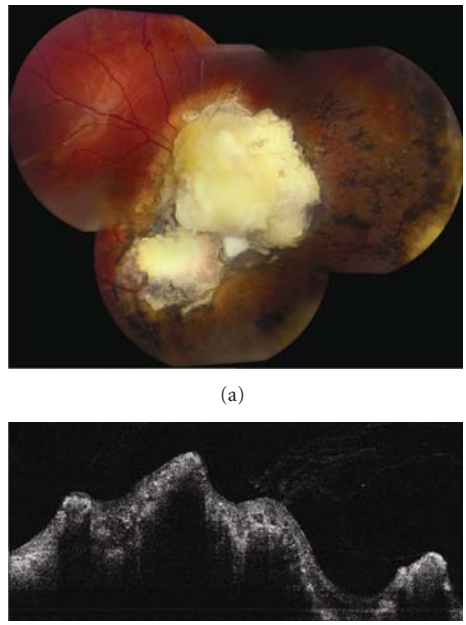

(a)

(b)

Figure 9: Retinoblastoma. (a) Mostly calcified retinoblastoma following chemoreduction and consolidation. (b) Time domain OCT demonstrates disorganization and irregularity of the inner retinal layers and posterior shadowing from calcification.

versus a nonorganic (i.e., amblyopia) cause of vision loss is essential to plan for long-term visual rehabilitation and maximizing outcome in all patients.

OCT images of retinoblastoma are difficult to obtain because traditional OCT imaging needs a certain degree of cooperation that is difficult to expect from children. This inherent limitation of OCT machines made reports on OCT of retinoblastoma few and lacking. Today, the development of handheld OCT has revolutionized intraoperative imaging capabilities that could have a tremendous impact on managing childhood ocular diseases such as retinopathy of prematurity and retinoblastoma [52]. These can deliver high-resolution spectral domain OCT images with 3D reconstruction capabilities [52].

11. Retinal Astrocytic Hamartoma

Retinal astrocytic hamartoma (astrocytoma) is a benign, vascularized, and glial tumor of the retina that may be acquired or congenital. Acquired astrocytic hamartomas appear as yellow-white mass of the inner retina that may be associated with adjacent retinal traction, cystoid macular edema, exudation, and nondilated feeder vessels. They generally lack calcification compared with the congenital form but are otherwise similar ophthalmoscopically. Congenital astrocytic hamartomas present in younger patients, may acquire intrinsic calcification through time, and are sometimes associated with central nervous system astrocytomas in the tuberous sclerosis complex. Both forms often do not require treatment but may at times exhibit progressive growth that leads to blindness and eye pain from neovascular glaucoma that require enucleation [53].

Astrocytic hamartomas show inner retinal thickening and disorganization with a gradual transition to the adjacent normal retina [5, 54] (Figure 10). Calcified tumors have higher reflectivity and greater posterior shadowing, while noncalcified tumors allow some light transmission to demonstrate intact outer retinal layers [54, 55]. There may be associated retinal traction in 27%, an intrinsic moth-eaten appearance from intratumoral cysts in 67%, and adjacent retinal or macular edema in 47% [54]. When treatment is initiated for macular edema, OCT may be used to follow resolution of subretinal fluid or release of macular traction [56, 57]. High-resolution spectral domain OCT confirms the intact outer retinal structures, as well as the underlying choriocapillaris [58]. 3D reconstruction demonstrates tumor architecture and its relationship to the adjacent retina in a single image [58].

12. Retinal Cavernous Hemangioma

Cavernous hemangioma is a benign retinal vascular tumor that appears as dark-red saccular aneurysms. This tumor can be associated with overlying preretinal fibrosis, vitreous hemorrhage, or vascular occlusion [28, 59]. Retinal exudation and edema are typically not associated [28]. There is a familial tendency from mutation of the cerebral cavernous malformation gene located in chromosome 7 in which

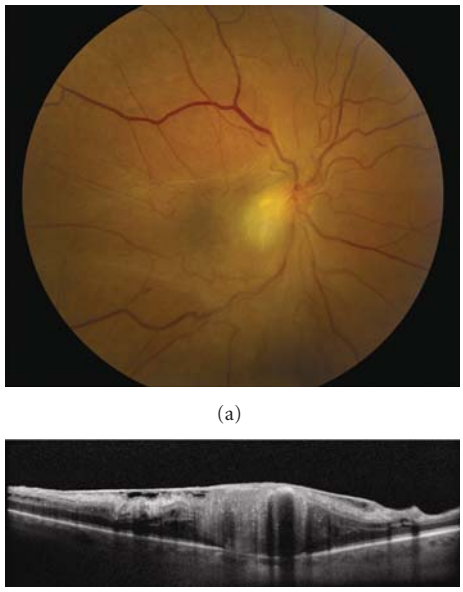

(a)

(b)

Figure 10: Retinal astrocytic hamartoma. (a) Juxtapapillary retinal astrocytic hamartoma with preretinal fibrosis and nasal dragging of the macula. (b) Spectral domain OCT image exhibits disorganization of the inner retinal layers and an intact RPE underlying the tumor. There is posterior shadowing presumably from calcification of the tumor apex. A dense epiretinal membrane causes the traction of the adjacent normal retina.

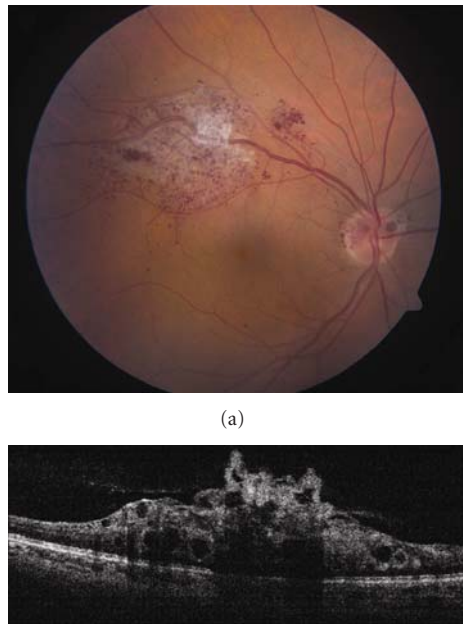

(a)

(b)

Figure 11: Retinal cavernous hemangioma. (a) Cavernous hemangioma along the superotemporal arcade with associated preretinal fibrosis. Note similar lesions over the optic disc. (b) Time domain OCT shows a lobulated inner retina with optically clear spaces representing the saccular aneurysms. The underlying RPE is intact.

cerebral or cutaneous cavernous hemangiomas may also be present [8, 28].

Features of cavernous hemangioma on OCT include lobulated, hyperreflective masses in the inner retina that correspond to the aneurysms. Optically clear cystic spaces may be present within the main hyperreflective mass [8, 60] (Figure 11). A preretinal membrane with traction on the adjacent retina may also be found; subretinal fluid is typically absent.

13. Retinal Hemangioblastoma

Retinal hemangioblastoma (capillary hemangioma) is an orange-red circumscribed vascular lesion with dilated feeding artery and draining vein. When multifocal, bilateral, or occurring in children less than 10 years, they are more often associated with von Hippel-Lindau disease [61]. This tumor can be associated with adjacent retinal exudation or remote cystoid macular edema. Advanced cases may have extensive serous retinal detachment, or neovascular glaucoma [28].

On OCT, retinal hemangioblastoma appears as an optically dense inner retinal mass with posterior shadowing due to intrinsic diffuse capillary channels [5, 8] (Figure 12). OCT is used mostly for the detection of macular edema, epiretinal membrane, and subretinal fluid associated with retinal hemangioblastoma [5, 8]. It is particularly useful for monitoring response to treatment.

14. Retinal Vasoproliferative Tumor

The vasoproliferative tumor of the ocular fundus is usually a unilateral, solitary, and yellow-red retinal lesion located in the inferotemporal periphery with minimally dilated or nondilated feeding artery and draining vein in contrast to hemangioblastoma. Most cases are primary, but 26% are secondary and associated with retinitis pigmentosa, pars planitis, and posterior uveitis, among others [62]. They may have associated macular edema, epiretinal membrane, exudative retinal detachment, or vitreous hemorrhage.

Inner retinal layer disorganization and posterior shadowing are features of vasoproliferative tumors on OCT [63] (Figure 13). They are difficult to image with OCT due to their peripheral location, but newer machines with longer scan lengths may be useful. OCT is beneficial for detecting associated preretinal fibrosis, macular edema, and subretinal fluid, as well as monitoring treatment [64].

15. Enhanced Depth Imaging Optical Coherence Tomography

Choroidal visualization has been rendered easier and more precise than before thanks to enhanced depth imaging (EDI) spectral domain OCT. The difficulty faced with conventional spectral domain OCT in imaging the choroid includes decreasing resolution and sensitivity with increasing depth beyond the retina, wavelength-dependent light scattering by RPE and choroid, and the limited 40 decibel dynamic range

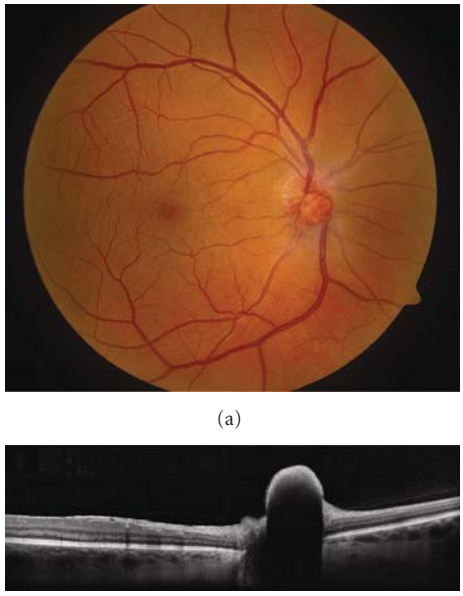

(a)

(b)

Figure 12: Hemangioblastoma. (a) Optic disc hemangioblastoma with a faint epiretinal membrane along the nasal edge of the fovea. (b) EDI OCT demonstrates a dome-shaped elevation of the inner retina with abrupt transition to the adjacent normal tissue and complete shadowing of the posterior layers. The adjacent RPE and choriocapillaris are intact.

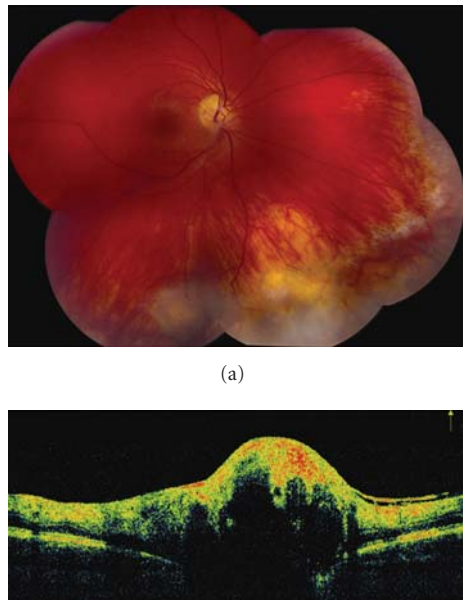

(a)

(b)

Figure 13: Vasoproliferative tumor. (a) Vasoproliferative tumor located at inferior periphery with preretinal fibrosis at its superior border and yellow subretinal fibrosis nasally. (b) Time domain OCT reveals a hyperreflective and disorganized inner retina with shadowing of the posterior layers including the RPE. An epiretinal membrane is seen at its posterior border.

inherent in Fourier domain systems. In EDI, the instrument is displaced to image deeper layers, and an inverted image is obtained with the superficial layers imaged at the bottom and the deeper layers imaged at the top. This image when flipped is comparable to the conventional spectral domain OCT image but with the choroid and inner sclera visualized at a higher resolution and sensitivity [65]. EDI OCT features have been described in normal choroid, age-related macular degeneration, and myopia [66–68]. This technique can be valuable for studying the structure and extent of choroidal tumors. A small pilot study suggested that small choroidal tumors (<1.0 mm in thickness and <9.0 mm in diameter), that are not detectable by ultrasonography, can be objectively measured by this technique [69]. Notably, even with high-quality choroidal images obtained, the retinal image quality is not compromised. In this preliminary study, EDI OCT showed promise in its ability to measure tumor thickness and visualizing internal structure. Its role in ocular oncology is hopeful, but further studies are still needed to better understand its histopathologic correlation.

16. Swept Source Imaging Optical Coherence Tomography

On the horizon is even higher-grade technology with "swept source" imaging. This employs a long wavelength light source that, at each point, a wavelength of light is rapidly swept across a band of wavelengths with a resultant signal detected by a sensitive photodiode. The photodiode is more sensitive and quicker than the charge-coupled devices (CCDs) used in spectral domain OCT. This extremely fast scan can produce 101,000 A scans per second. Imaging of both the retina and choroid is excellent with good deep penetration into the choroid due to the longer wavelength.

17. Conclusion

Conventional OCT is a valuable tool to visualize anatomic alterations induced by retinal and choroidal tumors. Newer OCT methods with EDI and swept source OCT can allow in vivo cross-sectional imaging of choroidal tumors with details on the tumor structure and measurement of tumor thickness too thin for measurement by ultrasonography.

Acknowledgments

This work was supported in part by a donation from Michael, Bruce, and Ellen Ratner, New York, NY, USA (C. L. Shields), Mellon Charitable Giving from the Martha W. Rogers Charitable Trust (C. L. Shields), the Rosenthal Award of the Macula Society (C. L. Shields), and the Eye Tumor Research Foundation, Philadelphia, PA, USA (C. L. Shields).

References

[1] D. Huang, E. A. Swanson, C. P. Lin et al., "Optical coherence tomography," *Science*, vol. 254, no. 5035, pp. 1178–1181, 1991.

[2] P. A. Testoni and B. Mangiavillano, "Optical coherence tomography in detection of dysplasia and cancer of the

gastrointestinal tract and bilio-pancreatic ductal system," *World Journal of Gastroenterology*, vol. 14, no. 42, pp. 6444–6452, 2008.

[3] T. Gambichler, G. Moussa, M. Sand, D. Sand, P. Altmeyer, and K. Hoffmann, "Applications of optical coherence tomography in dermatology," *Journal of Dermatological Science*, vol. 40, no. 2, pp. 85–94, 2005.

[4] H. G. Bezerra, M. A. Costa, G. Guagliumi, A. M. Rollins, and D. I. Simon, "Intracoronary optical coherence tomography a comprehensive review: clinical and research applications," *Journal of the American College of Cardiology*, vol. 2, no. 11, pp. 1035–1046, 2009.

[5] C. L. Shields, A. Mashayekhi, C. K. Luo, M. A. Materin, and J. A. Shields, "Optical coherence tomography in children: analysis of 44 eyes with intraocular tumors and simulating conditions," *Journal of Pediatric Ophthalmology and Strabismus*, vol. 41, no. 6, pp. 338–344, 2004.

[6] M. Khandwala, B. R. Penmetsa, S. Dey, J. B. Schofield, C. A. Jones, and A. Podoleanu, "Imaging of periocular basal cell carcinoma using en face optical coherence tomography: a pilot study," *British Journal of Ophthalmology*, vol. 94, no. 10, pp. 1332–1336, 2010.

[7] S. R. Ferenczy, S. Harmon, and C. L. Shields, "Optical coherence tomography in ocular oncology," *Journal of Ophthalmic Photography*, vol. 31, pp. 74–79, 2009.

[8] C. L. Shields, M. A. Materin, and J. A. Shields, "Review of optical coherence tomography for intraocular tumors," *Current Opinion in Ophthalmology*, vol. 16, no. 3, pp. 141–154, 2005.

[9] R. F. Spaide, H. Koizumi, and M. C. Pozonni, "Enhanced depth imaging spectral-domain optical coherence tomography," *American Journal of Ophthalmology*, vol. 146, no. 4, pp. 496–500, 2008.

[10] K. Sayanagi, D. E. Pelayes, P. K. Kaiser, and A. D. Singh, "3D Spectral domain optical coherence tomography findings in choroidal tumors," *European Journal of Ophthalmology*, vol. 21, no. 3, pp. 271–275, 2011.

[11] C. H. Ng, J. J. Wang, P. Mitchell, F. M. A. Islam, and T. Y. Wong, "Prevalence and characteristics of choroidal nevi in an asian vs white population," *Archives of Ophthalmology*, vol. 127, no. 3, pp. 314–319, 2009.

[12] A. D. Singh, P. Kalyani, and A. Topham, "Estimating the risk of malignant transformation of a choroidal nevus," *Ophthalmology*, vol. 112, no. 10, pp. 1784–1789, 2005.

[13] C. L. Shields, J. A. Shields, H. Kiratli, P. De Potter, J. R. Cater, and I. W. McLean, "Risk factors for growth and metastasis of small choroidal melanocytic lesions," *Ophthalmology*, vol. 102, no. 9, pp. 1351–1361, 1995.

[14] C. L. Shields, J. Cater, J. A. Shields, A. D. Singh, M. C. M. Santos, and C. Carvalho, "Combination of clinical factors predictive of growth of small choroidal melanocytic tumors," *Archives of Ophthalmology*, vol. 118, no. 3, pp. 360–364, 2000.

[15] C. L. Shields, A. Mashayekhi, M. A. Materin et al., "Optical coherence tomography of choroidal nevus in 120 patients," *Retina*, vol. 25, no. 3, pp. 243–252, 2005.

[16] C. L. Shields, M. Furuta, A. Mashayekhi et al., "Visual acuity in 3422 consecutive eyes with choroidal nevus," *Archives of Ophthalmology*, vol. 125, no. 11, pp. 1501–1507, 2007.

[17] C. L. Shields, M. Furuta, A. Thangappan et al., "Metastasis of uveal melanoma millimeter-by-millimeter in 8033 consecutive eyes," *Archives of Ophthalmology*, vol. 127, no. 8, pp. 989–998, 2009.

[18] S. Muscat, S. Parks, E. Kemp, and D. Keating, "Secondary retinal changes associated with choroidal naevi and melanomas documented by optical coherence tomography," *British Journal of Ophthalmology*, vol. 88, no. 1, pp. 120–124, 2004.

[19] G. Espinoza, B. Rosenblatt, and J. W. Harbour, "Optical coherence tomography in the evaluation of retinal changes associated with suspicious choroidal melanocytic tumors," *American Journal of Ophthalmology*, vol. 137, no. 1, pp. 90–95, 2004.

[20] A. D. Singh, R. N. Belfort, K. Sayanagi, and P. K. Kaiser, "Fourier domain optical coherence tomographic and autofluorescence findings in indeterminate choroidal melanocytic lesions," *British Journal of Ophthalmology*, vol. 94, no. 4, pp. 474–478, 2010.

[21] L. M. Heindl, C. Y. Mardin, L. M. Holbach, G. O. H. Naumann, F. E. Kruse, and H. L. J. Knorr, "Vitreal seeding from uveal melanoma detected by high-resolution spectral-domain optical coherence tomography," *Archives of Ophthalmology*, vol. 127, no. 8, pp. 1062–1064, 2009.

[22] N. Horgan, C. L. Shields, A. Mashayekhi, L. F. Teixeira, M. A. Materin, and J. A. Shields, "Early macular morphological changes following plaque radiotherapy for uveal melanoma," *Retina*, vol. 28, no. 2, pp. 263–273, 2008.

[23] C. L. Shields, J. A. Shields, N. E. Gross, G. P. Schwartz, and S. E. Lally, "Survey of 520 eyes with uveal metastases," *Ophthalmology*, vol. 104, no. 8, pp. 1265–1276, 1997.

[24] S. Natesh, K. J. Chin, and P. T. Finger, "Choroidal metastases fundus autofluorescence imaging: correlation to clinical, OCT, and fluorescein angiographic findings," *Ophthalmic Surgery Lasers and Imaging*, vol. 41, no. 4, pp. 406–412, 2010.

[25] J. F. Arevalo, C. F. Fernandez, and R. A. Garcia, "Optical coherence tomography characteristics of choroidal metastasis," *Ophthalmology*, vol. 112, no. 9, pp. 1612–1619, 2005.

[26] M. E. Manquez, C. L. Shields, E. C. Karatza, and J. A. Shields, "Regression of choroidal metastases from breast carcinoma using aromatase inhibitors," *British Journal of Ophthalmology*, vol. 89, no. 6, pp. 776–777, 2005.

[27] C. L. Shields, S. G. Honavar, J. A. Shields, J. Cater, and H. Demirci, "Circumscribed choroidal hemangioma: clinical manifestations and factors predictive of visual outcome in 200 consecutive cases," *Ophthalmology*, vol. 108, no. 12, pp. 2237–2248, 2001.

[28] J. A. Shields and C. L. Shields, *Intraocular Tumors: An Atlas and Textbook*, Lippincott Williams & Wilkins, Philadelphia, Pa, USA, 2nd edition, 2008.

[29] A. Ramasubramanian, C. L. Shields, S. A. Harmon, and J. A. Shields, "Autofluorescence of choroidal hemangioma in 34 consecutive eyes," *Retina*, vol. 30, no. 1, pp. 16–22, 2010.

[30] M. A. Blasi, A. C. Tiberti, A. Scupola et al., "Photodynamic therapy with verteporfin for symptomatic circumscribed choroidal hemangioma: five-year outcomes," *Ophthalmology*, vol. 117, pp. 1630–1637, 2010.

[31] G. W. Aylward, T. S. Chang, S. E. Pautler, and M. D. Gass, "A long-term follow-up of choroidal osteoma," *Archives of Ophthalmology*, vol. 116, no. 10, pp. 1337–1341, 1998.

[32] C. L. Shields, H. Sun, H. Demirci, and J. A. Shields, "Factors predictive of tumor growth, tumor decalcification, choroidal neovascularization, and visual outcome in 74 eyes with choroidal osteoma," *Archives of Ophthalmology*, vol. 123, no. 12, pp. 1658–1666, 2005.

[33] T. Ide, N. Ohguro, A. Hayashi et al., "Optical coherence tomography patterns of choroidal osteoma," *American Journal of Ophthalmology*, vol. 130, no. 1, pp. 131–134, 2000.

[34] A. Fukasawa and H. Iijima, "Optical coherence tomography of choroidal osteoma," *American Journal of Ophthalmology*, vol. 133, no. 3, pp. 419–421, 2002.

[35] C. L. Shields, B. Perez, M. A. Materin, S. Mehta, and J. A. Shields, "Optical coherence tomography of choroidal osteoma in 22 cases: evidence for photoreceptor atrophy over the decalcified portion of the tumor," *Ophthalmology*, vol. 114, no. 12, pp. e53–e58, 2007.

[36] S. E. Coupland and B. Damato, "Understanding intraocular lymphomas," *Clinical and Experimental Ophthalmology*, vol. 36, no. 6, pp. 564–578, 2008.

[37] T. S. Chang, S. F. Byrne, J. D. M. Gass, J. Randall Hughes, R. N. Johnson, and T. G. Murray, "Echographic findings in benign reactive lymphoid hyperplasia of the choroid," *Archives of Ophthalmology*, vol. 114, no. 6, pp. 669–675, 1996.

[38] E. Kim, C. Kim, J. Lee, and Y. Cho, "A case of primary intraocular lymphoma treated by intravitreal methotrexate," *Korean Journal of Ophthalmology*, vol. 23, no. 3, pp. 210–214, 2009.

[39] T. Ishida, K. Ohno-Matsui, Y. Kaneko et al., "Fundus autofluorescence patterns in eyes with primary intraocular lymphoma," *Retina*, vol. 30, no. 1, pp. 23–32, 2010.

[40] C. Fardeau, C. P. L. Lee, H. Merle-Béral et al., "Retinal fluorescein, indocyanine green angiography, and optic coherence tomography in non-hodgkin primary intraocular lymphoma," *American Journal of Ophthalmology*, vol. 147, no. 5, pp. 886–894, 2009.

[41] B. K. Williams, I. Tsui, and T. A. McCannel, "Spectral-domain optical coherence tomography of conjunctival mucosa-associated lymphoid tissue lymphoma with presumed choroidal involvement," *Graefe's Archive for Clinical and Experimental Ophthalmology*, vol. 248, pp. 1837–1840, 2010.

[42] C. L. Shields, A. Mashayekhi, T. Ho, J. Cater, and J. A. Shields, "Solitary congenital hypertrophy of the retinal pigment epithelium: clinical features and frequency of enlargement in 330 patients," *Ophthalmology*, vol. 110, no. 10, pp. 1968–1976, 2003.

[43] C. L. Shields, M. A. Materin, C. Walker, B. P. Marr, and J. A. Shields, "Photoreceptor loss overlying congenital hypertrophy of the retinal pigment epithelium by optical coherence tomography," *Ophthalmology*, vol. 113, no. 4, pp. 661–665, 2006.

[44] A. P. Schachat, J. A. Shields, and S. L. Fine, "Combined hamartomas of the retina and retinal pigment epithelium," *Ophthalmology*, vol. 91, no. 12, pp. 1609–1615, 1984.

[45] C. L. Shields, A. Thangappan, K. Hartzell, P. Valente, C. Pirondini, and J. A. Shields, "Combined hamartoma of the retina and retinal pigment epithelium in 77 consecutive patients. Visual outcome based on macular versus extramacular location," *Ophthalmology*, vol. 115, no. 12, pp. 2246–2252, 2008.

[46] C. L. Shields, A. Mashayekhi, V. V. Dai, M. A. Materin, and J. A. Shields, "Optical coherence tomographic findings of combined hamartoma of the retina and retinal pigment epithelium in 11 patients," *Archives of Ophthalmology*, vol. 123, no. 12, pp. 1746–1750, 2005.

[47] C. S. Huot, K. B. Desai, and V. A. Shah, "Spectral domain optical coherence tomography of combined hamartoma of the retina and retinal pigment epithelium," *Ophthalmic Surgery Lasers and Imaging*, vol. 40, no. 3, pp. 322–324, 2009.

[48] C. L. Shields and J. A. Shields, "Retinoblastoma management: advances in enucleation, intravenous chemoreduction, and intra-arterial chemotherapy," *Current Opinion in Ophthalmology*, vol. 21, no. 3, pp. 203–212, 2010.

[49] C. L. Shields, F. Ghassemi, S. Tuncer, A. Thangappan, and J. A. Shields, "Clinical spectrum of diffuse infiltrating retinoblastoma in 34 consecutive eyes," *Ophthalmology*, vol. 115, no. 12, pp. 2253–2258, 2008.

[50] N. Sinha, C. L. Shields, A. Ramasubramanian, S. Ferenczy, and J. A. Shields, "Giant spontaneously regressed retinoblastoma," *Canadian Journal of Ophthalmology*, vol. 45, no. 1, pp. 89–90, 2010.

[51] C. L. Shields, M. A. Materin, and J. A. Shields, "Restoration of foveal anatomy and function following chemoreduction for bilateral advanced retinoblastoma with total retinal detachment," *Archives of Ophthalmology*, vol. 123, no. 11, pp. 1611–1612, 2005.

[52] S. K. Houston, T. G. Murray, S. Q. Wolfe, and C. E. Fernandes, "Current update on retinoblastoma," *International Ophthalmology Clinics*, vol. 51, no. 1, pp. 77–91, 2011.

[53] C. L. Shields, J. A. Shields, R. C. Eagle, and F. Cangemi, "Progressive enlargement of acquired retinal astrocytoma in 2 cases," *Ophthalmology*, vol. 111, no. 2, pp. 363–368, 2004.

[54] C. L. Shields, R. Benevides, M. A. Materin, and J. A. Shields, "Optical coherence tomography of retinal astrocytic hamartoma in 15 cases," *Ophthalmology*, vol. 113, no. 9, pp. 1553–1557, 2006.

[55] W. Soliman, M. Larsen, B. Sander, M. Wegener, and D. Milea, "Optical coherence tomography of astrocytic hamartomas in tuberous sclerosis," *Acta Ophthalmologica Scandinavica*, vol. 85, no. 4, pp. 454–455, 2007.

[56] S. Eskelin, P. Tommila, T. Palosaari, and T. Kivelä, "Photodynamic therapy with verteporfin to induce regression of aggressive retinal astrocytomas," *Acta Ophthalmologica*, vol. 86, no. 7, pp. 794–799, 2008.

[57] M. Inoue, A. Hirakarta, N. Iizuka, S. Futagami, and T. Hida, "Tractional macular detachment associated with optic disc astrocytic hamartoma," *Acta Ophthalmologica*, vol. 87, no. 2, pp. 239–240, 2009.

[58] K. Kimoto, D. Kishi, H. Kono, J. Ikewaki, K. Shinoda, and K. Nakatsuka, "Diagnosis of an isolated retinal astrocytic hamartoma aided by optical coherence tomography," *Acta Ophthalmologica*, vol. 86, no. 8, pp. 921–922, 2008.

[59] E. Messmer, H. Laqua, and A. Wessing, "Nine cases of cavernous hemangioma of the retina," *American Journal of Ophthalmology*, vol. 95, no. 3, pp. 383–390, 1983.

[60] R. E. Andrade, M. E. Farah, R. A. Costa, and R. Belfort, "Optical coherence tomography findings in macular cavernous haemangioma," *Acta Ophthalmologica Scandinavica*, vol. 83, no. 2, pp. 267–269, 2005.

[61] A. D. Singh, J. A. Shields, and C. L. Shields, "Solitary retinal capillary hemangioma. Hereditary (von Hippel-Lindau disease) or nonhereditary?" *Archives of Ophthalmology*, vol. 119, no. 2, pp. 232–234, 2001.

[62] C. L. Shields, J. A. Shields, J. Barrett, and P. De Potter, "Vasoproliferative tumors of the ocular fundus. Classification and manifestations in 103 patients," *Archives of Ophthalmology*, vol. 113, no. 5, pp. 615–623, 1995.

[63] M. E. Turell and A. D. Singh, "Vascular tumors of the retina and choroid: diagnosis and treatment," *Middle East African Journal of Ophthalmology*, vol. 17, no. 3, pp. 191–200, 2010.

[64] V. M. L. Cohen, C. L. Shields, H. Demirci, and J. A. Shields, "Iodine I 125 plaque radiotherapy for vasoproliferative tumors of the retina in 30 eyes," *Archives of Ophthalmology*, vol. 126, no. 9, pp. 1245–1251, 2008.

[65] R. F. Spaide, H. Koizumi, and M. C. Pozonni, "Enhanced depth imaging spectral-domain optical coherence tomography," *American Journal of Ophthalmology*, vol. 146, no. 4, pp. 496–500, 2008.

[66] R. Margolis and R. F. Spaide, "A pilot study of enhanced depth imaging optical coherence tomography of the choroid in normal eyes," *American Journal of Ophthalmology*, vol. 147, no. 5, pp. 811–815, 2009.

[67] R. F. Spaide, "Enhanced depth imaging optical coherence tomography of retinal pigment epithelial detachment in age-related macular degeneration," *American Journal of Ophthalmology*, vol. 147, no. 4, pp. 644–652, 2009.

[68] T. Fujiwara, Y. Imamura, R. Margolis, J. S. Slakter, and R. F. Spaide, "Enhanced depth imaging optical coherence tomography of the choroid in highly myopic eyes," *American Journal of Ophthalmology*, vol. 148, no. 3, pp. 445–450, 2009.

[69] V. L. Torres, N. Brugnoni, P. K. Kaiser, and A. D. Singh, "Optical coherence tomography enhanced depth imaging of choroidal tumors," *American Journal of Ophthalmology*, vol. 151, no. 4, pp. 586–593, 2011.

Hindawi Publishing Corporation
Journal of Ophthalmology
Volume 2011, Article ID 928205, 4 pages
doi:10.1155/2011/928205

Clinical Study

Optical Coherence Tomography Findings in Idiopathic Macular Holes

Lynn L. Huang, David H. Levinson, Jonathan P. Levine, Umar Mian, and Irena Tsui

Retina Division, Department of Ophthalmology, Montefiore Medical Center, Albert Einstein College of Medicine, The Bronx, NY 10467, USA

Correspondence should be addressed to Irena Tsui, itsui@montefiore.org

Received 14 March 2011; Accepted 20 June 2011

Academic Editor: Fernando M. Penha

Purpose. To describe the characteristics of idiopathic macular holes (MH) on optical coherence tomography (OCT) and correlate OCT with clinical assessment. *Design*. Cross-sectional chart review and OCT assessment. *Participants*. Sixty-seven eyes with a clinically diagnosed idiopathic MH with available OCT data. *Methods*. A retrospective chart review and OCT assessment. *Results*. Based on OCT grading, 40 eyes had a full-thickness macular hole (FTMH) and 21 eyes had a lamellar macular hole (LMH). Clinical exam and OCT assessment agreed in 53 (87%) eyes when assessing the extent of MH. Six eyes (14.6%) in the FTMH group, and 3 eyes in the LMH group (14.3%) had persistent vitreomacular traction. Thirty-seven eyes (92.5%) in the FTMH group and 11 eyes (52.4%) in the LMH group had associated intraretinal cysts. Two eyes (5.0%) in the FTMH group and zero eyes in the LMH group had subretinal fluid. Intraretinal cysts were found to be more frequently associated with FTMH than with LMH ($P < 0.001$). *Conclusion*. This paper described OCT findings in a group of patients with clinically diagnosed MH. A high level of correlation between clinical assessment and OCT findings of LMH and FTMH was observed, and intraretinal cysts were often present in FTMH.

1. Introduction

For decades, macular holes (MH) have been classified by fundus biomicroscopy in four stages, as first described by Donald Gass in 1988 [1, 2]. The Gass classification is based on the fovea appearance, the estimated size of the hole, and whether or not the posterior vitreous is separated (Table 1). Confirmation of full-thickness macular holes (FTMH) can be performed with further clinical investigations such as Amsler grid assessment, the Watzke-Allen sign, or the laser aiming beam test [3].

Optical coherence tomography (OCT) has enhanced our understanding of MH by providing an objective and reproducible way of visualizing the macula. It confirmed the pathogenesis of idiopathic MH by introducing the concept of stage 0 macular hole, or vitreomacular traction (VMT) [4].

OCT provides confirmation of clinical findings, further anatomic characterization, means of educating patients, and improved staging of MH. In a study of 61 eyes with all stages of MH, OCT offered additional or different information in 92% of stage 1 MH [5]. Clinical assessment of late-staged MH is enhanced with OCT by enabling measurement of the diameter of the MH and visualizing the posterior hyaloid.

The purpose of this study was to describe OCT findings of idiopathic MH in a series of consecutive patients seen at a single tertiary care practice.

2. Methods

A retrospective chart review was performed at the Henkind Eye Institute at the Montefiore Medical Center in Bronx, New York. Institutional Review Board approval was obtained for this study. All research was carried out in accordance with the Health Insurance Portability and Accountability Act of 1996.

An initial search for the diagnosis of "macular hole" (International Classification of Diseases Ninth Revision 362.54) was done among 15,600 patient visits in the clinic database over a three-year time period. Charts were reviewed to confirm the clinical diagnosis of MH, and only idiopathic

Table 1: Modified Gass classification system of macular holes.

Stage	Description
Stage 1a	Yellow spot with loss of foveal depression, no vitreous separation
Stage 1b	Yellow ring with loss of foveal depression, no vitreous separation
Stage 2	Small full-thickness macular hole < 400 microns
Stage 3	Full-thickness macular hole > 400 microns, no vitreous separation
Stage 4	Full-thickness macular hole > 400 microns, complete vitreous separation

MH were included. Macular holes associated with trauma, retinal detachment, diabetic retinopathy, or myopia were excluded. Macular pseudoholes (MPH) associated with an epiretinal membrane by clinical diagnosis were also excluded. Patients with the initial clinical diagnosis of MH but no OCT were also excluded. Charts were reviewed for demographical (age, sex) and clinical information (visual acuity, clinical staging).

OCT was taken with time-domain OCT (Stratus OCT, Carl Zeiss Meditec, Inc., Dublin, CA, USA) using 6-line raster protocol or spectral-domain OCT (Cirrus OCT, Carl Zeiss Meditec, Inc., Dublin, CA, USA) using 5-line raster protocol. Assessment of OCT was based on both chart data and, when available, realtime imaging on the scanner. OCT review was done by two observers. OCT was evaluated for the extent of MH formation, for example, lamellar macular hole (LMH) versus FTMH. Additional OCT findings such as the presence of VMT seen as foveal vitreomacular adhesion, intraretinal cysts, and subretinal fluid (SRF) were evaluated. The relationship between OCT findings and the extent of MH and the agreement between clinical diagnosis and OCT diagnosis (LMH versus FTMH) were assessed using Chi-square tests.

3. Results

An initial search by ICD-9 code revealed 133 patients with the diagnosis of MH. A total of 112 charts were available for review. Eighty eyes met inclusion criteria for idiopathic MH by clinical documentation. Among these eyes, 67 eyes had available OCT data at presentation.

The mean age of patients was 71 years (range 35–97 years.) Forty-nine (69%) patients were female, accounting for a female-to-male ratio of 2.2 : 1. Best corrected visual acuity (BCVA) at presentation ranged from 20/25 to counting fingers (CF.) Forty-eight (60%) eyes had BCVA ≤ 20/200. Twenty eyes (25%) had BCVA ≥ 20/40. Twenty eyes were clinically diagnosed as LMH and 43 eyes as FTMH. The median BCVA was 20/70 in LMH group and 20/200 in FTMH group.

3.1. OCT Findings. Among 67 eyes with OCT data, 32 (48%) had TD-OCT, and 37 (55%) had SD-OCT. Four eyes were found to have epiretinal membrane with MPH and 2 eyes with resolved MH on OCT were excluded from the final analysis. Based on OCT grading, 40 eyes (66%) had FTMH and 21 eyes (35%) had LMH. Six (15%) of 40 eyes with FTMH by OCT evaluation had VMT versus 3/21 (14%) eyes with an LMH. Thirty-seven (93%) of 40 eyes with an FTMH by OCT evaluation had associated intraretinal cysts versus 11/21 (52%) eyes with a LMH. Two of 40 (5%) eyes with an FTMH by OCT evaluation had SRF versus zero eyes with an LMH. Intraretinal cysts were found to be more frequently associated with FTMH than in LMH ($P < 0.001$; Table 2).

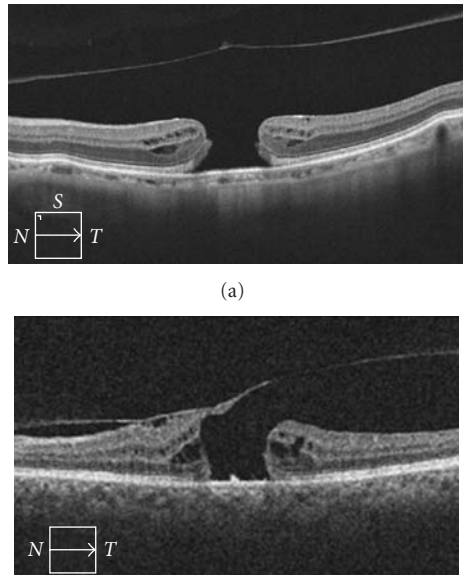

(a)

(b)

Figure 1: Optical coherence tomography of full-thickness macular holes (a) with separation of the posterior vitreous from the fovea and (b) with vitreomacular traction. Note the difference in foveal contour, as well as the presence of intraretinal cysts.

3.2. Clinical Exam and OCT Agreement. Overall, clinical exam and OCT data agreed in 53 (87%) eyes when assessing the extent of IMH (LMH versus FTMH.) The rate of agreement was higher in the OCT-confirmed FTMH group (93%) than in the OCT-confirmed LMH group (76%) ($P < 0.1$; Table 2).

4. Discussion

This paper was a descriptive OCT study of idiopathic MH captured at a large tertiary care center. Besides distinguishing LMH and FTMH, OCT data provided additional information such as the presence of VMT, intraretinal cysts, and SRF. VMT occurred at about the same rate (14-15%) in both LMH and FTMH. An example of an FTMH with and without VMT is shown in Figure 1. Intraretinal cysts were found to be significantly more common in FTMH than in LMH. Figures 1–3 demonstrate intraretinal cysts; the presence of cysts on OCT in all stages of MH formation has been previously reported [6, 7]. SRF was uncommon in both

Table 2: Optical coherence tomography (OCT) summary (MH = macular hole; VMT = vitreomacular traction; IRC = intraretinal cysts; SRF = subretinal fluid).

OCT diagnosis	Additional OCT findings			Agreement with clinical exam (%)
	VMT (%)	IRC (%)	SRF (%)	
Total MH ($n = 61$)	9 (15)	48 (79)	2 (3)	53 (87)
Lamellar MH ($n = 21$)	3 (14)	11 (52)	0 (0)	16 (76)
Full-thickness MH ($n = 40$)	6 (15)	37 (93)	2 (5)	37 (93)
P value	>0.1	<.001	>0.1	<0.1

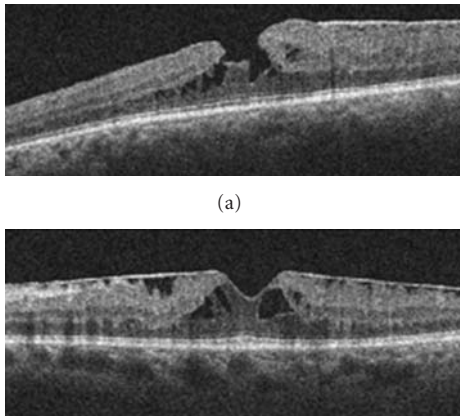

(a)

(b)

Figure 2: Optical coherence tomography of (a) a lamellar macular hole and (b) an epiretinal membrane with macular pseudohole. Note the difference in foveal contour, as well as intraretinal cysts.

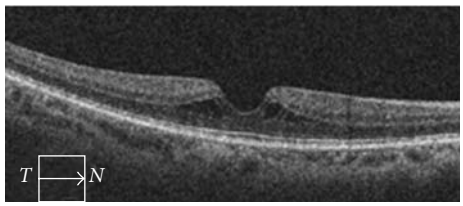

Figure 3: Optical coherence tomography of a lamellar macular hole with a smooth foveal contour. Notice intraretinal cysts.

LMH and FTMH among our patients. Fellow eyes should be imaged as well to look for subclinical VMT and intraretinal cysts, as these factors indicate increased risk of developing MH [6].

LMH were classified as a partial-thickness MH which showed an irregularity of the contour at the foveal center, and MPH as partial-thickness retinal defects associated with an epiretinal membrane and smooth configuration at the foveal center (Figure 2.) These two entities are generally considered different from each other [8, 9]. However, the distinction between MPH and LMH was not always clear. For example, one eye had a smooth contour at the foveal center without the presence of an epiretinal membrane (Figure 3). Furthermore, Michalewski et al. have reported a case of MPH that evolved into a lamellar IMH [10].

In the present study overall agreement between clinical examination and OCT was 87% and higher in the FTMH group than in the LMH group. However, clinicians were not blinded to the OCT results at time of clinical exam, thus the true rate of agreement may be lower, highlighting the utility of OCT in characterizing and staging MH. It would be interesting to assess the sensitivity and specificity of clinical examination for the diagnosis of MH, using OCT as the gold standard. Given its low incidence, however, this would require imaging a very large number of eyes.

OCT has greatly advanced innovations in the treatment for MH by offering an objective means of assessing MH closure. For example, the necessity of internal limiting membrane (ILM) peeling, adjunctive ILM staining, and postoperative positioning are controversial concepts, which have recently been evaluated by OCT [11–13]. Clinical trials with microplasmin for the nonsurgical closure of FTMH also used OCT as a primary outcome [14].

A limitation of the present study is the retrospective data collection and use of two different OCT machines. Therefore, our OCT analysis was limited to subjective evaluation without quantitative comparisons. Although OCT provides anatomical information about the fovea, other imaging modalities, such as autofluorescence and fluorescein angiography, can provide functional information of the underlying retinal pigment epithelial cells [15, 16]. These additional tests can be considered for prospective studies on MH.

In summary this study described OCT findings in a group of patients with clinically diagnosed MH. A high level of correlation between clinical assessment and OCT findings of LMH and FTMH was observed; intraretinal cysts were often present in FTMH. Understanding of the etiology and management of MH has evolved with the use of OCT technology.

Acknowledgments

The authors would like to express deep appreciation to Theresa D'Abbraccio and Christina Rivera for their administrative assistance, as well as to Kenneth Boyd for his help with ophthalmic photography.

References

[1] R. N. Johnson and J. D. Gass, "Idiopathic macular holes. Observation, stages of formation, and implications for surgical intervention," *Ophthalmology*, vol. 95, no. 7, pp. 917–924, 1988.

[2] J. D. Gass, "Reappraisal of biomicroscopic classification of stages of development of a macular hole," *American Journal of Ophthalmology*, vol. 119, no. 6, pp. 752–759, 1995.

[3] J. Martinez, W. E. Smiddy, J. Kim, and J. D. Gass, "Differentiating macular holes from macular pseudoholes," *American Journal of Ophthalmology*, vol. 117, no. 6, pp. 762–767, 1994.

[4] A. Chan, J. S. Duker, J. S. Schuman, and J. G. Fujimoto, "Stage 0 macular holes: observations by optical coherence tomography," *Ophthalmology*, vol. 111, no. 11, pp. 2027–2032, 2004.

[5] C. Azzolini, F. Patelli, and R. Brancato, "Correlation between optical coherence tomography data and biomicroscopic interpretation of idiopathic macular hole," *American Journal of Ophthalmology*, vol. 132, no. 3, pp. 348–355, 2001.

[6] A. Spiritus, L. Dralands, P. Stalmans, I. Stalmans, and W. Spileers, "OCT study of fellow eyes of macular holes," *Bulletin de la Société belge d'ophtalmologie*, vol. 275, pp. 81–84, 2000.

[7] P. T. Yeh, T. C. Chen, C. H. Yang et al., "Formation of idiopathic macular hole-reappraisal," *Graefe's Archive for Clinical and Experimental Ophthalmology*, vol. 248, no. 6, pp. 793–798, 2010.

[8] J. C. Chen and L. R. Lee, "Clinical spectrum of lamellar macular defects including pseudoholes and pseudocysts defined by optical coherence tomography," *British Journal of Ophthalmology*, vol. 92, no. 10, pp. 1342–1346, 2008.

[9] B. Haouchine, P. Massin, R. Tadayoni, A. Erginay, and A. Gaudric, "Diagnosis of macular pseudoholes and lamellar macular holes by optical coherence tomography," *American Journal of Ophthalmology*, vol. 138, no. 5, pp. 732–739, 2004.

[10] J. Michalewski, Z. Michalewska, K. Dziegielewski, and J. Nawrocki, "Evolution from macular pseudohole to lamellar macular hote-spectral domain OCT study," *Graefe's Archive for Clinical and Experimental Ophthalmology*, vol. 249, no. 2, pp. 175–178, 2011.

[11] A. Kumar, V. Gogia, V. M. Shah, and T. C. Nag, "Comparative evaluation of anatomical and functional outcomes using brilliant blue G versus triamcinolone assisted ILM peeling in macular hole surgery in Indian population," *Graefe's Archive for Clinical and Experimental Ophthalmology*, vol. 249, no. 7, pp. 987–995, 2011.

[12] M. M. Muqit, I. Akram, G. S. Turner, and P. E. Stanga, "Fourier-domain optical coherence tomography imaging of gass temponade following macular hole surgery," *Ophthalmic Surgery, Lasers & Imaging*, vol. 1, p. 41, 2010.

[13] M. Karkanová, E. Vlková, H. Dosková, and P. Kolár, "The influence of the idiopathic macular hole (IMH) surgery with the ILM peeling, and gas tamponade on the electrical function of the retina," *Ceská a Slovenská Oftalmologie*, vol. 66, no. 2, pp. 84–88, 2010.

[14] M. S. Benz, K. H. Packo, V. Gonzalez et al., "A placebo-controlled trial of microplasmin intravitreous injection to facilitate posterior vitreous detachment before vitrectomy," *Ophthalmology*, vol. 117, no. 4, pp. 791–797, 2010.

[15] H. Chung, C. J. Shin, J. G. Kim, Y. H. Yoon, and H. C. Kim, "Correlation of microperimetry with fundus autofluorescence and spectral-domain optical coherence tomography in repaired macular holes," *American Journal of Ophthalmology*, vol. 151, no. 1, pp. 128–136, 2011.

[16] M. U. Saeed and H. Heimann, "Atrophy of the retinal pigment epithelium following vitrectomy with trypan blue," *International Ophthalmology*, vol. 29, no. 4, pp. 239–241, 2009.

Hindawi Publishing Corporation
Journal of Ophthalmology
Volume 2011, Article ID 753741, 3 pages
doi:10.1155/2011/753741

Case Report

Using Spectral-Domain Optical Coherence Tomography to Follow Outer Retinal Structure Changes in a Patient with Recurrent Punctate Inner Choroidopathy

Kimberly E. Stepien[1] and Joseph Carroll[1,2]

[1] *Department of Ophthalmolog, Eye Institute, Medical College of Wisconsin, 925 N 87th Street, Milwaukee, WI 53226, USA*
[2] *Departments of Cell Biology, Neurobiology, Anatomy, and Biophysics, Medical College of Wisconsin, Milwaukee, WI 53226, USA*

Correspondence should be addressed to Kimberly E. Stepien, kstepien@mcw.edu

Received 14 February 2011; Accepted 9 May 2011

Academic Editor: Fernando M. Penha

Punctate inner choroidopathy (PIC) is a rare idiopathic inflammatory disorder of the retina and choroid usually affecting healthy, young, myopic females and presenting with photopsia, paracentral scotomata, and blurred vision. It is characterized by yellow-white chorioretinal lesions concentrated in the posterior pole, no vitritis, relapsing inflammatory activity of the retina and choroid, and frequent development of choroidal neovascular membranes. Here we describe a case in which spectral-domain optical coherence tomography (SD-OCT) imaging was used to monitor outer retinal structure changes associated with recurrent PIC over time. SD-OCT, which is both quantative and objective, provides an efficient, non-invasive way to follow recurrent inflammatory chorioretinal lesion activity, choroidal neovascular membrane development, and treatment response in patients with recurrent PIC.

1. Report of a Case:

A 21-year-old white myopic female with a history of symptomatic punctate inner choroidopathy (PIC) presented with new photopsias and scotoma in her left eye for several days. She had been symptomatic in her right eye for one year with documented new chorioretinal lesion formation and development of a choroidal neovascular membrane (CNVM) successfully treated with photodynamic therapy (PDT), intravitreal triamcinolone, and intravitreal bevacizumab (Avastin, Genentech, South San Francisco, Calif). Past ocular history was significant for herpetic keratitis for which she was taking acyclovir 400 mg daily.

On exam, visual acuity was 20/20 OU with myopic correction. Anterior chamber and vitreous were without inflammation. Funduscopy showed multiple yellowish-white chorioretinal lesions and a pigmented scar from the CNVM localized within the posterior pole in the right eye, and a focal chorioretinal lesion with fluid just nasal to the fovea in her left eye (Figure 1). When compared to previous fundus photos, the lesion in the left eye was new. No peripheral lesions were present. Fluorescein Angiogram (FA) showed focal leakage, left eye, consistent with CNVM. Indocyanine green (ICG) showed hypofluorescent spots corresponding to the chorioretinal lesions consistent with PIC [1] in both eyes, and a focal area of hyperfluorescence at the edge of the hypofluorescent spot in the left eye, suggesting a CNVM.

Spectralis spectral-domain optical coherence tomography (SD-OCT) (Spectralis HRA; Heldelberg Engineering, Heidelberg, Germany) of the left eye at the initial visit showed retinal pigment epithelium (RPE) elevation with surrounding intraretinal fluid (IRF) consistent with CNVM (Figure 2(b)). Two weeks after treatment with intravitreal bevacizumab, SD-OCT showed resolution of IRF (Figure 2(d)).

Over the next 2 months, the patient continued to have symptomatic photopsias in both eyes. Clinical exam continued to show no anterior chamber inflammation or vitritis. She was placed on an extended oral prednisone taper. While still on 30 mg of oral prednisone, she experienced an acute

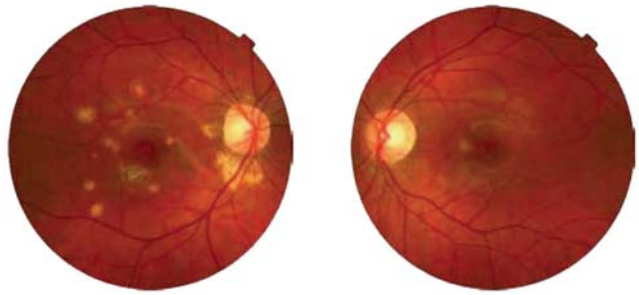

Figure 1: Right and left fundus photos of patient with recurrent punctate inner choroidopathy. Right fundus shows multiple yellowish-white chorioretinal lesions, some appear atrophic, localized to the posterior pole. Just inferior to the fovea is a pigmented scar from a successfully treated choroidal neovascular membrane. The left fundus shows a new focal yellowish chorioretinal lesion with surrounding fluid not documented on previous fundus photographs.

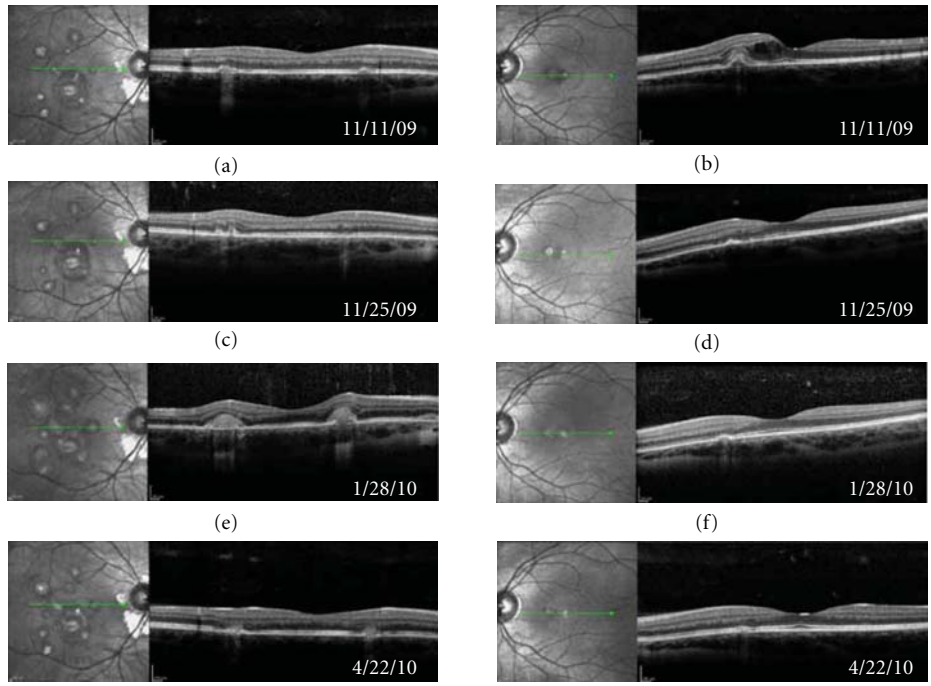

Figure 2: Spectralis spectral-domain optical coherence tomography (SD-OCT) images taken at the same location of both eyes over a 5.5-month period in a patient with recurrent punctate inner choroidopathy. (a) and (b) Initial visit. (b) Shows outer retinal irregularity and inner retinal fluid (IRF) from choroidal neovascular membrane (CNVM). (c) and (d) Followup two weeks later. After intravitreal bevacizumab treatment, left eye, shows resolution of IRF (d). (e) and (f) Two months later shortly after stopping chronic antiviral therapy. The patient experienced new photopsias, right eye, and SD-OCT revealed homogenous outer retinal thickening over chorioretinal lesions consistent with recurrent inflammatory activity (e). (g) and (h) Three months later after treatment. Symptoms subsided, and outer retinal thickening has resolved (g). Left eye shows no reoccurrence of CNVM (h).

increase in photopsias in her right eye. Four days earlier, she had run out of oral acyclovir. SD-OCT was suggestive of recurrent inflammatory lesion activity with new homogeneous outer retinal thickening overlying chorioretinal lesions but with no IRF (Figure 2(e)). The patient was treated with a higher dose of oral prednisone, oral valacyclovir (Valtrex, GlaxoSmithKline, Research Triangle Park, NC, USA), and two intravitreal bevacizumab injections over the next 2 months. Her symptoms resolved, and SD-OCT showed improvement in thickening over the chorioretinal lesions. Vision is still 20/20 OU.

2. Discussion

First described by Watzke et al. in 1984, PIC is a rare idiopathic inflammatory disorder of the retina and choroid usually affecting healthy, young, myopic females and presenting with photopsia, paracentral scotomata, and blurred vision [2]. Initial symptoms are usually unilateral although exam shows bilateral disease [2, 4]. Clinically, yellow-white chorioretinal lesions ranging in size from 100 to 300 microns are concentrated in the posterior pole and there is no vitreous inflammation [3].

Vision loss with PIC is usually secondary to development of CNVMs which can occur in 40–76% of patients [2–5]. Recently, intravitreal anti vascular endothelial growth factor (anti-VEGF) agents has been shown to be very effective in the treatment of CNVM associated with PIC [6–8]. SD-OCT imaging in our patient documented a great treatment response after intravitreal bevacizumab injection with resolution of IRF just 2 weeks after treatment.

PIC is characterized by relapsing inflammatory activity of the retina and choroid [9]. Unlike with CNVM where IRF was visualized, SD-OCT showed a homogenous thickening over the chorioretinal lesions with recurrent inflammatory activity. In this patient, her recurrent PIC may be associated with a viral etiology, as symptoms increased and SD-OCT documented outer retinal changes suggesting recurrent inflammatory activity shortly after cessation of chronic antiviral therapy. After restarting both immunosuppressive and antiviral therapy, both symptoms and SD-OCT findings improved.

SD-OCT gives excellent detail of outer retinal structures in patients with PIC. In this patient with recurrent PIC, SD-OCT imaging provided a quantitative and objective way to monitor outer retinal structure changes associated with CNVM development, treatment response, and recurrent inflammatory chorioretinal lesion activity. Given it is noninvasive, SD-OCT may prove to be a very effective way to monitor and better understand pathology in patients with PIC who develop CNVM and/or recurrent inflammatory activity.

Acknowledgment

This work was supported in part by an unrestricted grant from Research to Prevent Blindness, the Thomas M. Aaberg, Sr., Retina Research Fund and National Institutes of Health grant P30EY001931. This investigation was conducted in a facility constructed with support from the Research Facilities Improvement Program, grant number C06 RR-RR016511, from the National Center for Research Resources, National Institutes of Health. Dr. Carroll is the recipient of a career development award from Research to Prevent Blindness.

References

[1] J. Levy, M. Shneck, I. Klemperer, and T. Lifshitz, "Punctate inner choroidopathy: resolution after oral steroid treatment and review of the literature," *Canadian Journal of Ophthalmology*, vol. 40, no. 5, pp. 605–608, 2005.

[2] R. C. Watzke, A. J. Packer, J. C. Folk, W. E. Benson, D. Burgess, and R. R. Ober, "Punctate inner choroidopathy," *American Journal of Ophthalmology*, vol. 98, no. 5, pp. 572–584, 1984.

[3] S. R. Kedhar, J. E. Thorne, S. Wittenberg, J. P. Dunn, and D. A. Jabs, "Multifocal choroiditis with panuveitis and punctate inner choroidopathy: comparison of clinical characteristics at presentation," *Retina*, vol. 27, no. 9, pp. 1174–1179, 2007.

[4] J. Brown Jr., J. C. Folk, C. V. Reddy, and A. E. Kimura, "Visual prognosis of multifocal choroiditis, punctate inner choroidopathy, and the diffuse subretinal fibrosis syndrome," *Ophthalmology*, vol. 103, no. 7, pp. 1100–1105, 1996.

[5] A. T. Gerstenblith, J. E. Thorne, L. Sobrin et al., "Punctate inner choroidopathy. A survey analysis of 77 persons," *Ophthalmology*, vol. 114, no. 6, pp. e1201–e1204, 2007.

[6] W. M. Chan, T. Y. Y. Lai, D. T. L. Liu, and D. S. C. Lam, "Intravitreal bevacizumab (Avastin) for choroidal neovascularization secondary to central serous chorioretinopathy, secondary to punctate inner choroidopathy, or of idiopathic origin," *American Journal of Ophthalmology*, vol. 143, no. 6, pp. 977–e1, 2007.

[7] S. S. Mangat, B. Ramasamy, S. Prasad, G. Walters, M. Mohammed, and M. McKibbin, "Resolution of choroidal neovascularization secondary to punctate inner choroidopathy (PIC) with intravitreal anti-VEGF agents: a case series," *Seminars in Ophthalmology*, vol. 26, no. 1, pp. 1–3, 2011.

[8] V. Menezo, F. Cuthbertson, and D. M. Susan, "Positive response to intravitreal ranibizumab in the treatment of choroidal neovascularization secondary to punctate inner choroidopathy," *Retina*, vol. 30, no. 9, pp. 1400–1404, 2010.

[9] A. C. Cirino, J. R. Mathura Jr., and L. M. Jampol, "Resolution of activity (choroiditis and choroidal neovascularization) of chronic recurrent punctate inner choroidopathy after treatment with interferon B-1A," *Retina*, vol. 26, no. 9, pp. 1091–1092, 2006.